

W. T. Mayo



Experimental and Analytical Development of the Application of a Transit Laser Velocimeter

A. E. Smart and W. T. Mayo, Jr.
Spectron Development Laboratories, Inc.
3303 Harbor Boulevard
Costa Mesa, California 92626

November 1980

Final Report for Period March 1979 — September 1979

Approved for public release, distribution unlimited.

**ARNOLD ENGINEERING DEVELOPMENT CENTER
ARNOLD AIR FORCE STATION, TENNESSEE
AIR FORCE SYSTEMS COMMAND
UNITED STATES AIR FORCE**

NOTICES

When U. S. Government drawings, specifications, or other data are used for any purpose other than a definitely related Government procurement operation, the Government thereby incurs no responsibility nor any obligation whatsoever, and the fact that the Government may have formulated, furnished, or in any way supplied the said drawings, specifications, or other data, is not to be regarded by implication or otherwise, or in any manner licensing the holder or any other person or corporation, or conveying any rights or permission to manufacture, use, or sell any patented invention that may in any way be related thereto.

Qualified users may obtain copies of this report from the Defense Technical Information Center.

References to named commercial products in this report are not to be considered in any sense as an indorsement of the product by the United States Air Force or the Government.

This final report was submitted by Spectron Development Laboratories, Inc., 3303 Harbor Boulevard, Costa Mesa, California 92626, under contract F40600-79-C-0003, with the Arnold Engineering Development Center, Air Force Systems Command, Arnold Air Force Station, Tennessee. Mr. Marshall K. Kingery, DOT, was the Air Force Project Manager.

This report has been reviewed by the Office of Public Affairs (PA) and is releasable to the National Technical Information Service (NTIS). At NTIS, it will be available to the general public, including foreign nations.

APPROVAL STATEMENT

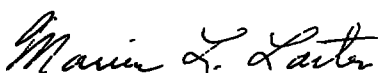
This report has been reviewed and approved.



MARSHALL K. KINGERY
Project Manager
Directorate of Technology

Approved for publication:

FOR THE COMMANDER



MARION L. LASTER
Director of Technology
Deputy for Operations

UNCLASSIFIED

REPORT DOCUMENTATION PAGE		READ INSTRUCTIONS BEFORE COMPLETING FORM
1 REPORT NUMBER AEDC-TR-80-28	2 GOVT ACCESSION NO.	3 RECIPIENT'S CATALOG NUMBER
4 TITLE (and Subtitle) EXPERIMENTAL AND ANALYTICAL DEVELOPMENT OF THE APPLICATION OF A TRANSIT LASER VELOCIMETER		5 TYPE OF REPORT & PERIOD COVERED Final Report - March 1979 - September 1979
		6. PERFORMING ORG. REPORT NUMBER SDL No. 79-6501
7. AUTHOR(s) A. E. Smart and W. T. Mayo, Jr.		8. CONTRACT OR GRANT NUMBER(s) F40600-79-C-0003
9 PERFORMING ORGANIZATION NAME AND ADDRESS Spectron Development Laboratories, Inc. 3303 Harbor Boulevard Costa Mesa, California 92626		10 PROGRAM ELEMENT, PROJECT, TASK AREA & WORK UNIT NUMBERS Program Element 65807F
11 CONTROLLING OFFICE NAME AND ADDRESS Arnold Engineering Development Center/DOS Air Force Systems Command Arnold Air Force Station, Tennessee 37389		12 REPORT DATE November 1980
		13 NUMBER OF PAGES 192
14 MONITORING AGENCY NAME & ADDRESS (if different from Controlling Office)		15 SECURITY CLASS (of this report) UNCLASSIFIED
		15a DECLASSIFICATION/DOWNGRADING SCHEDULE N/A
16 DISTRIBUTION STATEMENT (of this Report) Approved for public release; distribution unlimited.		
17 DISTRIBUTION STATEMENT (of the abstract entered in Block 20, if different from Report)		
18 SUPPLEMENTARY NOTES Available in Defense Technical Information Center		
19 KEY WORDS (Continue on reverse side if necessary and identify by block number) laser velocimeters anemometers discriminators performance tests fiber optics		
20. ABSTRACT (Continue on reverse side if necessary and identify by block number) Spectron Development Laboratories, Inc. has designed, constructed and demonstrated a rugged, compact, and reliable coaxial backscatter laser transit anemometer system. Measurements have been made through a 1.25" thick window without seeding at a range of 400 mm from very clean air at 1200 m/s with 80 mW of laser power incident on the sampling volume and a 100 mm diameter collection lens. The system employs many refined and/or new techniques which include specially prepared single fiber optic light guides, spatial filtering of flare		

UNCLASSIFIED

UNCLASSIFIED

20. ABSTRACT (Continued)

light from the opposite spot, high gain photomultiplier tubes with preamplifiers, filter/discriminators which reject single photon events and estimate pulse center time, microcomputer control of optics and electronics, with on-line flow parameter estimation and graphics display.

A digital correlator was used to further demonstrate the sensitivity of combining nonlinear filter discrimination techniques with single bit cross correlation. The 50 ns time clock was adequate for 0.6% absolute agreement with tunnel calibration at Mach 4.5 by interpolation of the correlogram store occupation. This delay increment was inadequate for supersonic turbulence intensity measurements with the optical configuration used. Repeatability of flow angle measurements was approximately 0.1° with the primary limitation being number of particle events available in a reasonable time. Previous Mie scattering and photon realization simulations indicate that particle diameters of 0.2 - 0.4 micrometers were observed at Mach 8.

UNCLASSIFIED

PREFACE

The work reported herein was conducted by the Spectron Development Laboratories, Inc., Costa Mesa, California, under Contract No. F40600-79-C-0003 with the Arnold Engineering Development Center, Air Force Systems Command. Air Force Project Manager for this contract was Marshall K. Kingery, AEDC/DOT. The work was conducted between March and September 1979, and the manuscript for this report was submitted to AEDC on October 30, 1979.

The reproducibles used in this report were supplied by the authors.

The authors wish to thank Ernestine Badman and Marshall Kingery for their support in administering the contract, and also Joe O'Hare, Bill Strike, and Willard Templeton, ARO, Inc., for their assistance during the tests at the Von Karman Facility.

TABLE OF CONTENTS

	<u>Page</u>
1.0 INTRODUCTION	7
1.1 LASER TRANSIT ANEMOMETRY DEVELOPMENTS	7
1.2 INTERVENING DEVELOPMENTS	8
1.3 CONTRACT SCOPE	8
2.0 ELECTRONIC DEVELOPMENTS	11
2.1 DISCRIMINATORS	11
2.2 MOTOR CONTROL FOR IMAGE ROTATOR	13
3.0 INTERNAL OPTICAL DEVELOPMENTS	18
3.1 ABERRATIONS AND OUTPUT LENS CHOICE	18
3.2 BEAM PARALLELISM EFFECTS	19
3.3 FIBER OPTICS	22
3.4 CLEANING AND ALIGNMENT	25
3.5 ALIGNMENT AIDS AND APERTURES	25
3.6 COMPONENT REDESIGN	26
3.7 IMAGE ROTATOR PRISM	27
3.8 COATINGS	29
3.9 DUST FREE PACKAGING	30
4.0 FLARE AND WINDOW THICKNESS EFFECTS	31
4.1 INTERNAL FLARE REDUCTION STOPS	31
4.2 INTERNAL REFLECTIONS AND SCATTER	32
4.3 CROSS STOP WALL FLARE REJECTION	33
4.4 WALL PROPERTIES	40
4.5 WINDOW THICKNESS EFFECTS	40
5.0 AEDC DEMONSTRATION (VKF)	43
5.1 EQUIPMENT SETUP	43
5.2 TUNNEL A RESULTS (MACH 4.5)	51
5.3 TUNNEL B RESULTS (MACH 8)	59
5.4 DISCUSSION	62

TABLE OF CONTENTS (CONTINUED)

	<u>Page</u>
6.0 CONCLUSIONS	63
7.0 REFERENCES	64
APPENDICES	
I -- "LASER TRANSIT ANEMOMETER WITH MICROCOMPUTER AND SPECIAL DIGITAL ELECTRONICS: MEASUREMENTS IN SUPERSONIC FLOWS"	67
II -- "SEMICLASSICAL PROCESSING OF LASER TRANSIT ANEMOMETER SIGNALS"	77
III -- "DISCRIMINATOR TESTS"	109
IV -- SECTION 7.0 THROUGH 7.3 OF "LASER TRANSIT ANEMOMETER SYSTEM OPERATION MANUAL"	123
V -- SECTION 7.4 OF "LASER TRANSIT ANEMOMETER SYSTEM OPERATION MANUAL"	135
VI -- "THICK WINDOW ABERRATION EFFECTS ON A LASER TRANSIT ANEMOMETER"	169

LIST OF FIGURES

<u>No.</u>	<u>Title or Description</u>	<u>Page</u>
1	Head and Data Management System	9
2	Typical Signal from Large Particles	12
3	Photograph of Discriminator Card and Plug In Modules	14
4	Photograph of Motor Control Board	16
5	Prism Motor Angular Rates	17
6	Formation of Two Spots by Wollaston Prism	20
7	Relay of Spots into Test Space	21
8	Mounting for Fiber Ends	24
9	Photograph of Image Rotator Prism	28
10	Image Through Stray Light Stops	34
11	Image of Output Lens Behind Cross Stop	34
12	Comparisons of Axial Rejection	36
13	Sources of Cross Talk	37
14	Mechanism of Cross Channel Scatter	38
15	Received Image Pattern with Flare	39
16	Spot Appearance Through Normal 4" Window	42
17	Spot Appearance Through 15° Inclined 4" Window	42
18	Spot Appearance Through 25° Inclined 4" Window (Disk of Least Confusion)	42
19	Spot Appearance Through 25° Inclined 4" Window (Near)	42
20	Spot Appearance Through 25° Inclined 4" Window (Away)	42
21	Installation of System in Tunnel A (Mach 4.5)	46
22	Optical Head with Beams Entering Fog in Tunnel A	47
23	Installation of Optical Head in Tunnel B (Mach 8)	48
24	Printout of Correlogram and Angle Plot from Tunnel A	50
25	Discriminated Output Signal from Tunnel A.	53
26	Data Rate and Data/Background Ratio Versus Threshold	56
27	Non-correlation of Measured Velocity with Threshold	58
28	Angular Plot for Tunnel B	58
29	Three Correlograms from Tunnel B	61

SECTION 1.0

INTRODUCTION

1.1 LASER TRANSIT ANEMOMETRY DEVELOPMENTS

Laser transit, time of flight, 2-spot, and L-2-F anemometry are all related names which have been used to describe different implementations of a class of laser techniques for measuring two-dimensional vector velocities. These techniques were developed initially as a method to reject noise produced by flare light better than has been achieved with the now conventional fringe laser Doppler velocimetry technique. However, we have demonstrated backscatter single-particle sensitivity and high supersonic velocity capabilities under this contract which show the technique to be suitable for many windtunnel applications, and others have shown that low-speed applications at ranges up to hundreds of meters may be possible.

The authors and others at Spectron Development Laboratories (SDL) have developed and demonstrated a prototype laser transit anemometer (LTA) system under Arnold Engineering Center funding in 1978, and the reader may wish to be familiar with the final report AEDC-TR-79-32 (May 1979) which is available from the NTIS. In order to provide the reader with an immediate introduction and review with additional descriptions of more recent developments and measurements, we have included reproductions of two recent conference papers as Appendices I and II. In addition, a list of references is provided as Section 7.0 of this report which includes the references of AEDC-TR-79-32.

The prototype demonstration with an unseeded supersonic jet at the AEDC in September 1978 was successful, but revealed a number of areas of improvement including electronic speed and reliability, optical efficiency and ease of cleaning and alignment, the understanding of thick window effects, the operation of the microcomputer control and data analysis system, and system and procedures documentation. During the

period September 1978 to September 1979, extensive improvements have been made and these are documented here.

1.2 INTERVENING DEVELOPMENTS

The instrument (Figure 1), which was created in 1978 with the partial support of AEDC Contract No. F40600-78-C-0002, was modified and used prior to the beginning of the present contract for supersonic feasibility measurements at NASA Ames Research Center (Reference 25) and for subsonic axial compressor measurements at the General Electric Company (Reference 24). In addition, SDL funds were expended in the further development of the microprocessor based data management system and the correlation detection theory. Most of the results of these activities are described in the appendices of this report.

The present contract was awarded in March 1979. The effort addressed the areas identified by the first AEDC contract, other than the data management system.

1.3 CONTRACT SCOPE

During the period from March to September 1979, the optical head of the LTA prototype system was extensively redesigned and a new unit constructed and tested to a standard where it could be applied to the hypersonic windtunnels at the Von Karman Facility (VKF) at the AEDC in late September. The resulting optical head was superficially similar to the prototype. The several and various optical and electronic changes occupied the period until September 4, when the equipment was shipped to the Arnold Center and installed on VKF tunnels with the assistance of Mr. Joe O'Hare, Bill Strike, and other ARO, Inc., personnel. Feasibility tests and measurements were conducted on Tunnel A during the night of September 10/11 and on Tunnel B the following night. Data were obtained from both experiments and were in good agreement with the calculated tunnel conditions.



Figure 1. Head and Data Management System.

This report describes the results of the present AEDC contract, i.e., the details of the design changes, the study of optical window thickness effects on spherical aberration, the laboratory tests of certain instrument parameters, and the feasibility demonstrations to Mach 8 with unseeded backscatter from 80 mW of laser power incident on the sampling volumes.

SECTION 2.0

ELECTRONIC DEVELOPMENT

Several significant changes were made to the first AEDC prototype system of Reference 20. Pulse discriminators were redesigned and tested. For this contract, photomultipliers with 14 stages and one high-speed preamplifier were used and we have noted that for improved operation in the presence of significant flare it is better to use two preamplifiers. In the latter case, the anode overload detection circuits are connected to a point between the preamplifiers. There is some discussion yet about whether to use 12 or 14 stage tubes for the flare constrained situation.

The Motor Control Card for the image rotator was redesigned and reduced to a printed circuit card; a set-up and calibrate procedure was documented. These items are described in Section 2.2 below.

Internal optical head wiring and connectors were standardized and "hardened" for reliability of operation in hostile environments, particularly vibration. A high voltage cutoff for tube protection was designed and fitted with care given to the safety aspect of high voltage when the side panels are removed from the head. No further discussion of these items is provided here.

2.1 DISCRIMINATORS

Figure 2 is an oscilloscope photograph of the summed signal from both monitor channels* triggered from that one upon which the event occurs first. Several features here indicate why the discriminators are necessary and what they should do. They should overcome the jitter caused by fixed level triggering of pulses of different heights. They should reject the pulses produced from single photon events while detecting all

*In the new design, the monitor output is taken from the output of the detection filter for the range selected by use of digitally selected reed relays.

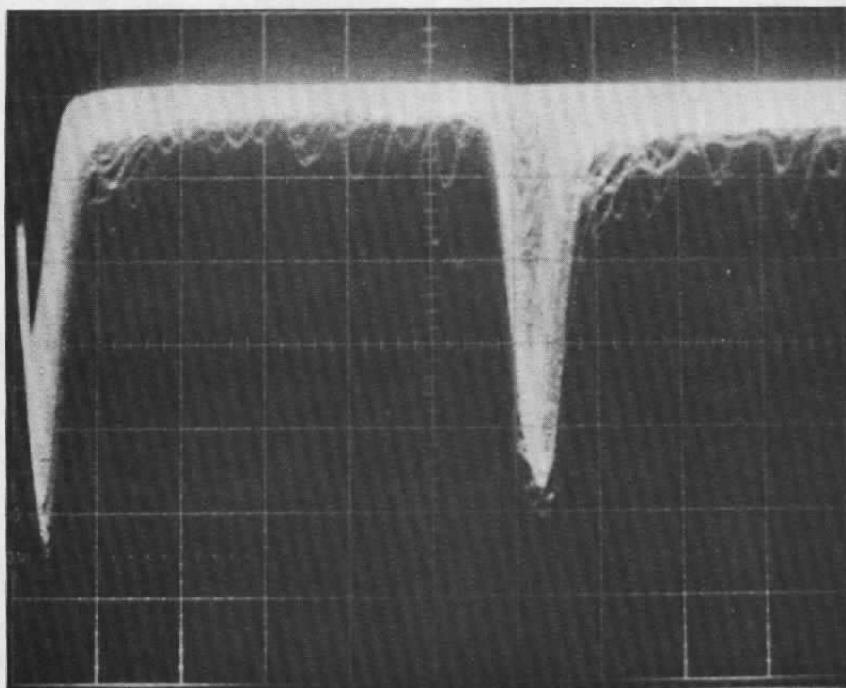


Figure 2. Typical Signal from Large Particles.

those whose photon bunching indicates a high probability of coming from a scattering particle. This photograph was taken in a low speed flow (100 m/s) using large particles ($>1 \mu\text{m}$ diameter) to show the salient effects.

The effect of separating multiphoton events associated with particle transits and single photon events from background light pulses by proper selection of detection filter threshold has been discussed earlier. (See Appendix II and References 20 and 25 for discussions of the detection and pulse center estimation techniques.) The first prototype system included a wire-wrapped card with plug-in integrated circuits and seven overlapping filter ranges going down to 100 ns pulse width for the integrated pulse center estimation filter. For the present tests, the electronic discriminator system was redesigned as a printed circuit board (Figure 3) with six plug-in filter/detector modules. These originally corresponded with the fastest six ranges in the prototype system, but for this contract, two even faster plug-in cards were developed. These were designated ranges 00 and range 0 and had pulse center estimation filter time constants of 25 ns and 50 ns respectively (the corresponding detection filter widths were approximately 15 ns and 25 ns respectively). The 00 board had no prefiltering other than that associated with the limited bandwidth of the photomultiplier and pre-amplifier combination. In Appendix III, we present some results of laboratory tests of the pulse delay accuracy and jitter of the discriminator circuits. The mean systematic errors and rms jitter are seen to be each on the order of 2 ns from those results for the fastest ranges 00 and 0.

2.2 MOTOR CONTROL FOR IMAGE ROTATOR

The circuits for motor instruction and driving to a specified position were translated from prototype breadboard to printed circuit construction with necessary and sufficient potentiometer adjustments for zero and calibration of the correspondence of mechanical position



Figure 3. Photograph of Discriminator Card and Plug-In Modules.

with electronic indication. A photograph of this board is included as Figure 4. It is connected by a Scotchflex ribbon connector for all power and data services and to the motor/prism combination by an eight-pin plug. Several monitor points are provided for checkout, calibration and troubleshooting.

The 0.05% linearity potentiometer was retained as adequate for the 0.1° resolution required of the device. Some more careful circuit adjustments enabled the position achieved by the prism to be consistently within $\pm 0.1^\circ$ arc of the requested position except in some extreme vibration environments where the error has been observed to be as large as 0.3° arc, but this is not normal and has not often been observed. The absolute accuracy is as high as the combination of the potentiometer linearity and the care taken in calibration will allow, but is typically within 0.4° over 360° .

At one stage, the new prism assembly exhibited stiction (before the oil formula was changed) and the residual error was a function of distance traveled. This was overcome before the thixotropy of the lubricant was discovered to be the culprit by using a second pass through the software to give a second dispatch instruction if the residual error on the first attempt was larger than 0.5° arc. This feature is retained as a safety measure even though the problem was solved by other methods. Occasionally, the V.D.U. reports that a second attempt was necessary and has been used to attain the final precision.

The angular speed achieved when moving to a new angular location has two domains dictated by the tracking loop conditions. For a change in angle of less than 20° arc then the speed to new location is $6^\circ/\text{s}$, station to station. If the angular change is greater than 20° , then the speed also varies with direction being $100^\circ/\text{s}$ for decreasing angle and $130^\circ/\text{s}$ when the angle is going towards higher numerical values. This is because the gear train from the motor experiences more resistance in the direction of decreasing angle.

The motor behavior is shown in Figure 5 which shows graphs on two scales $0 - 20^\circ$ and $0 - 400^\circ$ and the time for an angular traverse in these ranges regardless of starting position.

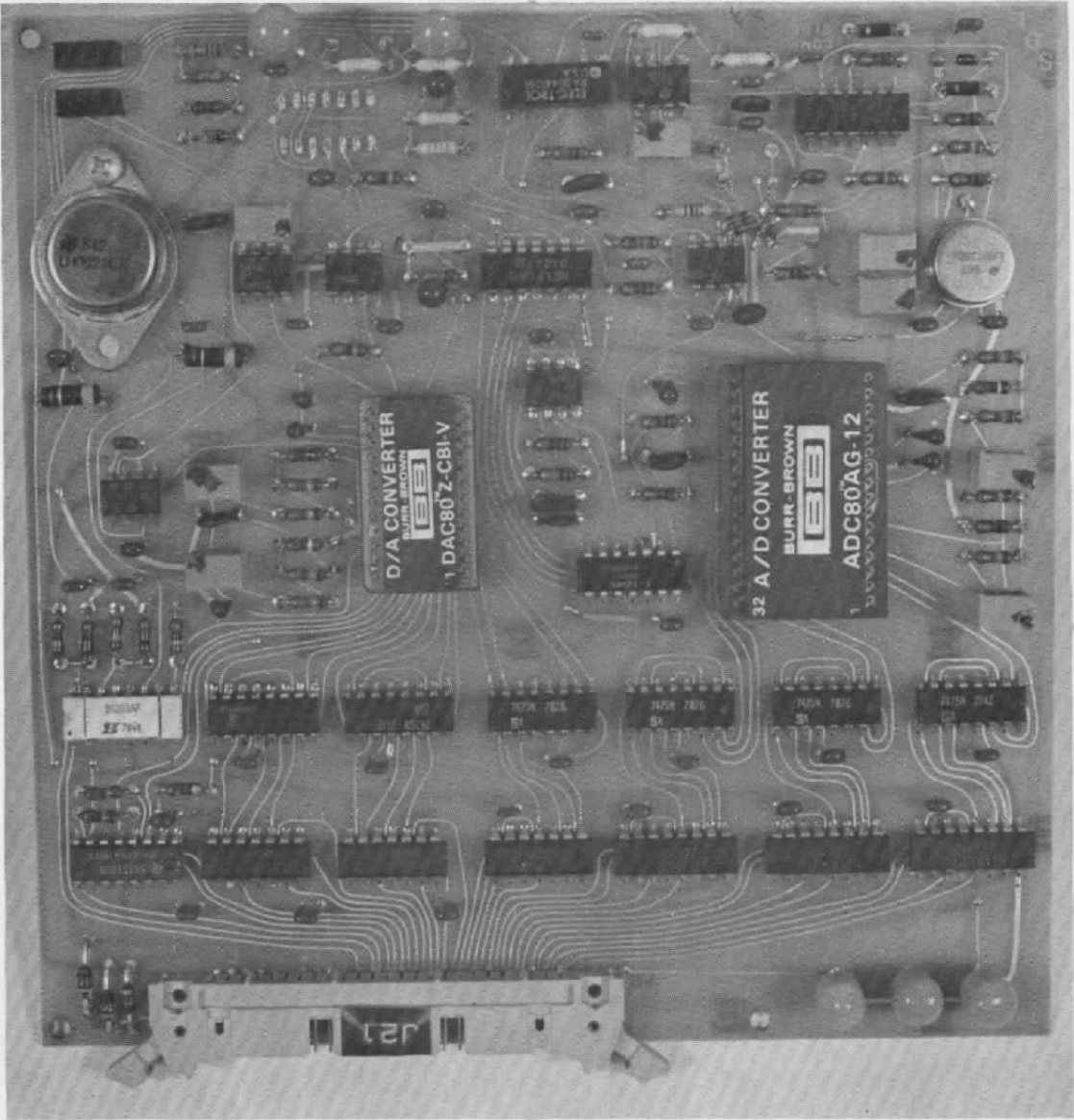


Figure 4. Photograph of Motor Control Board.

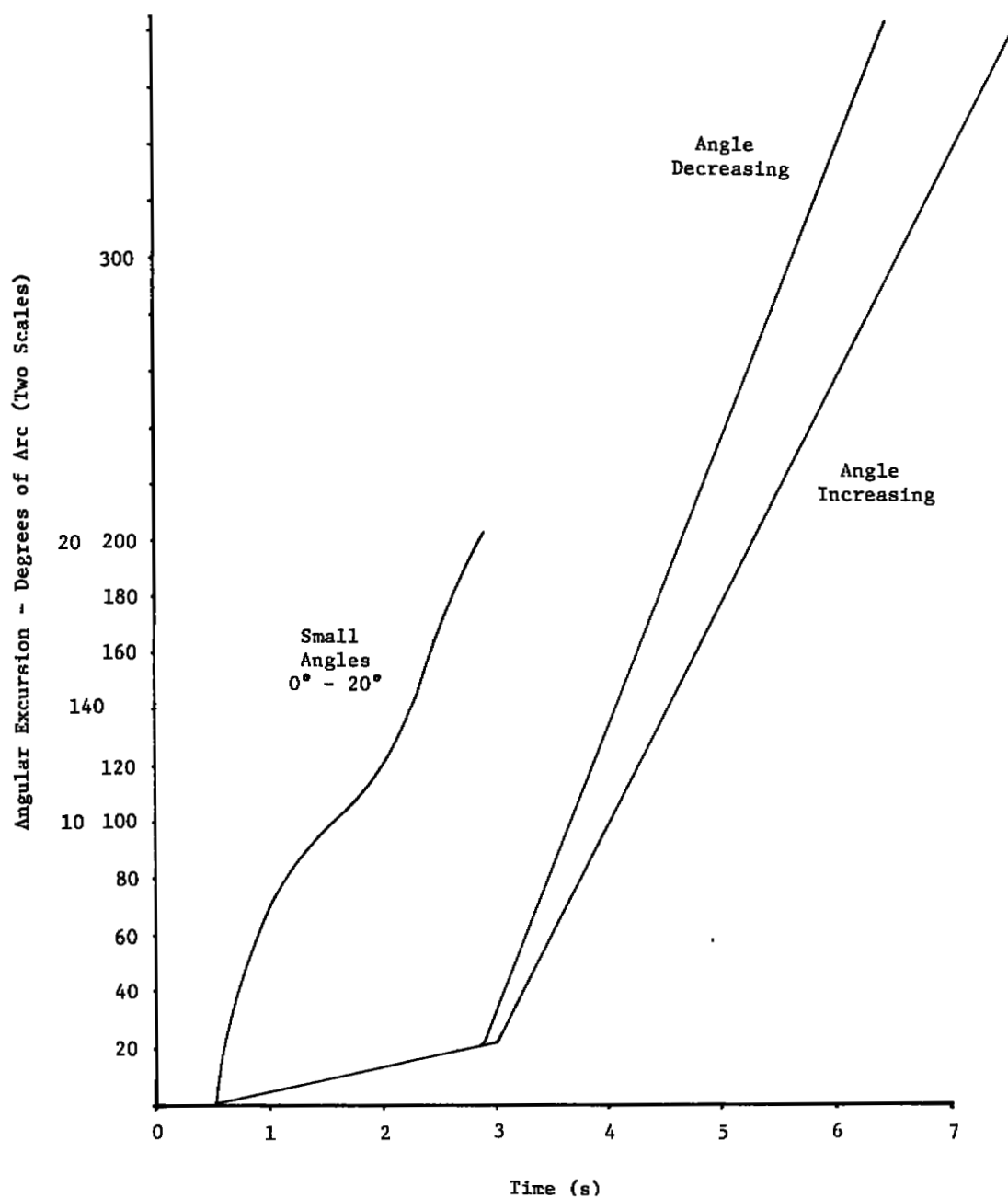


Figure 5. Prism Motor Angular Rates

SECTION 3.0

OPTICAL DEVELOPMENTS

The prototype instrument was built using general principles of good optical design. Only after some experience of the machine performance was it possible to select those critical areas where more careful study would produce significant improvement in performance, either in efficiency or in rejection of flare.

3.1 ABERRATIONS AND OUTPUT LENS CHOICE

The prototype system (used for the initial AEDC test - Reference 20 - and the Ames test - Reference 25) had an output lens system of 3" diameter lenses. These cemented achromats of fair quality and price were shown to limit the ultimate performance of this instrument very severely. There were two restrictions - residual spherical aberration and inadequate diameter. Because it was necessary to cure the former and this involved great effort, we decided to cure both sources of limitation by making a 4" system at increased cost to increase collecting power. The internal collimation now had an $f/4$ requirement and so far the only lens appropriate has been the Tropel 100 m, 400 mm focal length, collimator which has diffraction limited performance at any single visible wavelength, but is not achromatic. This last limitation carries a penalty for fluorescence work, but for such applications, the focusing qualities are less important and an inferior $f/4$ 100 mm diameter cemented doublet achromat may be installed. For a throw of about 400 mm, an output lens of the same specification as the internal collimator lens may be used. For 600 mm, a special lens has been obtained and proved very good. It is a cemented doublet which achieved near diffraction limited performance, actually slightly better than the Tropel, but it was working at $f/6$ which is much easier than $f/4$. Other lenses which proved to be adequate were 900 mm and 1600 mm air-spaced doublets, but many commercial lenses were rejected before these were found. No realignment is required except as discussed under Section 3.2 for very high precision in low turbulence.

The quantification of freedom from spherical aberration is further analyzed and discussed under Section 3.3.

3.2 BEAM PARALLELISM EFFECTS

The focusing lens images two points from the diverging but almost collimated small diameter beams emerging from the Wollaston prism. The center of the beamsplitter is near to the back focal plane of this lens which acts as a Fourier transforming element. The transform planes are not exact and the focusing lens may be axially translated to make the final output spots of light parallel to each other and the axis. The beams will suffer divergence if there is not due allowance for the magnification variation with axial position for an extended object in the projection system.

Figure 6 shows that for parallel spots in the output focal plane, it is essential to have the equivalent point of divergence in the back focal plane. Allowance must be made for the equivalent fore-shortening due to the refractive index of the prism. Because of the longitudinal variation of magnification shown in Figure 7, it is necessary to compensate this divergence with converging input spots. The system is designed to accept different output lenses and the first internal collimator (A in Figure 7) is set to produce parallel light so that the change of external lens B incurs minimum realignment problems. However, an output lens exchange, for reasons shown by inspection of Figure 7 will change the equivalent amount of required compensation to a small degree. The effect is only a few milliradians for typical dimensions but for low turbulence applications should be removed by readjustment of the Wollaston prism and focusing lens separation.

Reference 24 discusses this same point.

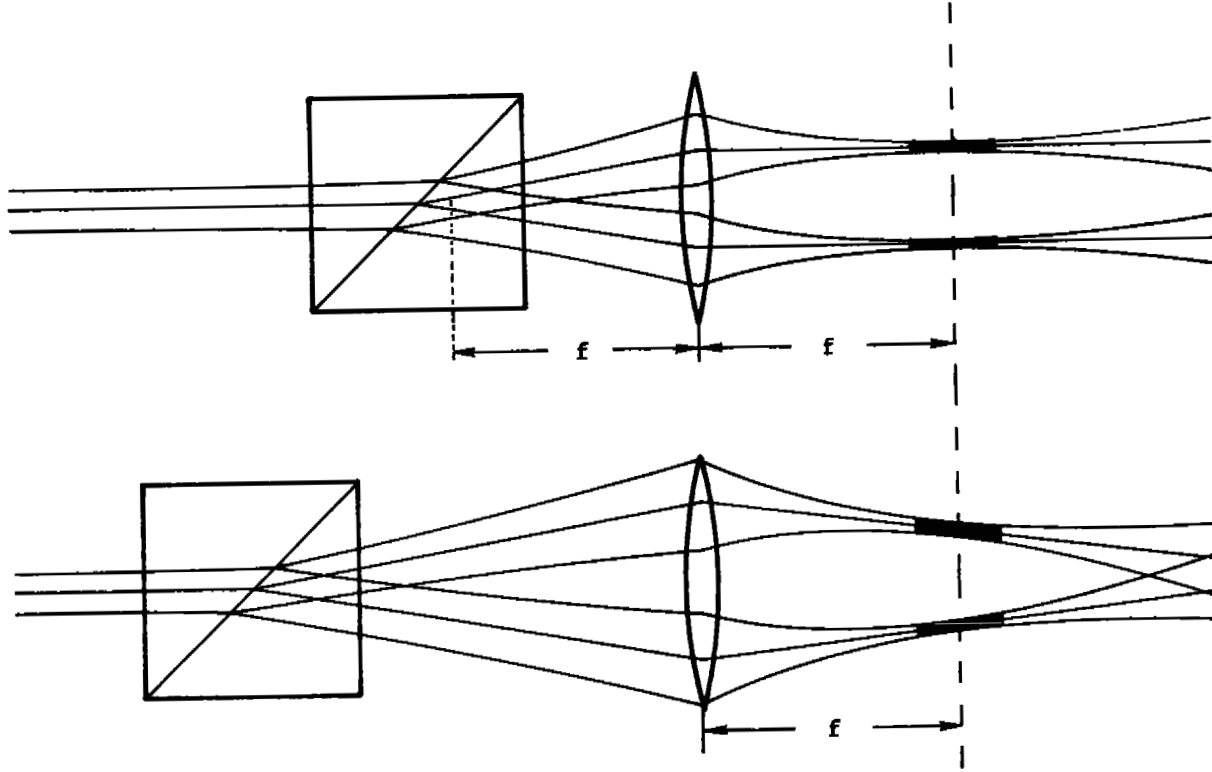


Figure 6. Formation of Two Spots by Wollaston Prism.

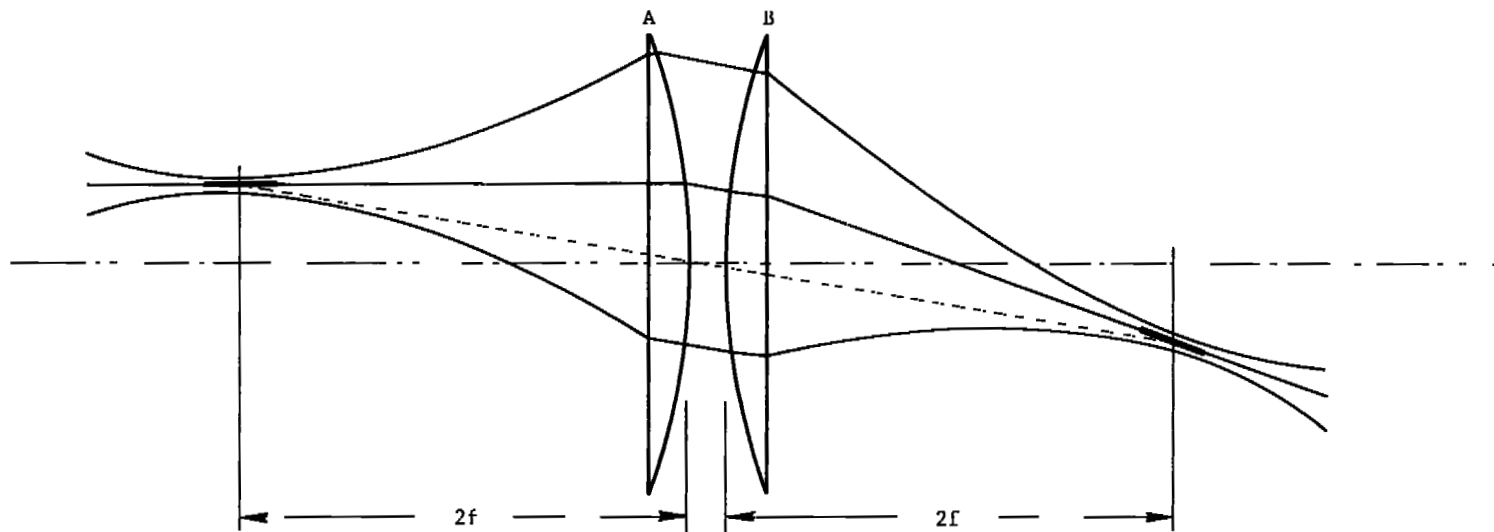


Figure 7. Relay of Spots into Test Space.

3.3 FIBER OPTICS

The original idea of using fiber optics to relay the light from the field image to each photomultiplier was good but required some refinement. Several areas needed attention, the matching of equivalent field size with final return image, allowance for all aberration sources, the reduction of insertion losses and protection from damage.

The mounting method for adjustable fiber optics was selected to be within hypodermic needles and both the needles and fibers are only available in a limited number of sizes. After some deliberation about topics such as mechanical handling, strength, bending radius and packaging, 230 μm diameter fused silica single fibers were selected. Multiple fibers immediately incur a high insertion loss because of interfiber spaces. The magnification available from any of a number of microscope objectives available as an enlarging lens compensates partially for the fixed choice at this point. A $\times 7$ objective was adequate although calculations show that the diffraction limited image would thus use less than all of the available fiber diameter. The additional size compensates for some aberration and even a small amount of misalignment. At the same time, it is sub-optimal in the theoretical rejection of light scattered from the axial regions near the probe volume. There is a trade-off here between collecting all the light and restricting the probe volume length. There are other trade-offs related to these same parameters (see Sections 3.5 and 3.6).

We chose to use this configuration as an all-around optimum but note that exchange of the enlarging lens will either increase the focal volume definition at the expense of light collection efficiency and difficulty of alignment with potential for adverse effects from alignment drift, or will improve the light gathering power (slightly) and improve the tolerance to misalignment but sacrifice some restriction of the probe volume length.

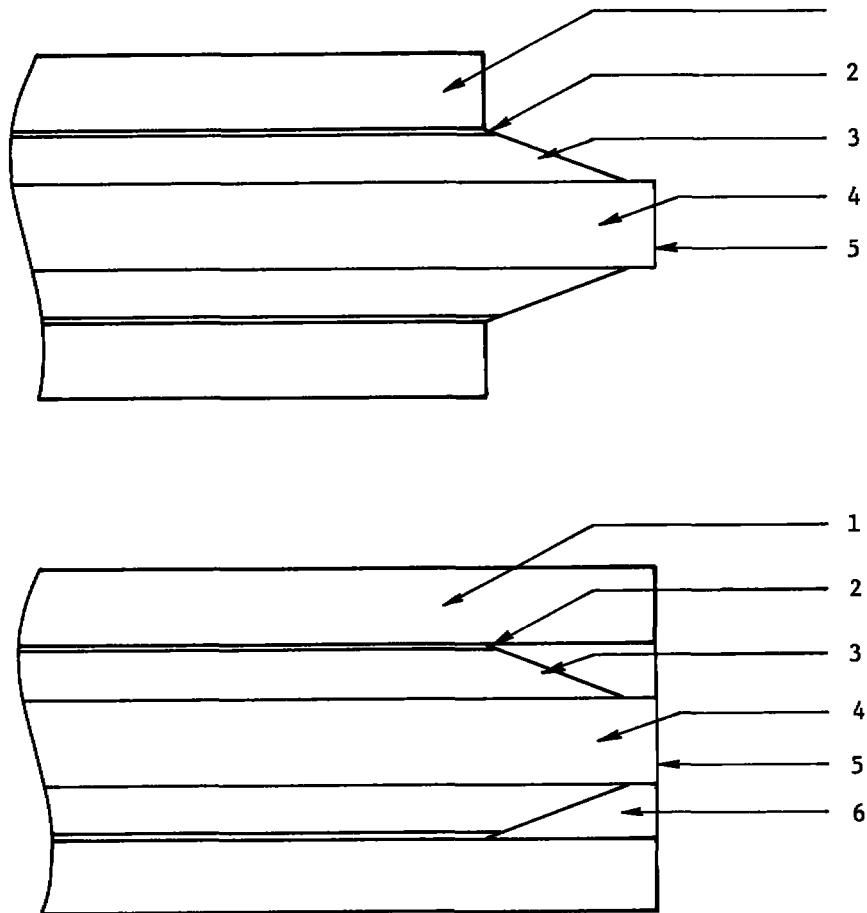
Initially, the fiber ends were cleaved normal and mounted to protrude slightly from their fragile low refractive index sheath and to stand proud of the needle end. This was poor, being inadequate fiber support and leaking light. A second batch of fiber was obtained with a

much superior and more rigid low index sheath and the same construction now was physically sound but optically made poor sense. The protruding fiber was being used as the field stop but was not limited in its acceptance of light by the limits of the core fiber. The cladding permitted light to leak into the core.

Figure 8a shows the initial construction as it suffered from poor stop delineation and had extreme tendencies for the edge of the cleaved fiber to break off. The loss of these corners affected the near flat normal end face and caused the insertion loss to be up to a factor of 20 which was totally unacceptable.

With the improved construction, Figure 8b, the fibers were rigid, well protected from accidental damage and, curiously, showed less tendency to accrete dust. The black rubber surrounding the fiber end was an effective stop to radiation outside the area of the fused silica and also made alignment much easier. When the final image is focused upon the now flat end of the entire hypodermic assembly, it is easy to see the bright best-focused pattern on either the metal rim of the hypodermic needle or the black rubber. When the adjustment is correct, the end of the fiber gives rise to less scattered radiation because the core of the fiber appears totally dark provided the other end is in darkness.

The fibers are about 18" long so the transmission losses, even in a fiber, poor by communication standards, is quite negligible. For a spot of low divergence smaller than the fiber end and placed so as to be wholly within the fiber edge, but not necessarily centered, the overall transmission is typically 82%. Any reduction from this implies damage and the fiber unit must be discarded. In the configuration of this instrument, the output from the fibers is restricted to a cone of about 10° total angle. It is not possible to misalign the fiber incidence angle sufficiently badly that this output will diverge to a much larger or dark centered cone and for this reason it is not necessary to recollimate the light at the photomultiplier end prior to any narrow band filtering which may be desired.



- 1 Steel Hypodermic Needle
- 2 Epoxy Adhesive
- 3 Low Refractive Index Cladding
- 4 Optical Fiber
- 5 Well Cleaved End
- 6 Black Rubber Cement

Figure 8. Mounting for Fiber Ends

3.4 CLEANING AND ALIGNMENT

The cleaning procedures for the instrument are outlined in Appendix IV which is Section 7.0 through 7.3 of the operating manual for the instrument. There are several new design features here which make cleaning either easier or less necessary than in the prototype instrument.

Because of the extremely critical optical performance of this machine, the optical alignment is very important. It is designed to preserve the correct alignment once it is fully aligned and there are small and specific adjustments to correct for laser aging and other long-term drift effects. The details, which we have developed under this contract, are long and tedious and are outlined in Appendix V which is also Section 7.4 from the operating manual. This section is not yet completely foolproof. There is a detailed sequence for aligning the image rotator prism but minute errors in this may interact with the basic system alignment detailed here. The undesirable consequences of this are that either the spots may be correct with the lens output position sustaining a small orbit of the shape of the Limacon of Pascal, or vice versa. As yet, we have not completely analyzed this error but it may be removed by careful manipulation of the adjustments on the prism and turning mirror supports.

3.5 ALIGNMENT AIDS AND APERTURES

The sequence of Appendix IV is facilitated by design changes such as the insertion of a circular stop just above the Wollaston prism. Not only does this serve to keep the prism relatively free from gravity-deposited dirt, it serves as an intermediate alignment aperture for the laser so that if its cavity is changed to restore maximum power for any reason, it is very easy to restore the alignment of the system without recourse to the full procedure. This may be done by gentle adjustment of the first mirror encountered from the laser.

Centration of beams is made possible at several points in the system, image rotator input and output and final lens aperture, by use of the target patterns of Figure 7.4.11 in Appendix V printed on to overhead projection transparency material and cut to suitable diameter. The input aperture from laser to optical system is arranged so that the system is aligned when the beam is normally incident and centered on the hole; the condition is assured by multiple reflections from an inserted microscope cover slip.

3.6 COMPONENT REDESIGN

The turning mirror and its mount were extensively redesigned for two reasons: (a) to reduce the size of the assembly so that it could be brought so close to the image rotator that the latter became the limiting f/No aperture, (b) to facilitate critical final alignments by kinematically separating the available degrees of freedom and, (c) to allow for insertion of a new type of stop (Reference 24 and Section 4.3 of this report). The new design is smaller and simpler (See Figure 7.4.7 of Appendix V, Items I through L).

The output lenses and mountings were significantly changed to allow up to 4" free diameter lenses in standardized cells. The new lens cell yokes are precisely centered so that no realignment is necessary on the exchange of the outer lens. A small amount of axial adjustment is present to allow perfect collimation after the beam parallelism has been corrected by translation of the focusing lens with respect to a fixed Wollaston prism. There is a difference in free length of Wollaston prisms of different divergence angles and only the shorter ones ($1/2^\circ$ and 1°) may be translated axially in the support. There was substantial redesign of the optical head assembly to accommodate the new electronics cards and to be the basis of standardization of connections. These services are now sufficiently hardened to provide high reliability.

3.7 IMAGE ROTATOR PRISM

The image rotator prism has been redesigned including glassware, mechanics and coatings.

The new rotator prism conforms to the design and description of References 20 and 23 (Figure 9) but has a few small and significant improvements. The precision ball bearings were replaced with plain bearings which had a mixed effect. Side float was effectively removed giving more precise location of the mechanical axis and better freedom from backlash which gave minute cyclic errors.

The change was not a total cure because a small amount of end float now necessary to provide free rotation gave a very slight glitch at one point of the cycle. The magnitude of optical/mechanical axis misalignment on the occurrence of the glitch varied between zero and about 30% of the spot separation. This does not cause problems in any application so far performed or envisaged. The bearings were lubricated with thixotropic oil at first, but this was later replaced by refined watch oil with the opportunity for re-oiling with age and use. The brake could now be dispensed with, but a mechanical end stop was still incorporated.

The glassware of the large base prism was redesigned to give a larger aperture without other penalty. This redesign also eased manufacture. Both this prism and the mirror are now hard coated with silver and a MILSPEC overcoat so that they may be cleaned. The normal reflectivity was reduced to between 95% and 96%, but this was thought acceptable in lieu of increased durability. All non-active surfaces of glassware were painted with optical black paint to suppress reflections of light transmitted by the nominally reflective coating. In systems such as this, where there is great emphasis on stray light suppression, a number of such tasks produced beneficial results.

The flat mirror mount was changed from simple bolting to a reference counterbore to a 3-point kinematic mount to avoid the distortion which became evident on interferometric testing of the completed assembly.



Figure 9. Photograph of Image Rotator Prism.

The motor gearing ratio was increased to aid better response to small signals from residual errors. There was some difficulty in maintaining equality of rotational resistance at any angular position as the entire assembly was not perfectly rigid for reasons of lightness. Selective shimming on assembly and three-point mounting to the spine plate minimized any unsatisfactory consequences.

3.8 COATINGS

There is a requirement for high optical efficiency, low flare, and practicability of cleaning optical components and this places a strict specification on reflective and anti-reflective coatings. For the 45° mirrors, the Newport Research Coating DM.2 was specified. This is a cleanable hard dielectric coating of 99.8% reflectivity at 45° for both argon wavelengths, 488.0 nm and 514.5 nm. Unfortunately, it was not practicable to obtain a similarly excellent coating for the turning mirror. Such a coating is not suitable for the image rotator prism whose incidence angles are predominantly 60° and 30° with an f/4 angular spread of 7.2° half angle. For this and the turning mirror, we specified hard overcoated silver and accepted the loss of 4% per reflection per surface in order to obtain mechanical cleanability and insensitivity to polarization (hence the metal). With any sensitivity to rotation of the polarization vector, the spots will change their relative intensities and impair the statistics of data obtained at a range of angles.

Wollaston prism, focusing lens and all output lenses were broadband coated with best performance in the green. The 1/4% reflection of the Tropel was a considerably better performance than that of other components. The cleaved fiber ends were not coated, nor were the photomultiplier faces. Although there is considerable emphasis on not losing light, the more important property is not to scatter nor reflect unwanted light into places where it could result in detected photons or bunches of photons.

All the above coatings are sufficiently durable to be cleaned by the methods of Appendix IV and show considerable resistance to accidental mechanical damage. Because this is not an imaging system 'per se', small flecks of deposited dust or scratch and dig damage do not contribute primary malfunction. As they worsen, the scattered light may rise but it may be rejected over a wide dynamic range of photon rate by the electronic methods outlined in References 20 through 22.

3.9 DUST-FREE PACKAGING

The exclusion of dust and other contaminating media is of importance for long-term functioning of the optical system. To this end, the head is sealed by velvet tape, heavily compressed at each metal joint. A stepped construction has also been adopted which assists in the rejection of foreign matter (and light, of course!). The side panels are pre-flexed so that pressure is maintained upon the seals while preserving the ability to remove the panels easily with only four thumb nuts each. The front panel at the top of the head is quite easily removable so that small mirror adjustments may be made without interfering with the main components, nor opening the head in a test environment.

SECTION 4.0

FLARE AND WINDOW THICKNESS EFFECTS

The system relies basically upon classical detection of bunches of photons scattered from particles in the flow through the test space. Any stray light is essentially scattered laser light and is thus a Poisson distributed stream of photons. In principle, as long as the statistical fluctuations of photon rate give a very low probability of two or more stray light photons occurring within one particle transit time, and multi-photon particle scattering occurs, this source of error may be entirely rejected by thresholding. Actually, the cutoff is not unambiguous and it is always important to reduce flare as much as possible from both internal and external sources. This becomes especially true when the signal from particles is an average of only two or less photons and the threshold discriminator will no longer reject noise. If, in that condition, the noise from scattered photons is low enough, the system will still extract data from the test situation. Flare rejection is degraded by all sources of spherical aberration, as discussed previously for lens effects. In this section, we also present a study of the spherical aberration effects of thick flat windows. This is discussed in greater depth in Appendix VI.

4.1 INTERNAL FLARE REDUCTION STOPS

The two apertures, the light admission hole into the box and the stop retained by O.P. on Figure 7.4.7 of Appendix V each minimize flare from scatter or diffraction sources from the laser to that stop. This latter aperture is dual function in that it is an alignment aid and a flare suppression stop. Its second function becomes more relevant if the mirrors preceding it in the optical train become dusty or damaged.

The beam incident upon the turning mirror has a Gaussian spread function and an associated group of haloes from multiple reflections and forward scattered light in the Wollaston prism and focusing lens. Residual transmission through the coating and diffraction from the edges of the turning mirror are suppressed by a small square baffle fixed behind the mirror. This becomes the limiting center stop of the return system (Reference 13) and may have different configurations according to function. For windtunnel tests, it was not fitted with 'wings' (See Section 4.3) as collection of light was more important than rejection of external flare.

The projected silhouette of the turning mirror is square because we have chosen to use a right-angled prism of 2.7 mm side as a readily available and adequately flat component. Accordingly, the guard stop under discussion is square and incurs typical 'square stop' diffraction patterns from scatter and reflections in the output optical train. At their 45° displacement, the receiving apertures cannot observe the bright lines of this pattern and thus no additional diffraction penalty is incurred.

The stop is made from 0.005" brass shim stock with carefully finished edges and chemically blackened surface and is slightly adjustable in position to compensate for any manufacturing or other system asymmetries. Observation through the return apertures will quickly assure that this stop is optimally located and further identify any flare sources in the system. The return picture is quite complicated and exists as a different view according to which plane is focused.

4.2 INTERNAL REFLECTIONS AND SCATTER

The construction of this instrument is such as to have very little of the source laser light returned to the photocathodes by unwanted means, particularly those due to optical components in the optical head system itself. The laser produces typically 3×10^{17} photons/s while

typical flare light from all internal sources (i.e., with the lens capped on the outside) is between 10^4 and 10^6 photons/s. Thus, the internal design achieves a flare suppression of 11 to 13 orders of magnitude.

On typical high speed ranges, the probability of a photon coincidence within a transit time is low and thus two-photon particles are detectable above the background as was predominantly so in the tests reported in Section 5 of this report.

To achieve these levels, it is necessary to have small, well chosen stops and to arrange that reflections from even fifth and sixth order images in glass components are geometrically excluded from receiving apertures. There is a curious effect from diffraction of the return light at the pinhole apertures. This is manifest very obviously with a scatterer of surface texture in the range of μm placed at the sampling volume, and is also observable as an integrated pattern from sufficiently dense particles. Figure 10 is a photograph of the image of the return stops showing that the focus is significantly smaller than the stops. The radial diffraction from the stop edge is not finally included in the detected light for the most restrictive field stop is the end of the fiber optic but it is an effect which should perhaps be considered further. If the pinholes were to be made smaller to reduce scattered light more, then this diffraction becomes worse. The patterns of diffraction may be seen in Figure 11, an image of the output transceiver lenses, taken through the center stop and receiving system up to the fiber ends. These are light random bands just discernible in the area blocked by the cross stop (see Section 4.3 and remember this figure).

4.3 CROSS STOP WALL FLARE REJECTION

Light returned to the instrument may be from small particles or from walls or other physical objects in or near the sampling volume. The rejection of this light is very important when measurements are to be made near model surfaces (in boundary layer regions, for example) or in reentrant cavities such as between blades in turbomachinery.

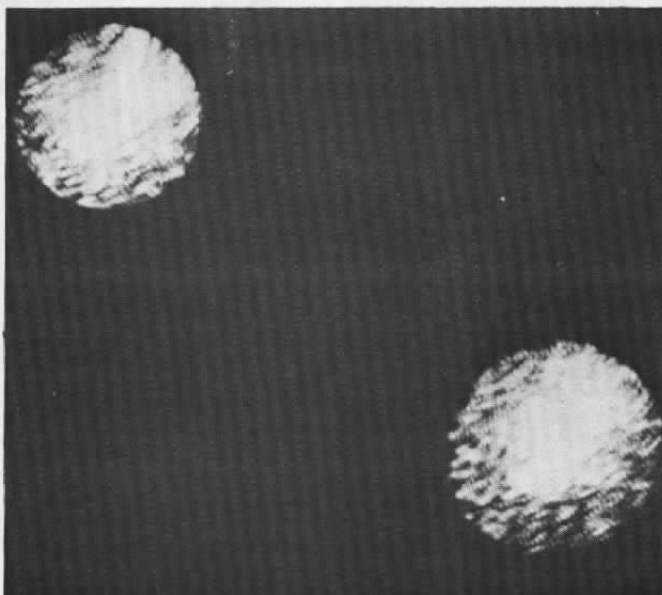


Figure 10. Image Through Stray Light Stops.

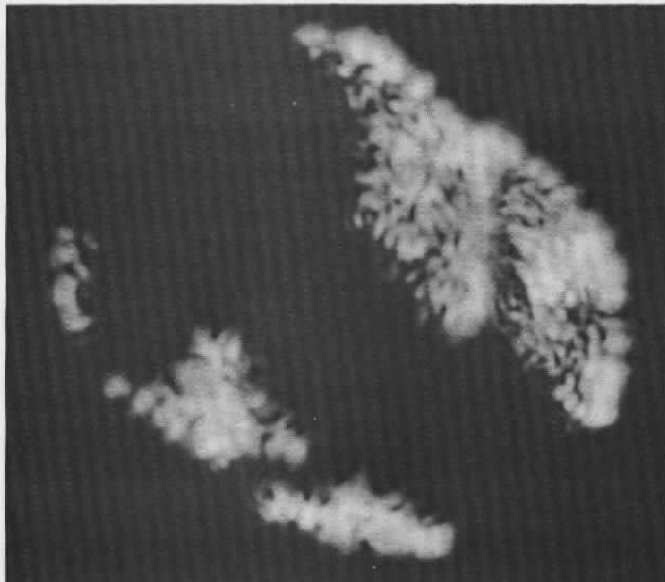


Figure 11. Image of Output Lens Behind Cross Stop.

As a result of making measurements in a compressor, the axial rejection of flare was seen to be good from its own channel, but there was cross talk from the other channel. Tests were performed and Figure 12 was obtained by scanning a Lambertian scatterer, with texture of a micron or two and fair opacity, through the active region of an LTA system. The far field scatter pattern has a scale which was small compared with the receiving aperture except within a few tens of microns of the best focus. The return signal was plotted to show the sensitive region with only the center and field stops in place and we see that these are effective in controlling the axial extent of sensitivity to its own channel illumination down to two-and-one-half orders of magnitude below the peak. From this dotted curve in Figure 12, it is obvious that there is a return of sensitivity to flare with increasing axial distance from the sensitive volume in both directions. Figure 13 shows how this spurious light arises from illumination in the other channel and Figures 14 and 15 the mechanism of production and appearance of the annular flare on the field stop. The effect of cross channel flare is manifest when the halo from one beam crosses the return aperture from the other as the halo expands and defocuses.

The effect is analogous but inverted as the scatter source is translated from one side of the sensitive volume (a dirty window, say) to the other (a wall or other mechanical boundary). The cure for this most detrimental limit to wall proximity is to attach wings to the center stop which occlude the flare pattern as shown in Figure 7.4.35 of Appendix V. This 'cross stop' then suppresses the flare to the solid curve of Figure 12.

The real appearance corresponding to Figure 7.4.35 of Appendix V is shown as Figure 15, a photograph of the effect of the cross stop on the light collection cone.

This optical improvement we have called a 'cross stop' because it eliminates channel cross talk, it is a cross between a field stop and an aperture stop, and it is shaped like a cross. It is possible to use the empirical data of Figure 12 to estimate the achievable wall proximity knowing the particle sizes available to scatter. It must be noted that the rejection shown is relevant to a scatterer which covers the whole

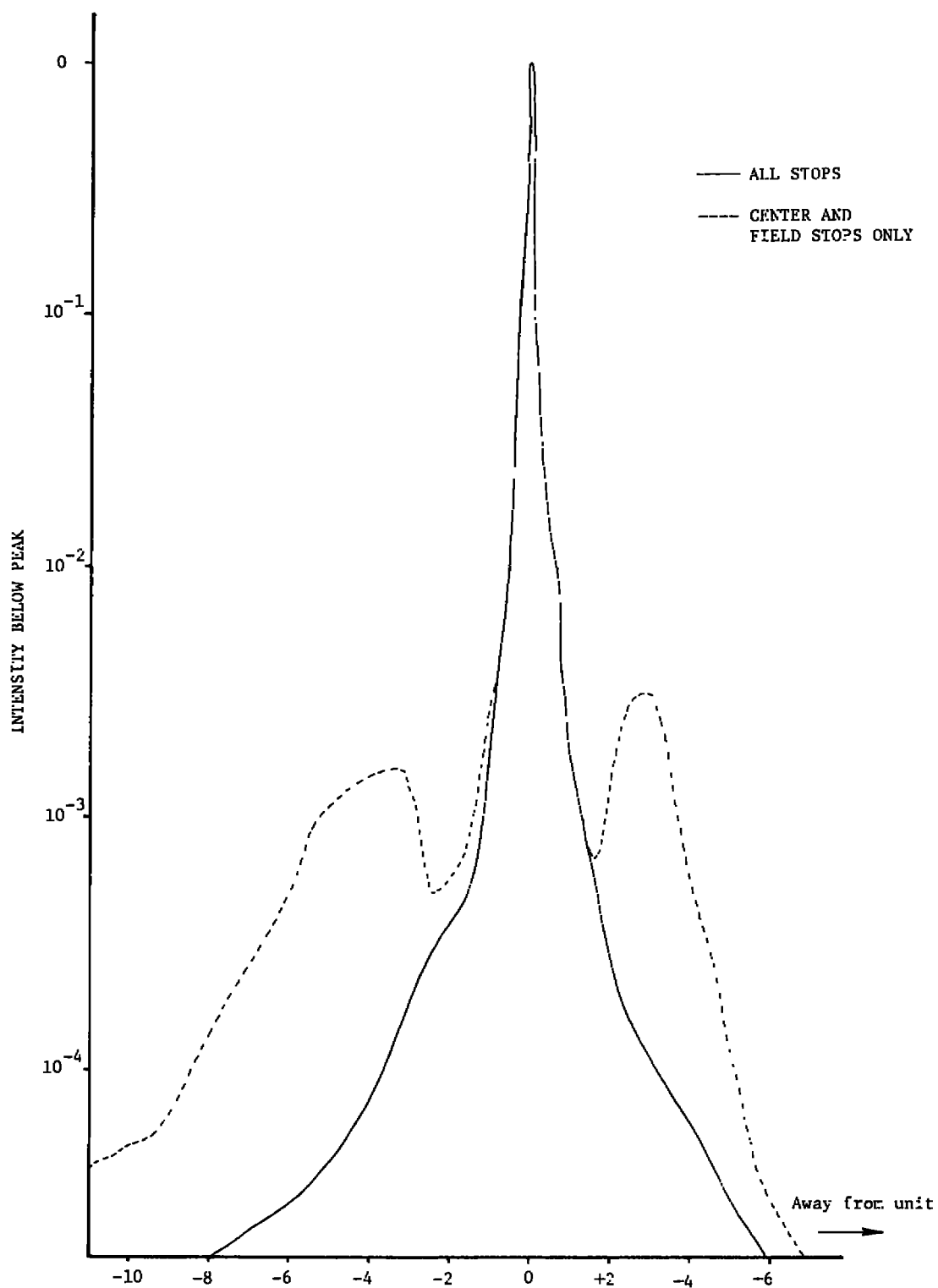


FIGURE 12. COMPARISONS OF AXIAL REJECTION

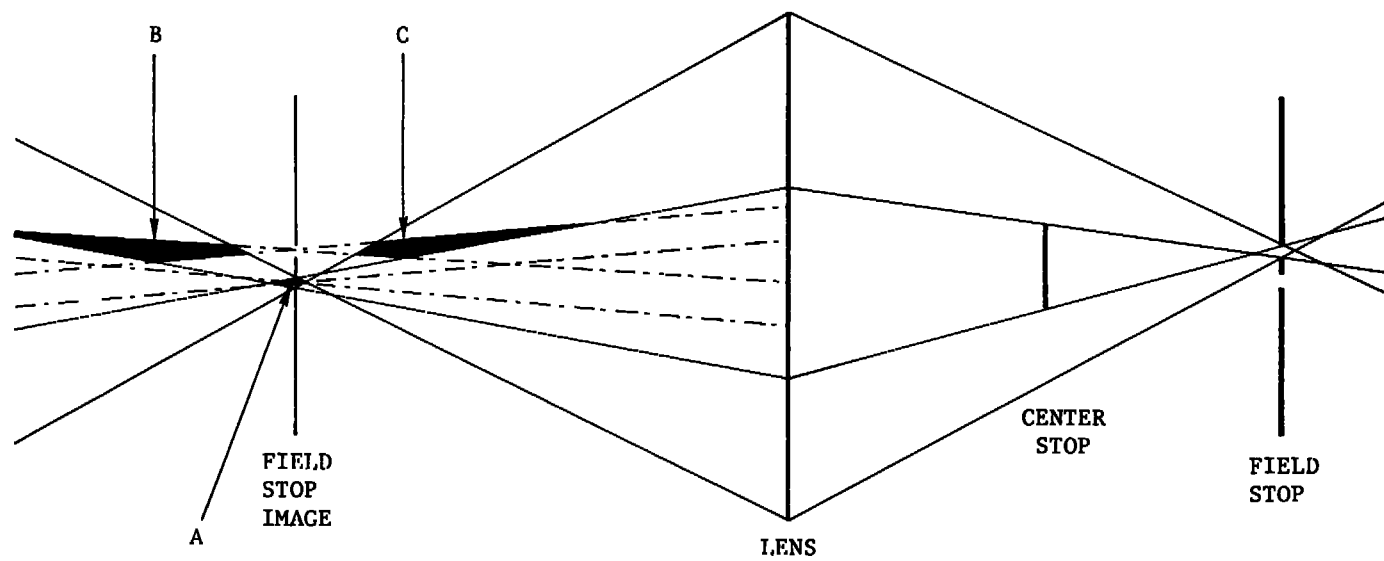


FIGURE 13. SOURCES OF CROSS TALK

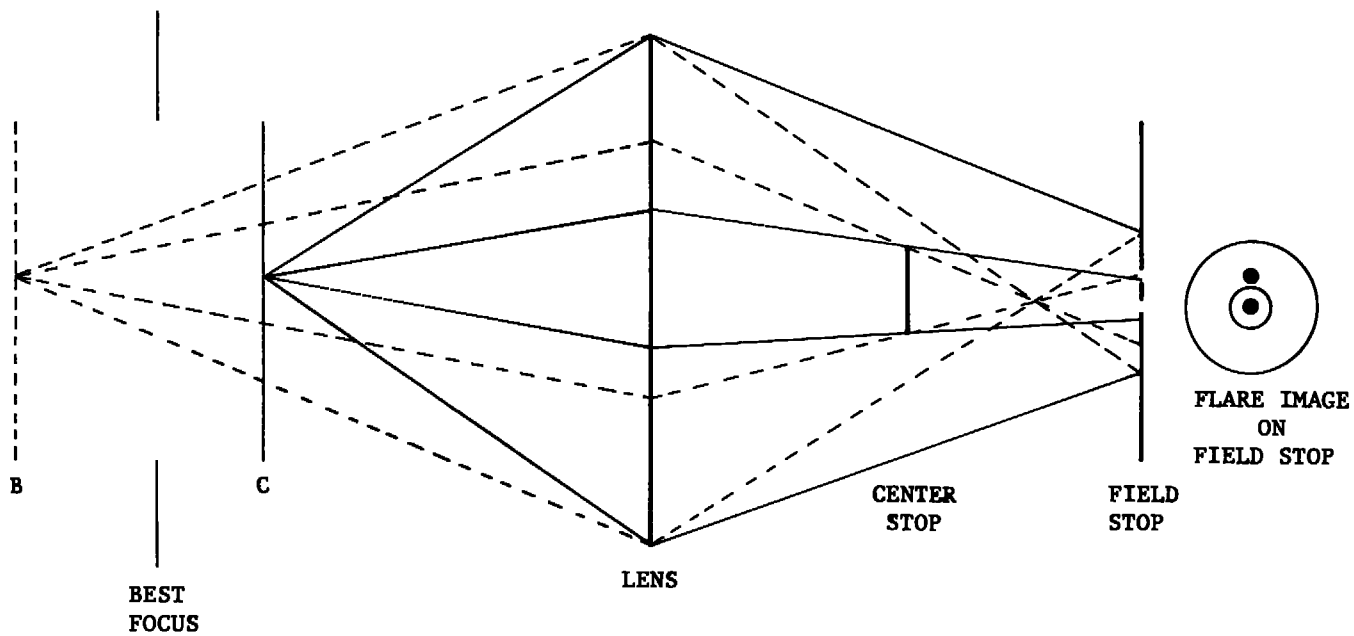


FIGURE 14. MECHANISM OF CROSS CHANNEL SCATTER

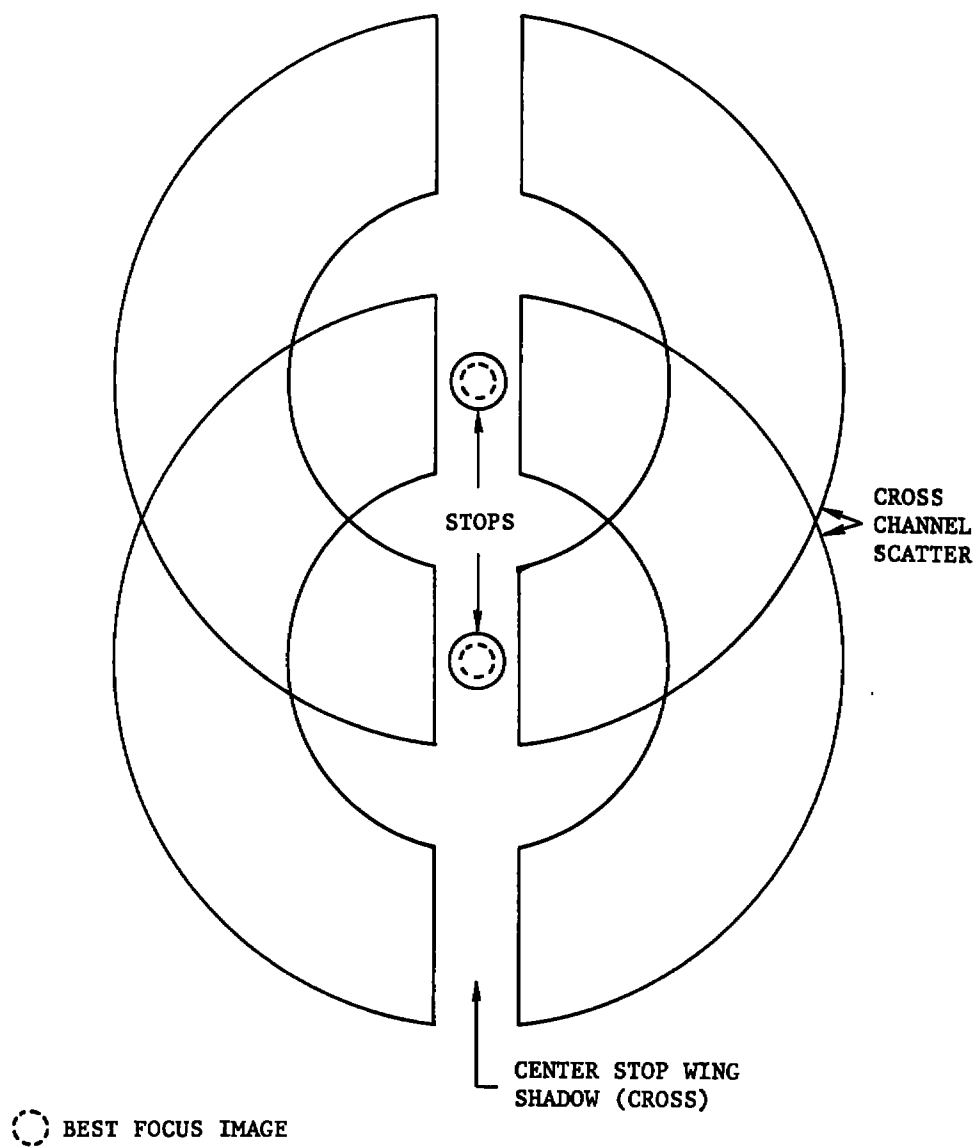


FIGURE 15. RECEIVED IMAGE PATTERN WITH FLARE

illuminating beam: this is usually true for the flare source but the ratio of useful scatter to flare must be reduced by both area and efficiency factors for particles, and, hence, the closeness to the wall in an active experiment has other factors involved. The measurements of focal depth corresponding to the quantification of geometrical properties are summarized on Table 7.4.37 of Appendix III.

4.4 WALL PROPERTIES

Recent tests (Reference 24) and a demonstration in a transonic axial compressor at the Naval Postgraduate School, Monterey, confirmed the desirability of having the internal surfaces close to which measurements are required finished in matt black. Aluminum may be black anodized satisfactorily; otherwise, a black paint which dries to a texture similar to that of the base material is acceptable. In the tests reported in Reference 24, the original blade finish was translucent fiberglass and this was not acceptable. Black painting produced an adequate improvement. Data were obtained without seeding within 0.2" of walls 'square on' in this test, but that was before (and a significant motivation for) the invention of the cross stop. Seeding was finally used to increase data rate, but the size of particle which may be used as a signal source depends on how much external flare must be tolerated.

For windtunnel applications, flare is much less of a problem since the sampling volume need not normally be so close to a material surface.

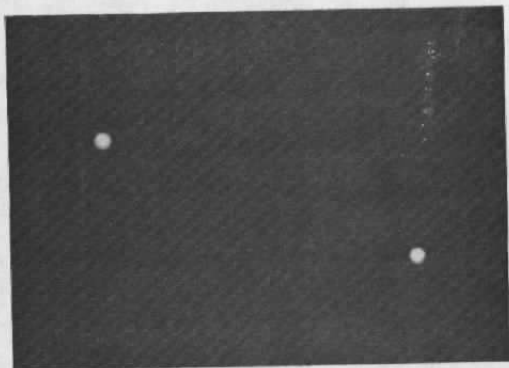
4.5 WINDOW THICKNESS EFFECTS

An analytical and computational study of the spherical aberrations introduced by windows of different thicknesses and material is presented as Appendix VI of this report. The Appendix presents graphic simulations and parameter design curves. The results show that typical applications

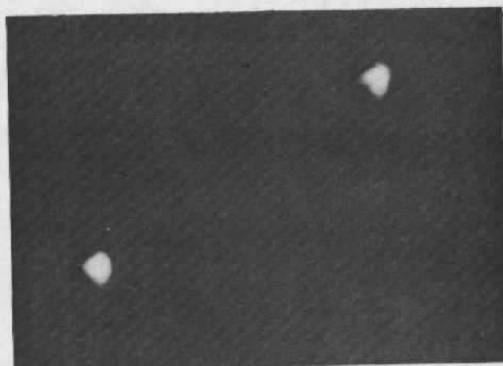
in windtunnels with windows less than 2" thick do not suffer appreciable degradation for near normal incidence. For either thicker windows or incidence in the neighborhood of 25° , there is serious degradation from tangential and sagittal astigmatism and the qualitative effects are shown here as Figures 16 through 20.

Figure 16 shows the appearance of the spots at normal incidence through a 4" window of optical glass of Schlieren quality. Figure 17 shows the 'disc of least confusion' for 15° incidence and Figure 18 shows the same for 25° off axis inclination. The Figures 19 and 20 are the tangential and sagittal foci, respectively, and show that the system will not operate at all satisfactorily in this geometrical configuration.

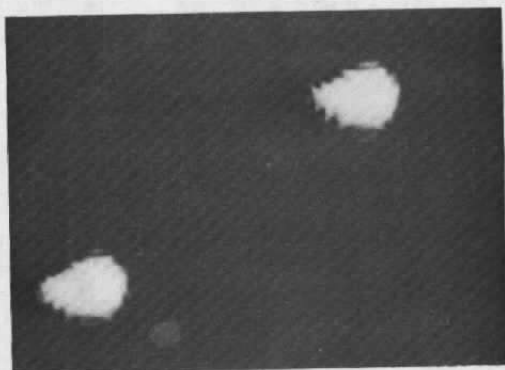
Quantification of the astigmatic defects has not been carried to the same lengths as the spherical defects in Appendix VI.



16.



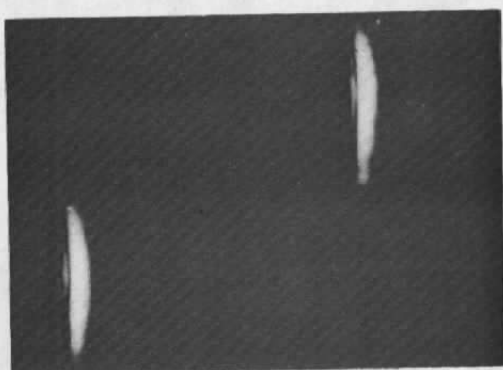
17.



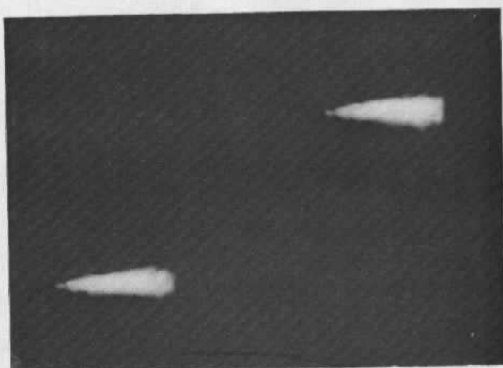
18.

Figure

- 16. Spot Appearance Through Normal 4" Window.
- 17. Spot Appearance Through 15° Inclined 4" Window.
- 18. Spot Appearance Through 25° Inclined 4" Window. (Disk of Least Confusion)
- 19. Spot Appearance Through 25° Inclined 4" Window. (Near) (Tangential)
- 20. Spot Appearance Through 25° Inclined 4" Window. (Away) (Sagittal)



19.



20.

SECTION 5.0

A.E.D.C. DEMONSTRATION

Equipment constructed along the lines of the earlier part of this report was shipped to A.E.D.C. on September 4, 1979, preparatory to feasibility tests on whatever of the VKF tunnels was available in the following two-week period. In the event Tunnel A (at a fixed Mach No. of 4.5) was available for several hours on the night of September 10th and Tunnel B at Mach No. 8 available for the 40 minutes run up to condition and 5 minutes at condition on the night of September 11th.

5.1 EQUIPMENT SETUP

The first few days were spent in laboratory checkout and performance verifications with some last minute improvements in motor calibration precision, discriminators and spot spacing calibration. This last was probably good to about 1% or better. The angle of spots was not calibrated for this exercise as we were interested in precision, not absolute accuracy - there was also no horizontal datum referred to the tunnel because of the type of stand used.

Two output lenses were used, the standard 400 mm Tropel and a newly obtained 600 mm, whose performance as a lens appears excellent, but in this installation was less effective because of its larger focal length. The performance of this machine depends typically on the fourth power of the focal length and is thus five times worse with the 600 mm lens. The way that the performance is defined is extremely complex and this simple rule is not totally correct, but may be a useful guide. Effects of increasing focal length are larger spots and separation (same ratio), longer probe volume (squared), smaller collection aperture and possible small changes in aberrations. The final configuration used on these tests is summarized in Table I.

Table I.

Laser Power	80 mW (40 mW/spot)
Throw	400 mm
Spot Size	12-14 μm
Spot Separation	585 μm
Size to Separation Ratio (For 600 mm lens separation was 875 μm with other parameters scaled)	$\sim 1:40$
P.M.T. High Voltage A	1667 V
P.M.T. High Voltage B	1750 V
Window Thickness	
Tunnel A	1.75"
Tunnel B	1.25"
Discriminator Ranges Used	00, 0, 1
Preferred } { Tunnel A	0
Range(s) } { Tunnel B	00 and 0

During the Tunnel A test, the optical head was mounted upon a cantilevered platform which was prone to vibrate so that it was quite unpleasant to place a hand on the unit. The head suffered this level of vibration throughout the entire shift - 7 hours more after the results reported here were obtained - without any noticeable deterioration of alignment nor electronic unreliability. This gave us some confidence in the head engineering and illustrated suitability for long-term operation without serious maintenance.

Figure 21 shows the installed system in Tunnel A and Figure 22 a better view of the optical head with the beams clearly visible in the fogging condition at startup and for 77 minutes until the fog cleared such that a signal was obtainable, and the laser beam became almost invisible. Figure 23 shows the installation in Tunnel B where the optical head was slid on to the rails of an existing traverse assembly which was already set up for the test. This simple mounting meant that the head and all the rest of the equipment could be removed in five minutes, after the tunnel reached condition and reverted to the prime user. In this five minutes, the results reported here were obtained.

The optical head was supported by the stand-alone data management system shown in Figure 1 and interfaced to a 96 store 50 ns K7023 Malvern correlator kindly loaned by Mr. J. F. Meyers of NASA Langley who witnessed these tests.

The simple program in the present data management system was used to estimate mean speed and angle and it is noted that better estimates may be made with more sophisticated software. This was not significant here as the precision was more dominated by the statistical properties of the small numbers of events leading to estimates. Somewhat surprisingly, for low turbulence flows, the precision of velocity estimate may be much greater than the store spacing of the correlator. At some of these measurements the peak was only ~9 stores from zero, but as long as the occupation number of each store is adequate, a velocity estimate to a fraction of a percent may be made by interpolation.

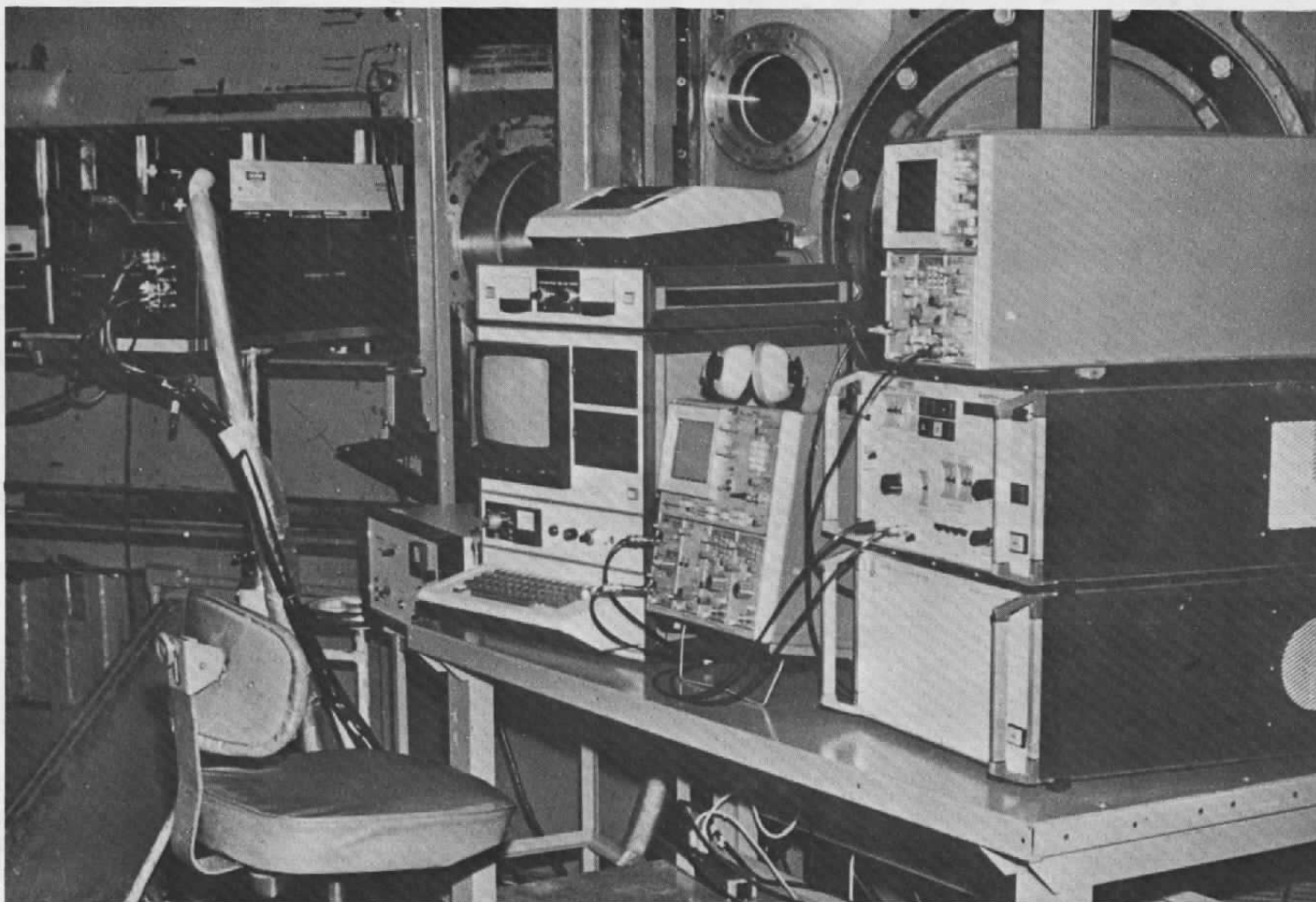


Figure 21. Installation of System in Tunnel A (Mach 4.5).



Figure 22. Optical Head with Beams Entering Fog in Tunnel A.

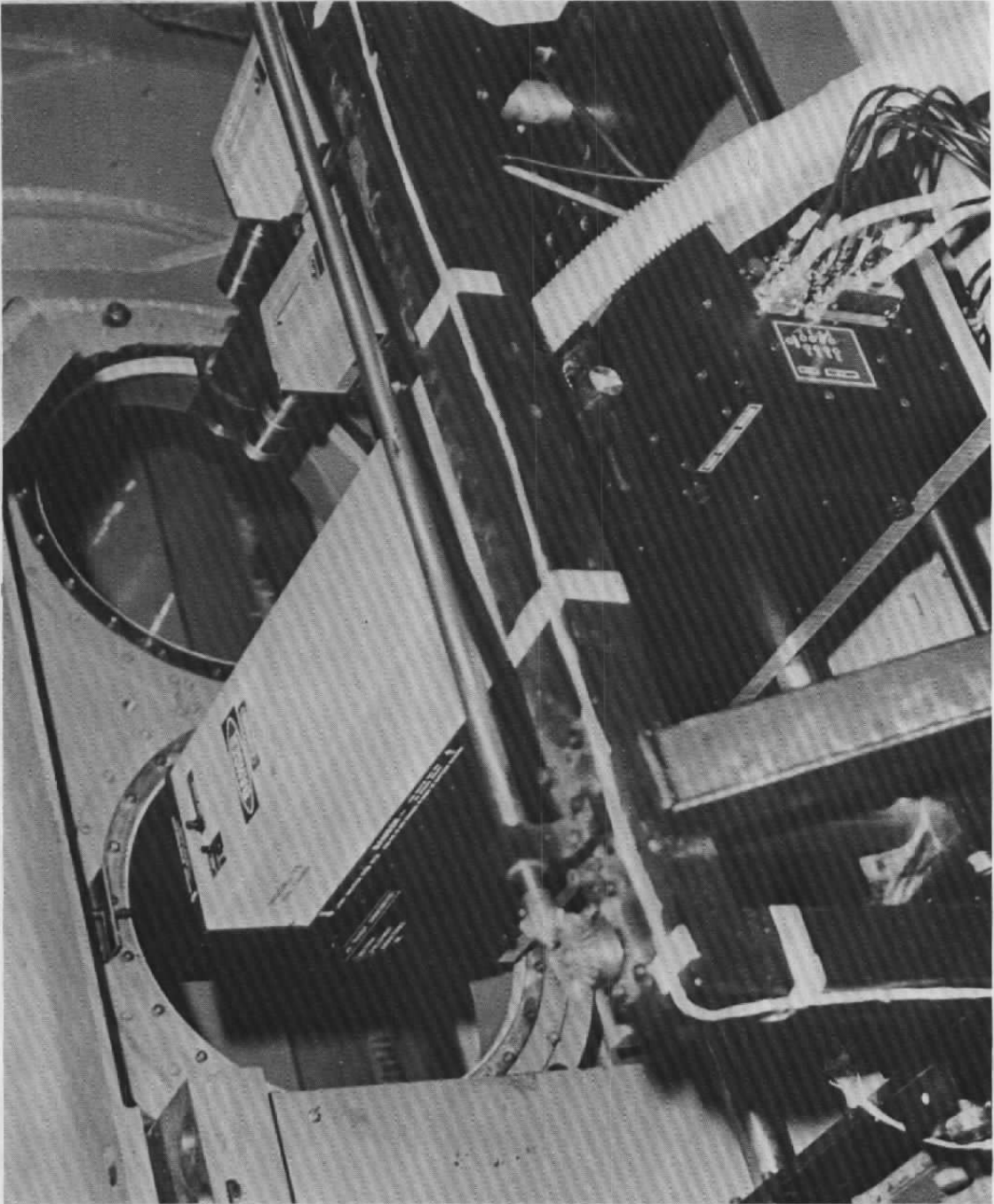


Figure 23. Installation of Optical Head in Tunnel B (Mach 8).

The printout from an experiment performed with the present software yields a data record of which Figure 24, taken from the Tunnel A sequence is a fair example. An explanation of the legend for this figure is as follows: The top graph is a print of the first 25 correlogram stores normalized to 5 units on the ordinate. The abscissa is store number with tick marks every ten. The vertical line represents the nearest resolution element of the pointer to the calculated peak taking one store on either side of the maximum store as a potential contributor to the mean velocity once the background is subtracted. DTHETA is the angular step through which the machine thinks it should search to find the best estimate of flow angle. This is based on an estimate of longitudinal turbulence from the correlogram and assumed isotropic variation. It is not critical to the correct estimate of angle so long as the probability of transit declines on either side of an angle at which a measurement is made (see the lower graph on this figure).

T-ACT is the angle at which the measurement was made and T-REQ is the angle to which the prism was sent and should have settled to. The readout precision is $\pm 0.1^\circ$ arc.

V is the estimated velocity based on mean transit time inversion using knowledge of the spot spacing.

TI is an estimate of turbulence intensity and is quite meaningless in the context of this experiment and software. It should be ignored.

N is the number of angles at which experiments are to be performed and is a manual key entry.

X is a new number identifier for the test.

Y & Z are spare identifiers, normally associated with a traverse if used.

DISC is the discriminator card slot selected (2 here) and, in this case, corresponded to Range 0 (See Appendix III, Table III).

IDEAL is the range which the machine calculates to be most appropriate and is wrong in this case because the divergence of the Wollaston prism was different from that in the software. If the spot/separation ratio is changed, the calculation which infers transit time of a spot from the transit time between spots must have its input constraints changed.

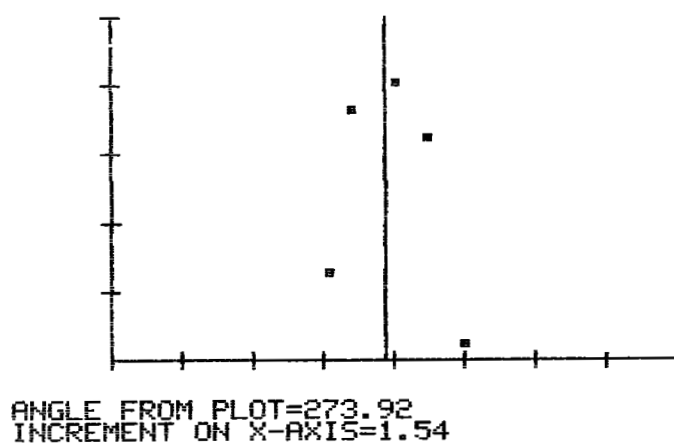
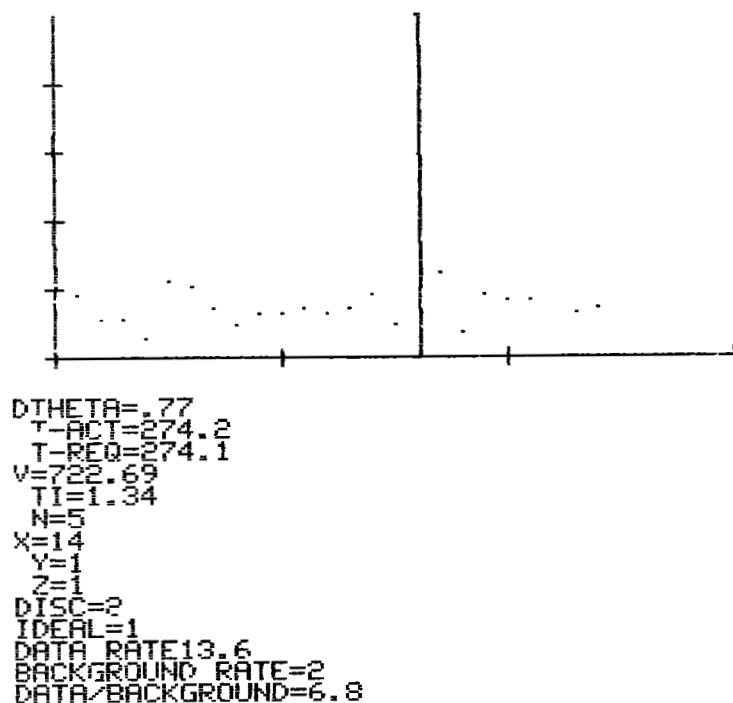


Figure 24. Printout of Correlogram and Angle Plot from Tunnel A

DATA RATE is the number of correlated events received per second of observation.

BACKGROUND RATE is the mean occupation number increase per second of the stores corresponding to background (away from the correlation peak). See Reference 25 for more details of this.

DATA/BACKGROUND is the quotient of the above two properties and is a somewhat arbitrary parameter which does give an indication of the quality of the correlogram; that is, the number of correlated events which were observed compared with the number which constitutes background.

An analogous figure is used to compute the curve of the lower graph where the figure of merit is now the visibility ratio which is defined and explained in Appendix I. This is usually sufficiently accurate to enable estimates to better than 0.1° arc if enough events are available.

The tick marks on the abscissa have their size listed under the graph. It is usually an odd quantity because of the method of calculation and the simple software graphics. The mean flow angle is obtained from a parabolic fit of the highest three adjacent points, which, provided sufficient data is obtained to reduce statistical noise, is a very good measure of most probable angle despite the non-linear assumptions in the angular fit.

5.2 TUNNEL A RESULTS (MACH 4.5)

On startup, Tunnel A was filled with dense fog that produced opacity, multiple scattering and many particles in the probe volumes simultaneously. As the fog cleared after about an hour, it became sufficiently optically thin to allow clean observation of the probe volumes which were still filled with very many, very small particles. This is in marked contrast with previous windtunnel results in the

6' x 6' Transonic Facility at NASA Ames (Reference 25) where the fog cleared to fewer particles which were rather larger and less than one of them in the volume at one time.

As Tunnel A became even cleaner, signals were obtained (77 minutes after startup) and were from very small particles. Our hypothesis is that the tunnel fogging serves as a mechanical condensate scrubber which removes most particles, upon which moisture might condense, with the water as part of the drying process. Later, the tunnel contains only very small particles, and only those in relatively small numbers. As measurements were obtained, they were typically giving rise to no more than two or three collected photons against a background of single photon events. Fortunately, this condition is tolerated by the SDL discriminators and data was retrievable. Some care was required with threshold selection and tube voltage balancing, but data were then quite acceptable.

Oscilloscope photographs were not adequate to show the signal from the monitors, but Figure 25 shows a picture of the discriminator output. The arrow shows the second events which are only just discernable. The correlation, however, demonstrates these perfectly as shown by Figure 24, one of the correlograms obtained, together with some house-keeping data and an angular search, as listed in the previous section.

Many such points were obtained at various conditions of experimental parameters and those which merit discussion are identified in Table II and the following notes: Photomultiplier voltages were varied a little to fine tune A and B rates, but finally selected a 1667 V for A and 1750 V for B and held constant thereafter. The experiments listed in this table were by way of preliminary attempts and demonstrate clearly that the experiment is feasible and that moderately consistent data may be obtained over a range of equipment parameters. To quantify these parameters for maximum precision, the next few runs were performed with various threshold levels to explore and find optimum levels. Table III shows the raw data and Figure 26 is a plot obtained from certain aspects

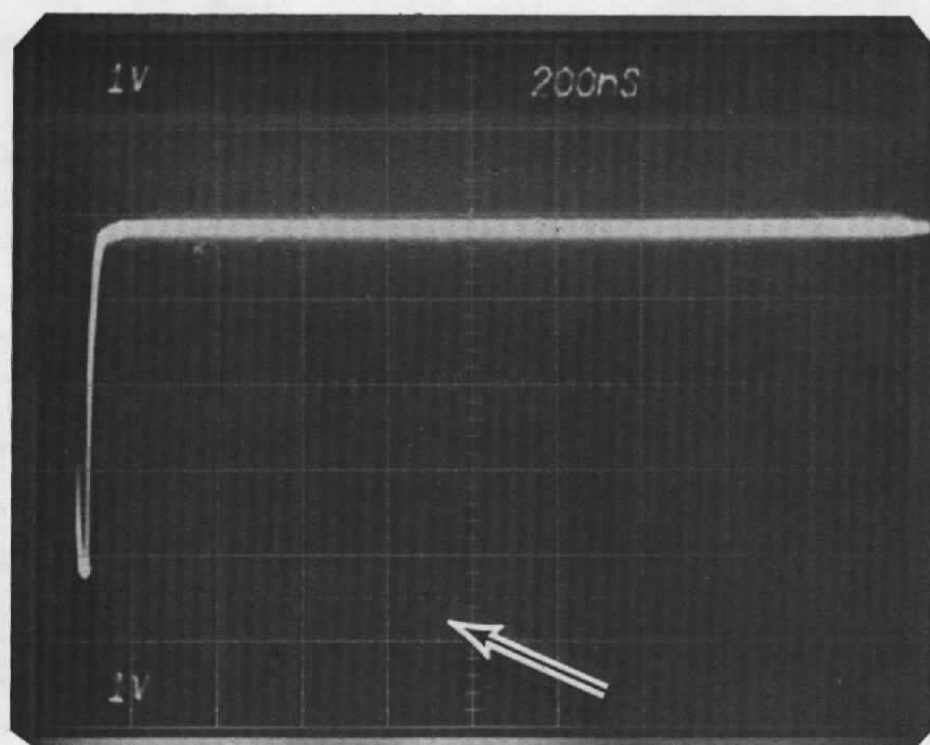


Figure 25. Discriminated Output Signal from Tunnel A.

Table II. Tunnel A Data (9/10/79)

<u>Run No.</u>	<u>Time</u> C.S.T.	<u>Velocity</u> ms ⁻¹	<u>Angle</u> °arc (arbitrary)	<u>Data Rate</u> s ⁻¹	<u>D/B Ratio</u>	<u>Notes</u>
1 & 2	20:47	-	-	-	-	Fogging
3	20:55	728.48	274.17	54	4.8	
4	21:02	732.98	273.90	52.1	2.5	a
5	21:12	725.20	274.01	49.2	17.2	d
6	21:16	726.17	274.10	35.6	3.2	a
7	21:25	723.32	273.97	21.6	37.3	b, d
8	21:35	726.49	274.01	18.14	82.8	d
9	21:38	733.03	274.14	24.1	2.0	
10	21:49	731.91	273.81	9.6	5.1	b, d
11	22:11	702.36	274.08	2.4	2.4	c, d
12	22:15	699.14	274.02	3.9	3.7	c, d
13	22:21	698.24	273.93	3.2	2.5	c, d
14	22:32	722.69	273.92	13.6	2.0	

Notes:

- a: Range 00
 b: Range 1
 }
 All other Range 0.
- c: 600 mm lens, all others 400 mm lens.
 (different calibration, error is possible).
- d: Smooth angular search curves.

Table III. Tunnel A Data (9/10/79)

<u>Run No.</u>	<u>Time</u> C.S.T.	<u>Event Rate</u> $\frac{A+B}{2}$ kHz	<u>Threshold</u>	<u>Velocity</u> ms^{-1}	<u>Data Rate</u> s^{-1}	<u>D/B Ratio</u>
15	22:36		1.0	-	-	-
16	22:37		2.0	-		
17	22:39		3.0	733.54	38.8	.2
18	22:40		4.0	718.42 [†]	15.5	3.8
19	22:41		5.0	717.95 [†]	8.9	104
20	22:42		6.0	-		-
21	22:53	147	3.5	-		
22	22:54	76	3.75	718.53 [†]	16.4	1.4
23	22:56	44	4.0	730.63 [†]	14.3	3.5
24	22:57	32	4.25	730.94 [†]	9.6	4.4
25	22:57	22	4.5	726.95 [†]	8.9	9.4
26	22:58	12	4.75	727.10 [†]	9.4	36.7
27	22:59	8	5.0	719.54 [†]	7.7	90
28	23:00	76	3.75	728.46 [†]	11.9	1.0
29	23:03	43	4.0	719.98 [†]	9.9	2.6
30	23:04	30	4.25	725.69 [†]	10.5	6.2
31	23:06	20	4.5	723.57 [†]	11.3	13.3
32	23:06	11	4.75	727.19 [†]	9.7	42.5
33	23:08	8.6	5.0	727.96 [†]	8.9	40.8

[†] Included in Final Average

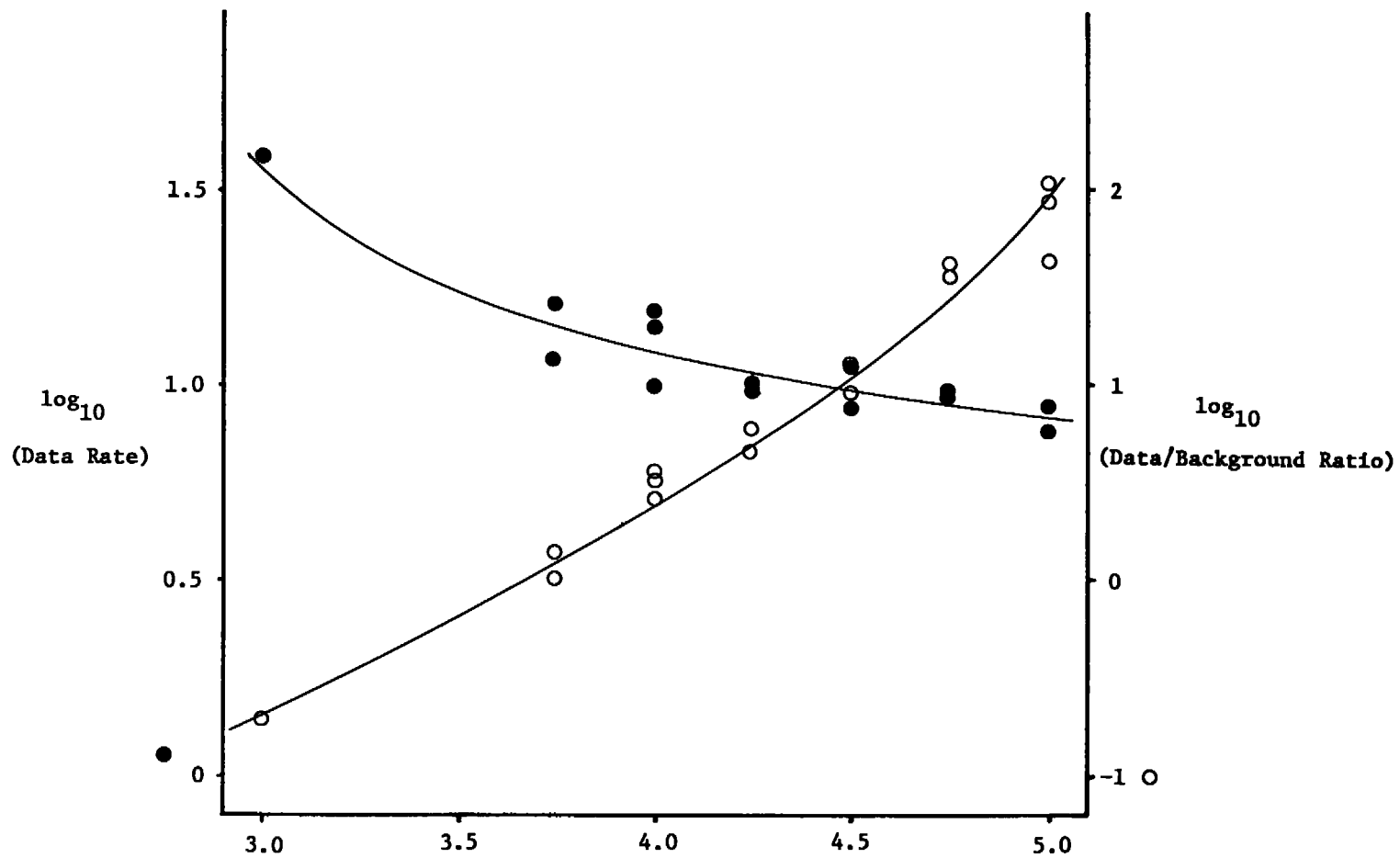


Figure 26. Data Rate and Data/Background Ratio vs Threshold

of the data quality. Here are plotted data rates and data to background ratios for a range of thresholds over which adequate data was obtainable. The range over which these measurements are meaningful at all is plotted as Figure 26 and this range will be seen to be already restricted from ranges in Table III whose rates outside this range make no sense because of the nature of the software and signal statistical properties. It seems that the data obtained within a certain (rather narrow) threshold range is good in that there is no reason to exclude any of it in a systematic basis. Hence, we conclude that experiments at a data-to-background ratio of between 1.0 and 100 seem to yield measurements considered not to contain serious systematic errors.

Figure 27 was a confirmation check to show that there was no correlation between threshold level and mean velocity calculated. Although there is no reason to expect such a correlation, we felt it desirable to show that there was none because the threshold is a manual set and to some extent is not quantified and is thus subject to the experience of the user.

The actual results of these experiments yield a mean velocity of 724.5 m/s with a standard deviation of 0.6%. The stated tunnel velocity calculated from thermodynamic conditions was 720.5 m/s which corresponded to a difference of 0.55%. We have made no attempt to explain this disparity since it could very probably be within the statistical fluctuation expected, or it could be a calibration factor error or non-uniform tunnel properties. We feel that the agreement is well within that which may be expected.

With respect to angular precision, the data on Table II summarizes the results of many angular searches and all lie in a region where the data-to-background ratio has shown that the data is fairly trustworthy. We could have included the velocity data but the tunnel conditions were not quite stable until the results reported in Table III were taken. We did not think that a minute change in velocity could affect the angle. Even the velocity taken over these runs, mean $727.8 \pm 0.55\%$, is not very different from that which was compared with the calibration condition, making the angular figure acceptable.

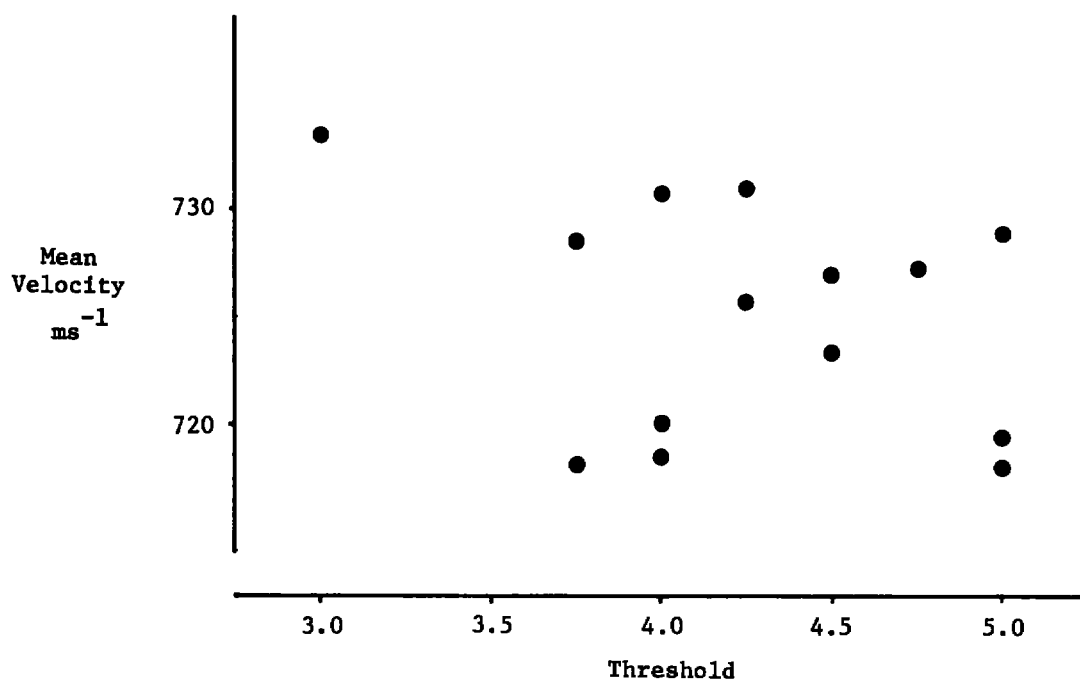


Figure 27. Non-Correlation of Measured Velocity with Threshold

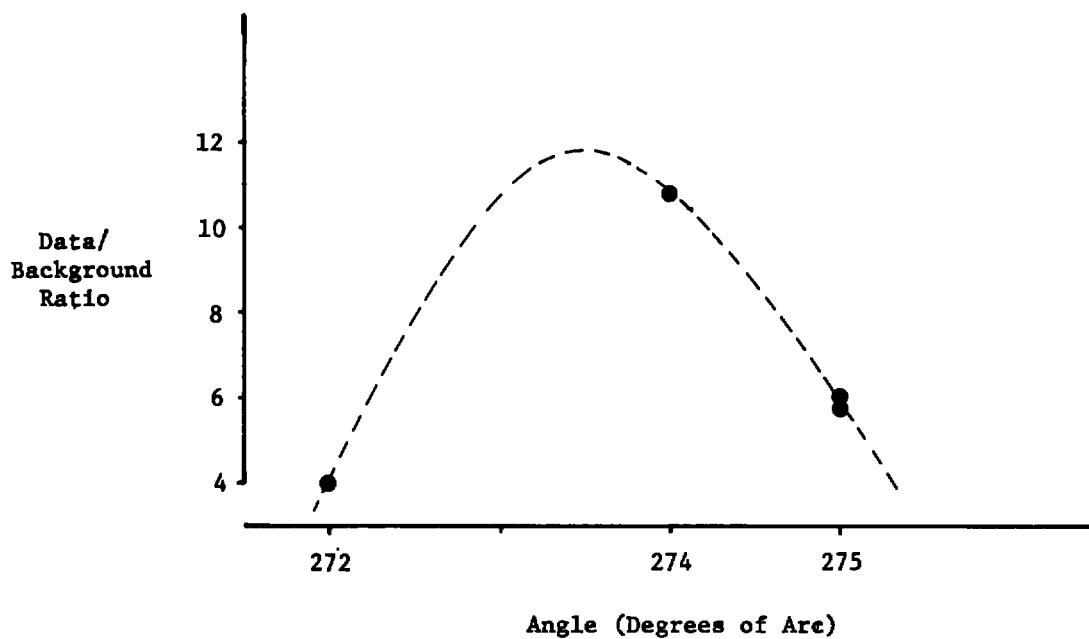


Figure 28. Angular Plot for Tunnel B (Mach 8)

There is no interest in the value of the angle 'per se' because the stand for the optical head could not easily sustain a horizontal calibration but the standard deviation of angle is of great interest and concern. Values of Table II yielded an angle of 274.01° arc with a standard deviation of 0.11° arc which seems a sufficiently precise estimate in view of the small numbers of particles available. Not all the printed angular searches are as smooth as the one shown in Figure 25. If we restrict the above measurement to those with a smooth curve only, then the results are 273.98° arc with a standard deviation of 0.09° arc which is not significantly different.

Each of the results from Tunnel A are based on five-second experiments with numbers of events between 50 and 250 which are relatively small compared with typical numbers considered adequate for most laser anemometry applications.

5.3 TUNNEL B RESULTS (MACH 8)

Tunnel B was available on the night of September 11th during the run-up to condition and for five minutes on condition. The initial operation exhibited fogging similar to Tunnel A, but somewhat less severe. The tunnel took 30 minutes to clear and when it did, no signals were at first visible. An observer (M. Kingery) reported that from the other side of the tunnel, looking toward the sampling volume, no scattered light was visible after fog clearing and during the acquisition of measurements. At 21:26 hr, shortly after the fog cleared, we were given five more minutes and obtained four 50 s runs at four pre-set angles. Table IV repeats the salient features of these.

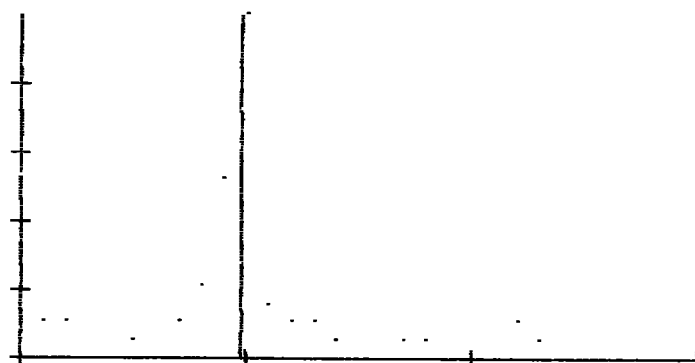
The measured velocity from the four runs was 1205.4 ms^{-1} with a standard deviation of 0.6% compared with a stated figure from thermodynamic tunnel calibration calculations of 1184 ms^{-1} . Thus, we have a disparity of 1.8%. This is not likely to be purely a statistical (3 sigma) deviation. The window was less thick than in Tunnel A and should not have affected the calibration. We cannot explain this

discrepancy. As these runs were taken at somewhat different angles, we have plotted Figure 28. Even with these scant data, the angle is clearly between 273 and 274 degrees and thus may be specified to a half degree with fair confidence. Note the repeatability of runs 32 and 33 with respect to data rate.

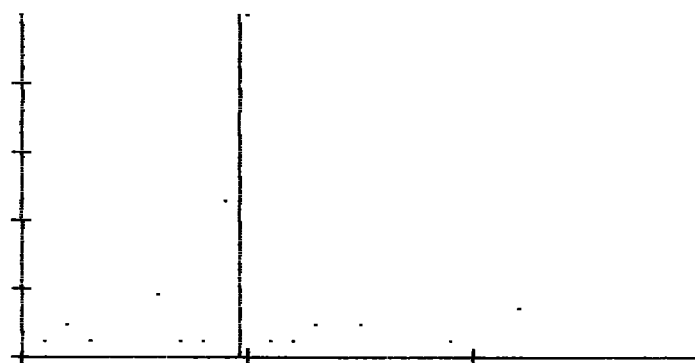
It was not possible to take photographs of the signal from the monitor from this test as there were insufficiently frequent events to register on the Polaroid 3000 film used. The correlation, however, was quite able to produce a well resolved signal such as Figure 29 from which good measurements were obtainable.

Table IV.

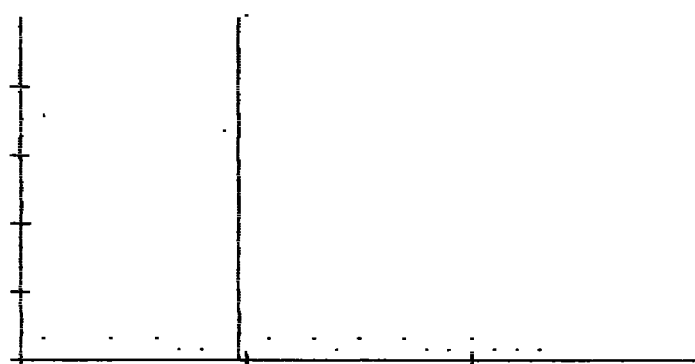
<u>Run No.</u>	<u>Velocity</u> ms^{-1}	<u>Data Rate</u> s^{-1}	<u>Data Background Ratio</u>	<u>Preset- Angle</u>
31	1201.86	4	40	272
32	1198.93	5.8	29	275
33	1205.83	6	34	275
34	1215.12	10.8	51	274



Run 32



Run 33



Run 34

Figure 29. Three Correlograms from Tunnel B

5.4 DISCUSSION

From experience with earlier simulation experiments, the particles from which data were obtained appeared in the size range of 0.2 μm to 0.4 μm diameter with almost none larger than this top limit.

The numbers of events from which these data were obtained are from 20 to 50 depending upon the precision with which the spot alignment corresponded with the mean flow direction. For both a small number of stores and a low occupation number for each store, the velocity precision is impaired to the extent of the fluctuation in occupation number caused by small number statistics.

There are two statistical effects to consider which limit the accuracy of a mean velocity measurement when only a small amount of data is present: first, individual transit time contributions have \pm clock interval errors (which are the cause of the triangular instrument broadening function discussed briefly in Appendix II). Secondly, the number of transit time realizations which occur in the stores either side of the true (for a steady flow) delay obey small number statistics. It is thus easy to see that when data collection time is a premium, and the turbulence level is low, there is an advantage in using a faster correlator with smaller \pm clock interval error per transit so that fewer events are needed to produce an average of a prescribed statistical deviation.

SECTION 6.0

CONCLUSIONS

Spectron Development Laboratories has demonstrated a laser transit anemometer system with improved optical and mechanical design. Aberrations are minimised, flare is well rejected by geometrical stops and the system is rigid and stays aligned. Initial alignment is by a documented logical sequence of operations.

Studies of spherical aberration caused by thick flat windows indicate that system performance is not much degraded for thicknesses below 1.5 inches for the shortest focal length (400 mm) and thicker for longer focal lengths.

New transit event detection principles and circuitry further improve the acquisition of signal in the presence of what background light remains.

This system has made measurements in unseeded flow at Mach 8.0 in full coaxial backscatter with 80 mW of argon laser light ($\lambda=514.5$ nm) at the AEDC VKF Facility. The ambient particles are thought to be between 0.2 μm and 0.4 μm diameter based on earlier computer simulation studies.

Mean velocity measurements of high precision are possible by interpolation, even with the poor time resolution of the 50 ns correlator. For high precision where only small numbers of events are available a faster correlator of higher precision is desirable.

Angular precision of flow direction to 0.5° arc is relatively easy to achieve with few events for low turbulence flows: 0.1° arc is achievable with larger numbers of events, higher rates or longer experiment times. Accuracy depends on calibration and geometrical levelling.

SECTION 7.0

REFERENCES

1. Barnett, D. O. and Giel, T. V., "Laser Velocimeter Measurements in Moderately Heated Jet Flows," AEDC-TR-76-156, April 1977.
2. Johnson, D. A., Bachalo, W. D., and Moddaress, D., "Laser Velocimetry Applied to Transonic and Supersonic Aerodynamics," in AGARD Conference Proceedings No. 193 on Applications of Non-Intrusive Instrumentation in Fluid Flow Research, published September 1976.
3. Mayo, W. T., Jr., "Modeling Laser Velocimeter Signals as Triply Stochastic Poisson Processes," in Proceedings of Minnesota Symposium on Laser Anemometry, held October 22-24, 1975.
4. Mayo, W. T., Jr., "Digital Photon Correlation Data Processing Techniques," AEDC-TR-76-81, July 1976.
5. Thompson, D. H., "A Tracer Particle Fluid Velocity Meter Incorporating a Laser," J. Sci. Inst. (J. Phys. E.) Ser. 2, Vol. 1, 1968, pp. 929-932.
6. Tanner, L. H., "A Particle Timing Laser Velocity Meter," Optics and Laser Technology, June 1973, pp. 108-110.
7. Schodl, R., "On the Extension of the Range of Applicability of LDA by Means of the Laser-Dual-Focus (L-2-F) Technique," Proceedings of the LDA-Symposium Copenhagen, 1975.
8. Cummins, H. Z. and Pike, E. R., Photon Correlation Spectroscopy and Laser Velocimetry, Plenum Press, New York, 1977.
9. Mayo, W. T., Jr., "Study of Photon Correlation Techniques for Processing of Laser Velocimeter Signals," NASA CR-2780, February 1977.
10. Abbiss, J. B., Chubb, T. W., and Pike, E. R., "Supersonic Flow Investigations with a Photon Correlator," Proceedings of the Second International Workshop on Laser Velocimetry, Purdue University, LaFayette, Indiana, March 22-29, 1974.
11. Smart, A. E., "Special Problems of Laser Anemometry in Difficult Applications," AGARD Lecture Series No. 90, 25-26 August 1977.

12. Smart, A. E., "Applications of Digital Correlation to the Measurement of Velocity by Light Scattering," Conference on Laser and Electro-Optical Systems, San Diego, California, 9 February 1978.
13. Smart, A. E., "Data Retrieval in Laser Anemometry by Digital Correlation," Third International Workshop on Laser Velocimetry, Purdue University, LaFayette, Indiana, 11-13 July 1978.
14. Smart, A. E., "Laser Anemometry Close to Walls," presented at DFC'78, Baltimore, MD, Sep 1978. (Published as Appendix to Ref. 20 below)
15. Mayo, W. T., Jr., "Ocean Laser Velocimetry Systems: Signal Processing Accuracy by Simulation," Third International Workshop on Laser Velocimetry, Purdue University, LaFayette, Indiana, 11-13 July 1978.
16. Smart, A. E. and Mayo, W. T., Jr., "Applications of Laser Anemometry to High Reynolds Number Flows," Conference on Photon Correlation Techniques in Fluid Mechanics, Stockholm, Sweden, 14-16 June 1978.
17. Mayo, W. T., Jr., "A Two Component LDV System with Photon Counting for the NASA Langley V/STOL Tunnel: Preliminary Design Study," Final Report for NASA Contract NAS1-13737, October 12, 1976.
18. Mayo, W. T., Jr., "Fringe LV Photon Correlation Interpretation Program Software Manual," Final Report for NASA Contract NAS1-14963, 11 November 1977.
19. Oliver, C. J., "Correlation Techniques," in Photon Correlation and Light Beating Spectroscopy, H. F. Cummins and E. R. Pike, eds., NATO Advanced Study Institute Series, Series B; Physics, Volume 3, Plenum Press, New York 1974.
20. Mayo, W. T., Jr. and Smart, A. E., "Comparison of Data from the Transit Time Velocimeter with Other Systems Now in Use for Velocity Measurement," AEDC-TR-79-32, May 1979.
21. Mayo, W. T., Jr., "Semiclassical Processing of Laser Transit Anemometer Signals," presented at the 3rd International Conference on Photon Correlation Techniques in Fluid Mechanics, Churchill College, Cambridge, United Kingdom, 21-23 March 1979.
22. Mayo, W. T., Jr., and Smart, A. E., "Laser Transit Anemometer with Microcomputer and Special Digital Electronics: Measurements in Supersonic Flows," Proceedings of the 8th International Congress on Instrumentation in Aerospace Simulation Facilities, Naval Postgraduate School, Monterey, CA, September 1979. (Included here as Appendix I)

23. Smart, A. E., "A Compact Wide Aperture Image Rotator Without Aberrations," submitted to J. Phys. E., April 1979.

24. Smart, A. E., Wisler, D. C. and Mayo, W. T., Jr., "Optical Advances in Laser Transit Anemometry," submitted to ASME 1980 Spring Annual Meeting Symposium on Measurement Methods in Rotating Components of Turbomachinery, New Orleans, Louisiana, 1979.

25. Mayo, W. T., Jr. and Smart, A. E., "Feasibility Study of Transit Photon Correlation Anemometer for Ames Research Center Unitary Wind Tunnel Plan," Final Report for NASA Contract No. CR 152238, 7 February 1979.

APPENDIX I

LASER TRANSIT ANEMOMETER WITH MICROCOMPUTER
AND SPECIAL DIGITAL ELECTRONICS:
MEASUREMENTS IN SUPERSONIC FLOWS

by W. T. Mayo, Jr., A. E. Smart and T. E. Hunt

Spectron Development Laboratories, Inc.
3303 Harbor Boulevard, Suite G-3
Costa Mesa, California 92626

Prepared For:

8TH ICIASF

INTERNATIONAL CONGRESS ON INSTRUMENTATION
IN AEROSPACE SIMULATION FACILITIES

NAVAL POSTGRADUATE SCHOOL
MONTEREY, CALIFORNIA, USA
SEPTEMBER 24-26, 1979

Sponsored by the Aerospace & Electronic Systems Society of the
INSTITUTE OF ELECTRICAL AND ELECTRONICS ENGINEERS

LASER TRANSIT ANEMOMETER WITH MICROCOMPUTER
AND SPECIAL DIGITAL ELECTRONICS:
MEASUREMENTS IN SUPERSONIC FLOWS

by W. T. Mayo, Jr., A. E. Smart and T. E. Hunt

Spectron Development Laboratories, Inc.
3303 Harbor Boulevard, Suite G-3
Costa Mesa, California 92626

Summary

An advanced laser transit anemometer system has been developed for difficult optical flow measurement applications. This co-axial backscatter system measures mean velocity, flow angle, and turbulence intensity. The use of highly focused spots, special pulse detection circuitry, a fast single bit digital correlator, and a microcomputer data management system allow unseeded subsonic measurements to ranges greater than two meters and supersonic measurements with naturally occurring submicron particles at shorter ranges. The system has excellent wall and window flare rejection capabilities and may be used for boundary layer measurements near solid models. It is compact and rugged and has been demonstrated for supersonic measurements in high noise and vibration environments at both USAF Arnold Center and the NASA Ames Research Center. This LTA system has also been demonstrated for subsonic axial compressor measurements. In recent developments, the speed, sensitivity and reliability have been further improved in preparation for measurements up to Mach 5 at the Arnold Center Von Karman Facility in late summer 1979.

improvements to both the optical and signal conditioning systems. The data management system (DMS) has been improved under SDL private funding. Commercial copies of this even more advanced "fourth generation" system have been constructed and delivered.

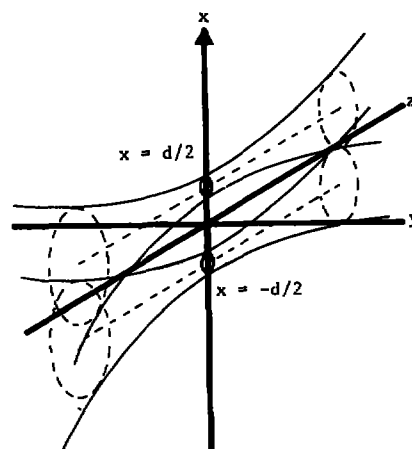


Fig. 1 - Laser Beam Geometry

1. INTRODUCTION

Laser transit anemometry (LTA) or "two-spot" techniques have received attention recently due to sensitivity, high velocity capabilities, and superior flare rejection advantages¹⁻⁷. An LTA system measures the distribution of the times of flight of scattering particles as they pass successively through two highly focused parallel laser beams as illustrated in Figures 1 and 2. The appropriateness of using pulse center estimation filters with real-time single-bit cross correlation and the need for correlation processors with 5 to 10 nano-second time resolution for supersonic flows have both been documented recently^{6,7}.

An advanced co-axial backscatter LTA system was developed and demonstrated by Spectron Development Laboratories under sponsorship by the U.S.A.F. Arnold Engineering Development Center⁵, NASA Ames⁶, and private funding. This system included a third generation compact and rugged optics head with a 135 mW laser, optics, spot-pair rotation, real-time graphic display of correlograms, preliminary on-line data analysis of mean speed, flow angle, turbulence intensity, and mass data transfer or storage for further off-line computer processing.

More recently, additional development funding from the U.S.A.F. Arnold Center⁸ has resulted in

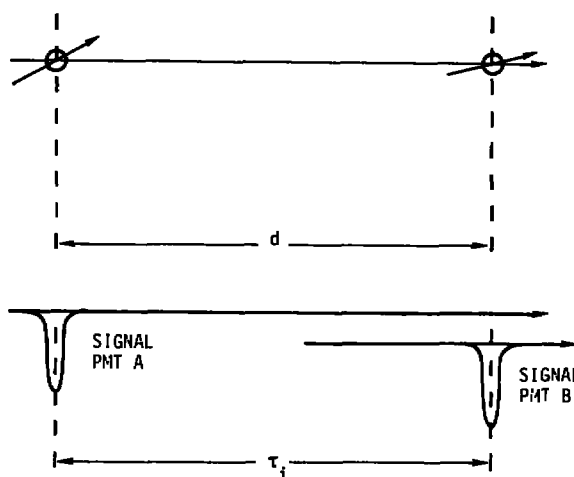


Fig. 2 - Operating Principle $V_i = d/\tau_i$

Following sections describe various aspects of the system and our experience to date. These include the system configuration, signal conditioning electronics, the microcomputer based control and data acquisition subsystem, and display and data reduction algorithms. This is followed by a brief description of supersonic measurements and conclusions about the applicability of this technology.

2. SYSTEM OVERVIEW

Figure 3 is a photograph of the LTA optical head and the data management system (DMS). A digital cross correlation processor (not shown) and interconnection cables complete this stand-alone system, although traverse-mechanism and other interfaces are available. The optical head contains several sets of printed circuit card electronics. These subsystems include a rotator prism control card, two sets of filter discriminators, a high voltage relay circuit, and photomultiplier tube housing circuits. Figure 4 is a photograph of one of the discriminator cards.

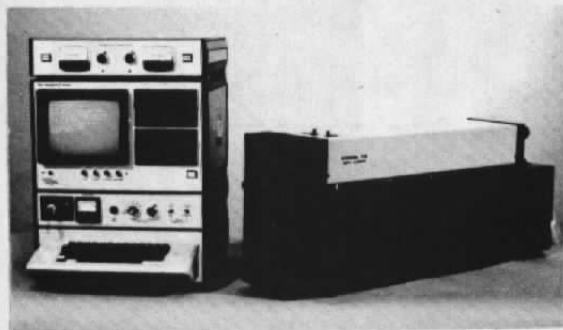


Fig. 3 - LTA Data Management System and Optical Head

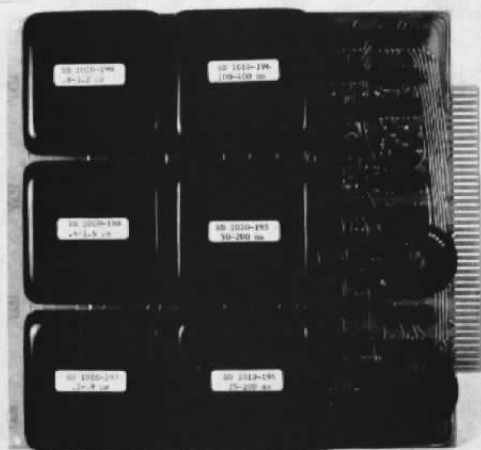


Fig. 4 - Example of Optical Head Electronics: Discriminator Card

During our LTA development, we have used a Malvern K7023 50 ns correlator to produce a single-bit cross correlation of the outputs of pulse-center estimation filters (discriminators). A faster "multiple station" correlation processor is presently under development at SDL for LTA and other applications. Figure 5 is an example cross correlogram of transit delay intervals from a 48 store correlator. The rms turbulence intensity for this example is 7%.

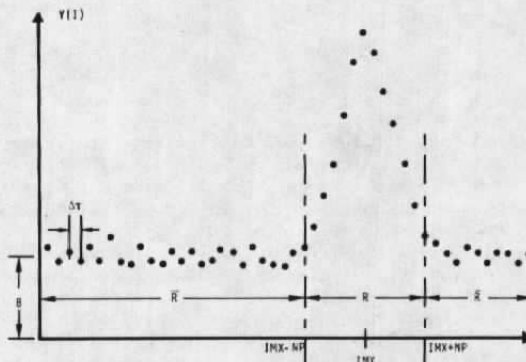


Fig. 5 - An Example Cross Correlogram with 7% RMS Turbulence Intensity

The DMS automatically rotates the two focused beams about a common center through a sequence of angles with the angular step size determined on line from the turbulence level estimated from the first data run. The correlator is started and the data transferred to the DMS in proper sequence. The operator is shown a graphic display of the correlograms, a plot of signal visibility ratio from which mean flow angle is extracted, and a printout of the estimates of mean speed, mean angle, and apparent turbulence intensity.

3. OPTICAL HEAD ELECTRONICS

Through previous experience, one of the authors (Smart) found that large electromagnetic interference fields were often present in common test environments in addition to high levels of noise and vibration. Thus, in addition to designing for mechanical rigidity, we chose to locate the analog electronics inside the optics head where short low-impedance leads and shielding could be used to maintain speed, sensitivity and good immunity to interference. Only TTL level signals are transmitted over the long signal and control cables (30 meters or more).

The photomultiplier tube circuits offered quite a challenge. We desired good single-photon response (pulses up to two volts in magnitude and less than 10 ns wide with little or no ringing and with good single photoelectron pulse height resolution) while allowing much longer classical signals. This must be accomplished in the presence of wall flare and blade flash which, for brief periods, drive the tube

output far beyond the allowed average anode current. The PMTs selected were 12 stage, 2 inch diameter EMI 9817B linear fast focused tubes with S-20 photocathode material. These tubes have high cathode maximum current limits such that the cathode is protected by the inclusion of a series 100 M Ω resistor. Good single photoelectron pulse height response and first stage gain is assured regardless of the high-voltage setting by two series 150V Zener diodes between the cathode and the first dynode.

The inputs and outputs are illustrated in Figure 6. The gain suppression does not disconnect

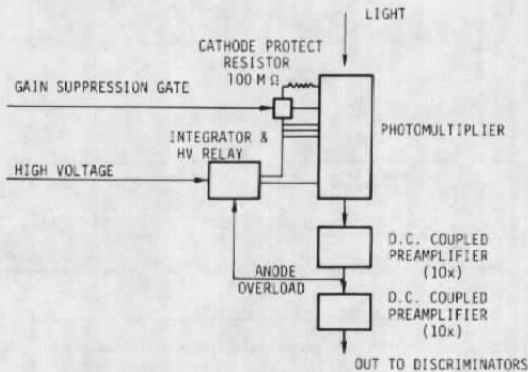


Fig. 6 - Photodetection Electronics.

the high voltage but removes the interstage gain at the first dynode thus preventing predictable transient optical overload from fatiguing the dynode electron emitters. The PMT anode load is 50 Ω . There are two direct coupled stages of preamplification which together give a gain of $\times 100$ and do not change the polarity of the output signal. These preamplifiers saturate at about -6 volts. In general, the use of such preamplifiers is not desirable, and for wind tunnel applications away from model surfaces, a 14 stage tube with one 10x preamp is a better selection. However, the applications of interest often require proximity to walls; thus, the preamplifiers are required to avoid dynode fatigue through excessive average current. Each preamplifier output drives a 50 Ω co-axial cable terminated on a discriminator board. Figure 7 is a photograph of two phototube assemblies which are partially disassembled to show the circuitry.

Between the two preamplifiers there is an integrating monitor, located physically on the high voltage relay board, which detects a condition which could, if sustained, damage the later dynodes or anode of the photomultiplier tube. This trip condition corresponds to a dc anode condition of 200 μ A for a period of 0.5s. The high voltage relay responds to the integrating monitor (actually an active low-pass filter) by disconnecting the high voltage to protect the anode and later stages of the dynode chain. Each tube has a separate sense line and a separate high voltage relay but a red overload light on both the optical head and the DMS

will come on when either tube is tripped. The red light is incorporated in a switch which resets the relays when pushed.

There is a separate discriminator card for each of the two separate photomultiplier tubes. Each discriminator card is a "mother" board with six separate plug-in "daughter" modules as illustrated in Figure 4. Each module is for a pulse width with a dynamic range of 4:1. The ranges overlap, as they increment in powers of two with range 1 being 25 ns to 100 ns, range 2 being 50 ns to 200 ns, etc. Figure 8 illustrates one of the plug-in modules functionally. The low-pass filters are designed to have

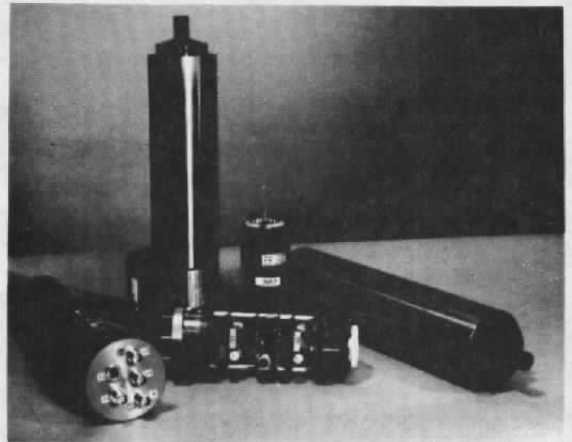


Fig. 7 - Photomultiplier Tube Assemblies

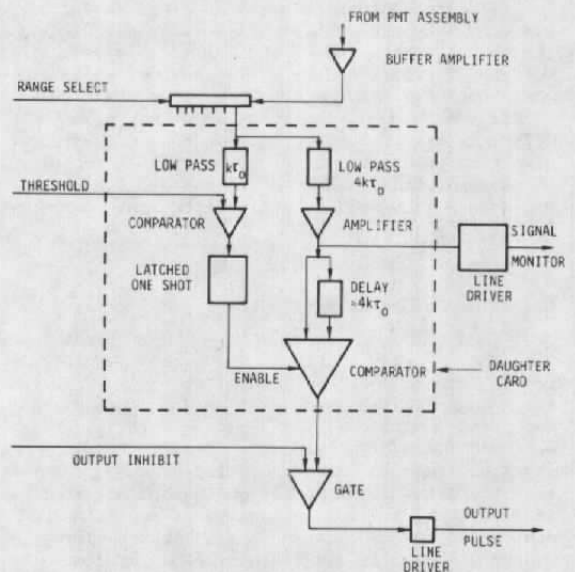


Fig. 8 - Schematic of Single Filter Discriminator Plug-in Module.

nearly symmetric, non-ringing, Gaussian impulse responses whose duration are kt_0 and $4kt_0$ for the detection filter and the pulse center estimation filter, respectively. The range selected is k , from 1 to 6. The $1/e^2$ pulse width τ_0 for the fastest range is 25 ns for the standard units; special higher-speed plug-in modules have been developed⁸ for applications up to Mach 10.

In operation, the user electronically selects the discriminator range for which most of the spot transit durations T_j will lie within the range $kt_0 < T_j < 4kt_0$. Under these conditions, the detection filter (kt_0) has a wider bandwidth than the classical signals to be detected, so there is no statistical biasing due to attenuation of the faster pulses. Once the detection threshold is exceeded, the pulse-center filters are enabled. Since the impulse response of these filters is longer in duration than the spot transit times, the single-photon pulses are smoothed, even when only one or a few such pulses occur in a spot transit group. The comparator thus locates the weighted average center of a photon pulse cluster.

The discriminator cards include a second level detection circuit just following the buffer amplifier which is not shown in the simple block diagram. This circuit inhibits the discriminator outputs if the signals exceed a preset level. The preset level is typically -2.5 volts to avoid very large impulses (from large scatterers or other causes). By adjusting the PMT high voltage supply, the average pulse level out of the preamplifiers is set between -0.2 and -2.0 volts.

The motor control board supplies power to the dc geared motor which drives the prism rotator such as to zero the difference between the logic word provided by the microprocessor and the analog-to-digital conversion of the signal from the potentiometer connected without backlash to the prism rotator. For incremental angle steps less than 2 degrees, 0.1 degree precision is obtained in less than 0.5s. The value of the instruction dispatch word is displayed at the microprocessor as is the word which corresponds to the angular position ultimately obtained. The prism motor may also be driven in either fast or slow mode in either direction from the manual switches on the DMS console. In this mode the readout of actual position to the DMS screen is sustained and updated many times per second.

4. DATA MANAGEMENT SYSTEM (DMS)

The DMS (see Figure 3) is normally situated remote from the optical head by up to 30 m and contains the microprocessor, keyboard, visual display unit, two mini floppy disk units, operating software and a number of manual controls. Figure 9 shows the labeled front panel layout which identifies the items shown in the photograph of Figure 1. Inside, there are low voltage power supplies and other electronic hardware to augment the microprocessor. These are 48k bytes of RAM, interfaces, and the window and delay unit (one channel of which controls the "live time" of one discriminator and the other the "blanking time" of both photomultipliers for periodic flow applications.) The

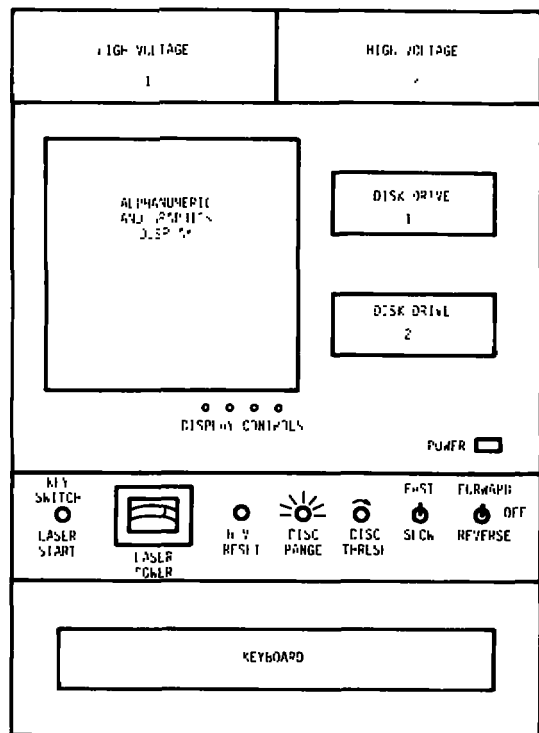


Fig. 9 - Data Management System Front Panel

parallel ports (interfaces) provided in the DMS include a buffered 8 bit duplex computer interface with four additional control lines and a 48 bit correlator interface. The correlator ports are programmable with respect to the direction of information flow. Thus, interfaces to a variety of other computers and correlators may be configured by software without hardware changes. Since all software is provided on disk rather than permanent read-only memory, the system is quite flexible.

Software as provided is read from Disk 1 on startup and Disk 2 is reserved for data storage. Either will serve both functions, if necessary. All initiation and data heading functions are entered from the keyboard in response to questions posed on the screen as illustrated in the example given in Table 1. These keyboard entries are written as initialization heading before each data record. Further details concerning the data processing algorithms are presented in Section 5 below.

The photomultipliers are each supplied from their own high voltage supply so that fine tuning on gain may be performed. The remote laser start/safe is a removable key switch with laser-ready indication. This prevents the need for access to the laser power supply except when one wishes to change power levels or the control mode. There is a laser output power meter on the control console. Manual controls which may override the computer are

Table 1 - Example of Data Entry Prior to Run

DMS PROMPT TO USER	EXAMPLE OF ENTRY
PUT IN DATA DISKETTE	Confirm that this is done
DATE (MONTH, DAY)	12, 25
NO. OF STORES = ?	48 (48 store correlator)
SPOT SEPAR (MM) = ?	0.27
NO. OF BLADES = ?	29
WINDOW WIDTH FOR GATE SIGNAL = ?	Width and Delay in Microseconds
DELAY FOR GATE SIGNAL = ?	
WINDOW WIDTH FOR BLANKING SIGNAL = ?	Width and Delay in Microseconds
DELAY FOR BLANKING SIGNAL = ?	
NO. OF POINTS TO USE ON EACH SIDE OF THE PEAK = ?	7 (See Section 5)
NO. OF DELTA-T'S (POWER OF 10) = ?	6
X, Y, Z = ?	10 25, 3 45, 5 00
TIME (HOUR, MINUTE) = ?	07, 43
DELTA-T (MICROSEC) = ?	0 05
DESIRED RANGE = ?	2 (Discriminator Plug-in)
THETA = [VALUE DISPLAYED WITH REAL TIME UPDATE]	Manual set then return
DESIRED THETA = ?	180 4
THETA = 180 6	
THETA = 180 4	
GO ON?	Hit Return

provided to make setting up the system easier. There is a switch which allows either manual or computer discriminator range selection. Mode switches for motor control to facilitate alignment of the spot orientation with the flow are provided. Even under manual control, the correct prism orientation is read to the screen of the DMS. The threshold control for the discriminators sets over a wide range, the level which changes the ranges the ratio of single photon events to multiphoton particle events.

5. SOFTWARE

The optical and electronic system for transit anemometry basically acquires two channels of digital events whose only information is carried at event times. To measure the distribution of event times, it is optimal to cross correlate the two channels where the delayed channel corresponds to that which a particle crosses first. This subject has been previously discussed⁷. The subject of optimum data extraction from correlograms can get very detailed. Here we will explain what we have elected to do with the system to date. Further software revisions are possible either by the user or from SDL on a new minidisk. The present software functions:

- Make a visible record of data quality so that the user may make on-line improvements to operating procedure, threshold and voltage settings,

- Give an approximate value for velocity, turbulence and angle in minimum time,
- Print these estimates on paper for brief assessment,
- Store or transmit and identify all acquired data for later processing with superior algorithms in a large computer.

Figure 1 is a schematic view of the sampling volume and shows how the velocity is resolved in the axial direction but only gives rise to a measurement of true speed if it is in the plane of the two parallel cylinders. More simply, this can be viewed as in Figure 2. Because there is no way of identifying a specific particle, we have chosen to decode the data on a statistical basis. By computing the times between all possible 'A then B' pairs such that the delay does not exceed the displayed delay time of the correlator, then it is possible to obtain a peak from those particles which crossed A and then B and a background from all others. Over short delay intervals it is permissible to assume that uncorrelated events from particles which cross only one spot or from other random events are Poisson distributed. This is not, in general, true for longer correlation times; and, indeed, provides a method of assessing turbulence scale by correlating the existence of particle concentration fluctuations⁹. Over the short time involved in a typical transit, these effects are not manifest and it is permissible to assume that the "background" is flat. Figure 5 showed a typical correlogram for about 7% turbulence and a 48 store correlator. Upon this plot are marked the various operating parameters which are used by the DMS to evaluate the flow parameters.

There are many simplifications in the following analysis. It is not to be scorned for that, as it is intended as a quick-look device and, if used correctly with proper precautions, is capable of much better than 1% accuracy in velocity, particularly for low turbulence, and no more than a few percent error on turbulence for turbulence up to about 15%. For very low turbulence more stores and/or smaller ΔT correlator resolution may be required. The low turbulence limit also depends on the degree of deconvolution of the instrument broadening function⁷ one may wish to attempt in post-detection processing. The standard algorithms are presented below.

Based on experience and "a priori" knowledge of the flow, the operator selects a number of stores NP which he expects to bound the highest turbulence conditions of the correlogram. The region R is then the set of stores located within NP stores either side of the peak IMX of the correlogram. The region \bar{R} is all the rest of the stores as shown in Figure 5. The first step in the data reduction is to compute the arithmetic average of the values accumulated in the stores of region R. This is an estimate of the "white" level due to uncorrelated background pulses. This value is subtracted from the correlogram. Thus, if Y(I) are the correlogram values, we obtain

$$(1) \quad B = \frac{1}{NB} \sum_R Y(I)$$

where Q is the total "area" under the peak (see Figure 10) which normalizes the function as a probability density function estimate; i.e.,

$$(3) \quad Q = \sum_K Y(I) - B$$

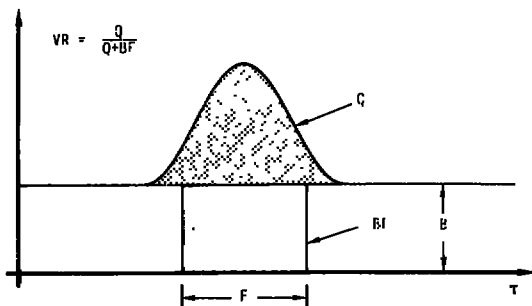


Fig. 10 - Definition of Visibility Ratio

The first order mean speed estimate (assuming that the spot pair axis is directed somewhat along the mean flow direction) is obtained from the mean delay number KBAR quite simply as

$$(4) \quad V \approx \frac{d}{(KBAR \cdot \Delta\tau)}$$

where d is the physical distance between the spots and $\Delta\tau$ is the correlator clock interval. This estimate of mean speed based on the inverse of the mean transit time is similar to the mean velocity component estimate obtained from burst counter processing of fringe LV data without inversion. As is well known¹¹, the use of the inverse of the mean transit time provides first-order correction of the particle rate biasing. Thus, for low turbulence flows the mean speed estimate is excellent. At higher turbulence levels, say greater than 10%, higher order data processing with the inclusion of the "pie slice" effect (accepted flow-angle at any one angle depends on particle size for a fixed threshold) and other effects may be included in a more precise model.

For simplicity the present turbulence intensity estimate, TI, is calculated as a root mean square deviation of the transit time distribution instead of the velocity distribution. This may be improved in the future. In terms of the effective width, F , of the correlogram peak we obtain

$$(5) \quad FI = F/2KBAR$$

where this somewhat unusual notation is used in the definition of the signal visibility ratio function below:

$$(6) \quad F = 2 \sqrt{\sum_K (I - KBAR)^2 \cdot \frac{Y(I) - B}{Q}}$$

The above formula for mean speed is quite insensitive to the values of NP chosen. If the data acquisition time is so short that the scatter in

the baseline is considerable as illustrated in Figure 5, then the turbulence intensity estimate becomes significantly affected by the noise on the baseline and, hence, the choice of R and \bar{R} . Under such conditions, more data should be acquired or more elaborate curve fit parameter extraction algorithms should be employed for optimum retrieval of information from the data.

The DMS uses the estimate of turbulence intensity to compute an incremental angle $\Delta\theta$ for spot-pair rotation which proceeds automatically unless another $\Delta\theta$ is chosen. The computation of $\Delta\theta$ assumes that the turbulence is isotropic to obtain a crude estimate of a "good" $\Delta\theta$. Thus, if the number of angles at which observations are to be made is N , then $\Delta\theta$ is computed as in Table 2.

Table 2 - Selection Formula for $\Delta\theta$

N	DT
3 -	$1.5 \times TI \times 180/\pi$
5 -	$1.0 \times TI \times 180/\pi$
7 -	$0.7 \times TI \times 180/\pi$

Unless $TI = 0$, in which case

$$\begin{aligned} 3 - & 1.5 \times 0.02 \times 180/\pi = 1.72 \\ 5 - & 1.0 \times 0.02 \times 180/\pi = 1.15 \\ 7 - & 0.7 \times 0.02 \times 180/\pi = 0.80 \end{aligned}$$

and TI is displayed as ≈ 0 .

During the automatic angle incrementation sequence, the signal "visibility ratio," $VR(L)$, is computed. The angle is $\theta_1 + L\Delta\theta$ where θ_1 is the initial angle selected manually or via computer. The quantity $VR(L)$ is the ratio of the area under the delay curve, Q , and the sum of this area with that portion of the background within the "width" F of the correlogram:

$$(7) \quad VR(L) = \frac{Q}{Q + BF}$$

These quantities are illustrated in Figure 10. The value of the function $VR(L)$ lies between zero and unity. The zero condition is obtained when the spot pair axis is rotated so far away from the mean flow angle that no correlated events occur and Q goes to zero.

The mean flow angle occurs in the vicinity of the peak of the plot of $VR(L)$. The present DMS software uses a 3-point parabolic fit of the peak and the value of $VR(L)$ on each side of the peak to obtain the mean flow-angle estimate as illustrated in Figure 11. The idea behind the definition of the visibility ratio function is that it removes the effects of particle rate fluctuations when the threshold is set sufficiently high for all detected pulses to be from particles. At lower thresholds and particularly when the probe volume is near a flare producing surface, many of the detected pulses are single photoelectron background pulses whose rate may be subject to angular orientation of the spots. Under such conditions, the raw data rate Q which has background subtracted out, may be

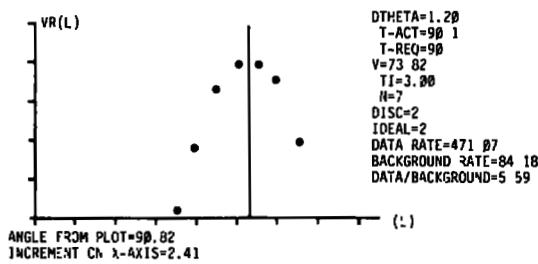


Fig. 11 - Example Screen Plot of VR(L) and Display of Reduced Data.

a better parameter to fit for mean flow angle. All of the flow estimation software is written in BASIC to allow ease of future modification. In fact, all of the operating software is provided on disk, rather than permanent memory and can easily be changed.

6. MEASUREMENTS

At the time of this writing (July 1979) additional supersonic measurements are scheduled to be conducted at the Arnold Engineering Development Center Von Karman Facility, but these will not be conducted before the submission deadline. These tests will be through windows two inches thick, without seeding, in Tunnel A at Mach numbers in the range 1.5 to 5.0. The results of these tests will be described at the Congress if they are available at that time, and will be provided later in other publications. In this section we will briefly review the supersonic measurements made with the prototype system at the Arnold Center, September 1978, and at NASA Ames, October 1978. These experiments are described in more detail in the contract reports^{5,6}.

The objective of the AEDC measurements was to demonstrate an LTA system with a digital correlator and to compare the measurements with simultaneously obtained fringe velocimeter measurements. The prototype system was transported to the Arnold Center on September 18, 1978. Demonstration measurements along the centerline of a supersonic jet with a Mach disk were made, with the LTA system; however, due to equipment difficulties experienced by the Arnold Center personnel and time and funding constraints which precluded further SDL measurements, no simultaneous measurements were accomplished.

The AEDC tests were conducted using a free jet test (unseeded) installation located in Propulsion Research Cell (R-1A-1) of the Engine Test Facility at the Arnold Engineering Development Center. Assistance was provided to SDL personnel by Mr. T. V. Giel, ETF, Mr. Virgil Cline, PWT, and the facility technicians. A 1" diameter underexpanded unheated jet with a pressure ratio of 4 was used. This jet has been tested extensively in the past with both laser velocimetry and shadowgraph techniques as reported by Barnett and Giel¹⁰ in 1977. The first and second Mach disks were located 1.73 inches and 3.39 inches downstream¹⁰. Due to other activities which had occurred since the calibrations of the

jet, a right angle bend had been installed in the jet supply pipe. It is thus possible that differences in the flow would occur with respect to the earlier measurements.

The output lens used for the jet test was a 622 mm focal length lens which resulted in a throw, or range, from the front of the instrument of 597 mm, a spot separation of 0.489 mm as calibrated prior to instrument shipping, and a spot size of approximately 20 micrometers diameter. The axial speed and apparent turbulence intensities as determined by the operator and the data management system were recorded for several locations along the center line of the jet. Figure 12 is a plot of the axial speed measured along the jet centerline.

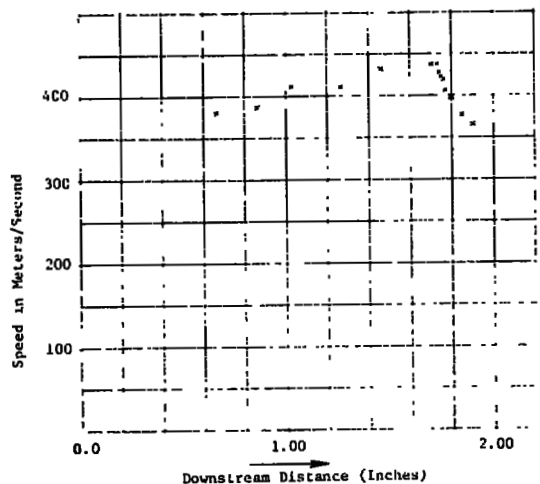


Fig. 12 - Axial Speed on Jet Centerline.

Careful study of all the AEDC data and the apparatus indicated that the selection of the collimator lens for the prototype system was inadequate to properly focus return scattered radiation on to the fiber optic light guides employed in the system. The resulting loss of scattered radiation resulted in a receiver efficiency of less than 5%. Calculations had indicated that measurements from particles down to 0.3 micrometers in diameter would be achievable. The particle lag evident in the plot of data across the Mach disk indicated that the first prototype system did not achieve this sensitivity. Contractual time and funding limitations prevented further data collection or analysis at that time.

The purpose of the NASA Ames experiment was to obtain data for design of a larger future system for the NASA Ames 11-foot transonic tunnel, if such a system appeared feasible from the tests. The test was more difficult than the AEDC test in that there was a 2-inch thick window between the LTA system and the flow field, and the larger particles impact out of a recirculating tunnel. The measurements were conducted in a piggyback test at the 6-foot transonic tunnel without seeding at Mach numbers from 0.6 to 1.6. Repeatability of the mean flow

measurements was as good as 0.15%. The tunnel was not seeded. Minor improvements in the optical system had been made to improve the optical efficiency of the receivers to nearly 10% but insufficient time had been available to replace the output collimator. Computer simulations of the signals using Mie scattering codes and measured optical parameters indicated that data was obtained from particles down to about 0.5 micrometers in diameter, but no standing shocks were available for relaxation tests in this exercise.

In December 1978, the prototype system was used to make measurements in a research axial compressor at the General Electric Co. Some of the data was obtained unseeded and some was obtained using 0.25 micrometers diameter solid seed material. For that test, which will be reported in detail at the Spring 1980 ASME Conference in New Orleans, a diffraction limited collimator lens was used with marked increase in optical efficiency and thus system sensitivity.

7. CONCLUDING REMARKS

An advanced microcomputer automated laser transit anemometer system (LTA) has been designed, constructed, and delivered. This LTA system has been demonstrated to be capable of coaxial backscatter measurements of unseeded flow near walls and surfaces and at velocities up to Mach 1.6. Further tests at speeds up to Mach 5 are planned. The prototype system has been transported to three separate real world tests with high noise and vibration environments and performed well in all cases. The successes support the design choices which include the extensive use of printed circuit electronics inside the compact optical head. The usual complaint concerning data collection time with an LTA system has been substantially overcome by microcomputer automation of the system control and the provision of on-line flow field parameter estimation and graphic operator oriented screen displays. The LTA system is more sensitive than fringe LV systems and is expected to find wide application to measurement problems requiring good sensitivity to the submicron particles which abound in most instances without seeding. A practical LTA system with unique features has been developed and demonstrated.

8. ACKNOWLEDGEMENTS

The development of the optical head electronics described in this paper was funded for the most part by the U.S.A.F. Arnold Engineering Development Center under Contracts F40600-78-C-0002 and F40600-79-C-0003. The Air Force project manager for both contracts was Marshall N. Kingery.

9. REFERENCES

- Schodl, R., "On the Extension of the Range of Applicability of LDA by Means of the Laser-Dual-Focus (L-2-F) Technique," Proceedings of the LDA-Symposium Copenhagen, 1975.
- Smart, A. E., "Data Retrieval in Laser Anemometry by Digital Correlation," Third International Workshop on Laser Velocimetry, Purdue University, LaFayette, Indiana, 11-13 July 1978.
- Smart, A. E., "Laser Anemometry Close to Walls," Dynamic Flow Conference 1978, Baltimore, Maryland, 18-21 September 1978.
- Bartlett, K. G., and Sne, C. Y., "Single-Particle Correlation Techniques for Remote Measurement of Wind Speed: Aerosol Condition and Measurement Rates," JOSA, **69**, 455 (March 1979).
- Mayo, W. T., and Smart, A. E., "Comparison of Data from the Transit Time Velocimeter with Other Systems Now in Use for Velocity Measurements," AEDC-TR-79-32, May 1979 (Final Report on Contract F40600-78-C-0002).
- Mayo, W. T., and Smart, A. E., "Feasibility Study of Transit Photon Correlation Anemometer for Ames Research Center Unitary Wind Tunnel Plan," NASA CR 152238, February 1979, (Final Report on Contract No. NAS2-10072).
- Mayo, W. T., Jr., "Semiclassical Processing of Laser Transit Anemometer Signals," Proceedings of the 3rd International Conference on Photon Correlation Techniques in Fluid Mechanics, Churchill College, Cambridge, U. K., March 1979.
- Final Report on AEDC Contract F40600-79-C-0003 to be published.
- Erdmann, J. C., and Gellert, R. I., "Recurrence Rate Correlation in Scattered Light Intensity," JOSA **68**, p. 787, (June 1978).
- Barnett, D. O., and Giel, T. V., Jr., "Laser Velocimeter Measurements in Moderately Heated Jet Flows," Arnold Engineering Development Center Report No. AEDC-TR-76-156. (April 1977).
- McLaughlin, D. K., and Tiederman, W. G., "Biasing Correction for Individual Realisation Laser Anemometer Measurements in Turbulent Flows," Phys. of Fluids, **16**, p. 2082 (December 1973).

ERRATUM

Following Equation (1), please insert:

Next, the mean delay store number is computed:

$$(2) \quad \text{KBAR} = \sum_R \frac{Y(I)-B}{Q} \cdot I$$

APPENDIX II

SEMICLASSICAL PROCESSING OF
LASER TRANSIT ANEMOMETER SIGNALS

by
W. T. Mayo, Jr.

Presented at:
3rd International Conference On Photon
Correlation Techniques in Fluid Mechanics
Churchill College, Cambridge, United Kingdom
21 to 23 March 1979

Abstract:

Laser transit anemometry (LTA) systems find many practical applications where the statistical variability noise produced by wall flare light limits signal detection. Under these conditions, non-linear threshold-detection and pulse-center-estimation, along with cross correlation processing, is superior to either photon correlation or to classical pulse pair timing. We have developed a photon-limited pulse-center estimation discriminator and demonstrated the efficiency of this with cross correlation processing in recent unseeded backscatter wind tunnel tests with the new SDL LTA system.

This paper introduces ideas concerning cross correlation of non-linearly discriminated LTA signals, some effects of correlator parameters on the measurement of turbulence, and supportive experimental results from steady transonic flow.

INTRODUCTION

Laser Transit Anemometer (LTA) systems are now receiving considerable attention⁽¹⁻¹⁴⁾ because they seem to be more sensitive in the estimation of velocity of very small particles in the presence of flare light than comparable fringe LV systems⁽¹¹⁻¹⁴⁾. Spectron Development Laboratories, Inc. has recently developed a digitally automated LTA system with funding assistance by the U.S. Air Force Arnold Engineering Development Center⁽¹³⁾ and used the system to obtain unseeded backscatter sensitivity and data rate information for the NASA Ames six-foot transonic tunnel⁽¹⁴⁾. Demonstration measurements have also been made in a General Electric research compressor (unpublished). The details of the spectron LTA system are provided in the AEDC report⁽¹³⁾ and will not be repeated here.

The experimental data from the Ames measurements support a few ideas of the author concerning LTA signal processing using a digital correlator. In this paper we will first briefly describe the experiments and then use some of the results as illustrations for discussion of LTA signal processing concepts. The conclusions from this discussion have implications of a dual nature for fringe LV signal processing, some of which may be inferred from an earlier paper⁽¹⁵⁾.

EXPERIMENT

Description of System Used for NASA Ames Experiment

The SDL LTA system illustrated schematically in Figures 1 and 2 was transported to NASA Ames in October 1978, and set up. A 50 ns Malvern correlator (48 store) was used for the high speed delay processing of the SDL pulse discriminator output signals. The correlator was used in both the "photon" and the "pulse" correlation modes and all the indistinguishable states in between as discussed further below. The laser was a Lexel Model 75-.2 operating at about 135 mW at 514.5 nm with 100 mW in the transmitted beams.

The parameters of the SDL optical head were as follows. The spot separation was measured with a calibrated microscope objective as 0.376 mm with $1/e^2$ spot diameters estimated at $1/25$ of the spot separation, i.e., 15×10^{-6} micrometers. The "throw" or range from the front face of the optical head to the probe volume center was 473 mm. The transmitter/receiver lens pair were 40 mm in radius. The outer annular portion of the lens from radius 20 mm to 40 mm radius was used for the receiver, while the inner area from 0 to 20 mm radius was used for the transmitted beams. The transmitter/receiver image rotator prism assembly has digital-to-analog DC drive with DC feedback sensing, and a separate linear potentiometer and analog-to-digital readout. The precision of this angular control system was 0.1 degree.

The co-annular backscattered radiation was imaged around a small transmitter beam turning mirror to two pinhole aperture stops. These transmitted the desired signal radiation and some diffuse background radiation to a microscope objective which magnified the images of the transmitted beams illuminating scatterers onto the ends of two fiber optics assemblies. The purpose of the fiber optics was to separate the light from the two spots to two separate

LTA Optical Components

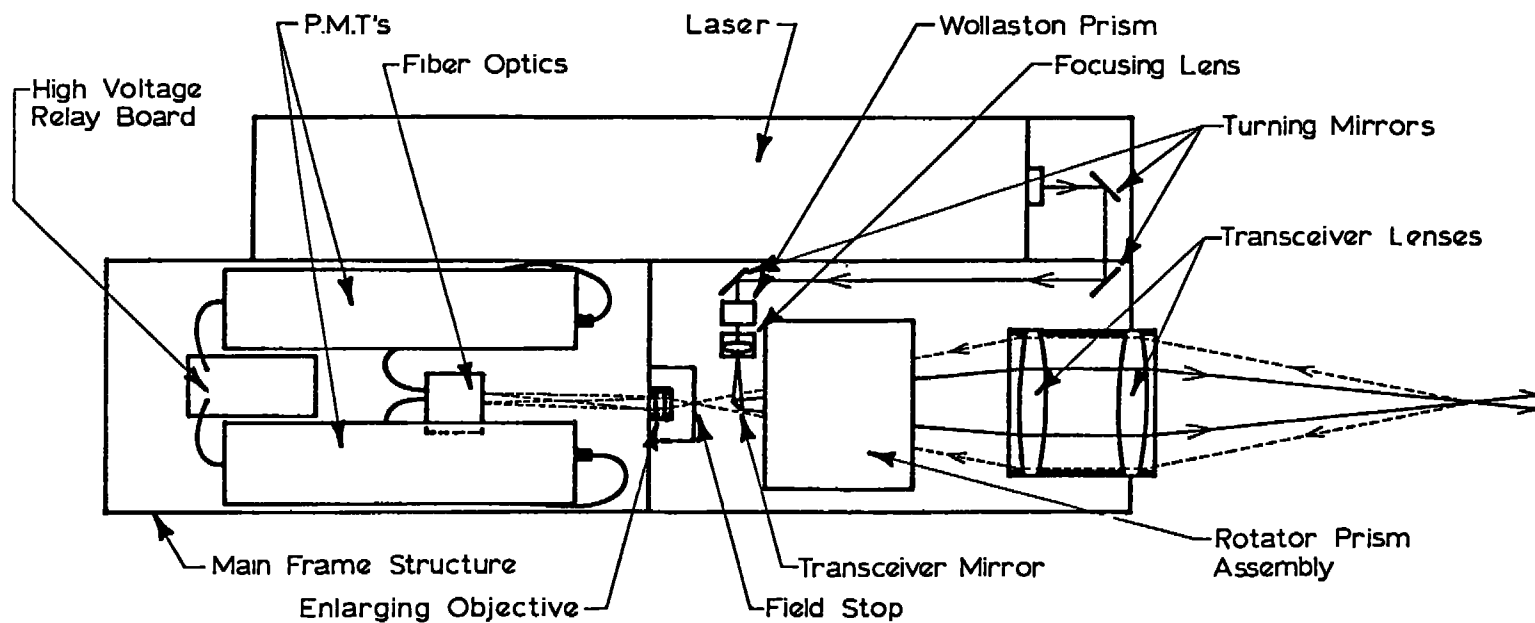


Figure 1. Schematic Diagram of Optical Components in SDL Optical Head.

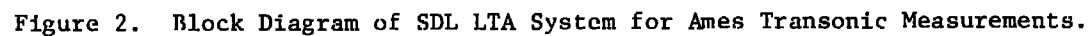


Figure 2. Block Diagram of SDL LTA System for Ames Transonic Measurements.

photomultiplier tubes, one for each spot*. The use of two detectors provided completely unambiguous direction sensing capability and also avoided a zero delay correlation which would interfere with data processing in high turbulence conditions. Perhaps the most subtle advantage of two detectors is that the effective background light is one-half for each detector over what would occur if both spots were imaged on the same tube. Thus, the undesired background for the cross correlation of two detector outputs is one-fourth that of the autocorrelation of one detector output with both signals.

The pulse detection discriminators included several overlapping ranges. Range 1 was optimized for pulses with duration 25-100 nsec; Range 2 for 50-200 nsec; Range 3 for 100-400 nsec, and so forth for seven ranges. Each range included separate optimum detection filters, which were flat in response across the range so as not to bias the detection probabilities towards higher or lower velocities, and pulse center detection filters which determine the center of the pulse independently of signal amplitude.

For signal pulses which contain only one, two, or a small number of single photoelectron pulses, the pulse center detection filter measures a weighted average pulse center estimation. This means that pulse center jitter errors can occur up to the transit time duration as the number of detected photons goes down to one. This implies a distinct precision advantage of working with three or more photoelectron pulses per scatterer transit both to avoid processing so many single photoelectron signals arising purely from background light and to reduce the pulse-center estimation error. In order to use semi-classical and classical pulse techniques, one raises the detection threshold so that single photoelectron pulses are detected less often. However, due to the statistical distribution of single photoelectron pulse heights from the PMT electron multiplier, the transition from single to multiple photoelectron events is not distinct, as the data discussed later shows.

* For these experiments EMI 9816 and EMI D305 tubes were used.
Both tubes are 2" diameter, 14 stage, S-20 tubes of high quality.

The discriminator detection range was both manually and micro-computer selectable from the remote location where the operator was located. The discriminator level and the PMT high-voltage were both manually controllable. The PMT's were protected from maximum anode current overload by high-voltage relays following an anode DC current monitor. These relays were remotely resettable (not shown in figure). The correlator data acquisition and prism rotator were semi-automatically controlled by the microcomputer subsystem.

Measurements in the Six-Foot Transonic Tunnel

The LTA optical head was set up on a table next to a two-inch thick schlieren window. After one tunnel run during which data were collected, the tunnel was down for repairs for several days. When the tunnel was again operational, only limited time was available; but measurements were obtained at several subsonic and supersonic conditions. No seeding was used. The measurements are reported in detail in the NASA report⁽¹⁴⁾. We will only use examples below in our discussion of several points concerning LTA processing. The correlograms presented below were obtained by recording them with the LTA data management system microcomputer and then transferring them to an HP System 1000 computer for additional processing and plotting.

CONCEPTS CONCERNING SINGLE-PARTICLE LTA SIGNAL PROCESSING

Detection Filters

The following ideas are not necessarily original, but have been overlooked by or disagreed with by some investigators. First, single-particle LTA signals are often sparsely distributed as short pulses in time while the background flare light is somewhat more steady statistically. This implies that the optimum detection and velocity estimation system should ideally shut itself off in between particle scattering events and avoid processing single photon events which arise out of background light since they contribute statistical variability without contributing velocity information. This notion was one of the reasons for the development of burst-counter processors for classical fringe LV signals, and it is also applicable to "ideal" photon correlation of either fringe LV or LTA signals. We have briefly discussed this concept for photon correlation of fringe LV signals before⁽¹⁵⁾. An implication which follows immediately is that one must statistically detect the presence of a particle while delaying the signal waveform so that the velocity estimator can be noncausally gated on at time with high probability of the presence of a particle. This implies the use of a digital or analog detection filter in addition to the velocity estimation processing. Thus, we postulate that pure photon correlation using all available photons is not optimum in many applications.

The principle of gating of localized sections of a single-photon impulse signal could be implemented in principle by a shift register delay line with a digital filter which looked for high local number of photon events. A more realizable system uses a classical linear analog low-pass filter followed by threshold detection. The disadvantage of such an approach is that the random variability of the single photoelectron pulse height response of most photomultiplier tubes makes it impossible to cleanly discriminate multiphoton events from

single-photon background unless the threshold is set up very high. The use of cross correlation is helpful in this regard, since it allows us to work in the signal regime of a few photons per pulse even though significant numbers of large single photon background pulses are still detected.

It is important that the detection filters have two characteristics. They must have a smooth Gaussian-like non-ringing impulse response, and they must have adequate bandwidth so that the higher speed particles are not discriminated against by the high-frequency roll off. The bandwidth requirement is not consistent with the requirement of a pulse center estimation filter which must integrate the total signal for an optimum estimate as discussed later.

Figure 3, 4, and 5 illustrate, by computer simulation, what a semi-Gaussian detection filter does to semiclassical signals from a photomultiplier tube. The simulation was for 0.5 micrometer diameter particles at 400 meters per second as described in detail in (13). Figure 3 assumes reasonable efficiency for the optics (0.3) while Figure 4 and 5 include an additional optical efficiency factor of 0.15 to account for difficulties we were having with fiber optics insertion loss. In Figure 4 the four scattering particles occur at the same time as in Figure 3, but the occurrence times are obscured by the background single photon events. Figure 5 shows the filtered version of Figure 4 and we see that all four of the single particle signals would have been detected and none of the single photon background if the detection threshold were placed just so. In practice some desirable signals must be lost if the threshold is high enough to miss most of the background single photon pulses.

Figures 6 and 7 illustrate the detection effects which we have been discussing. These figures are reproductions of the raw cross correlograms obtained in a series of sequential five-second data collection experiments with the six-foot tunnel steady and "on condition" at Mach 0.9. The experiment variable was the detection threshold voltage of the discriminators. The two PMT

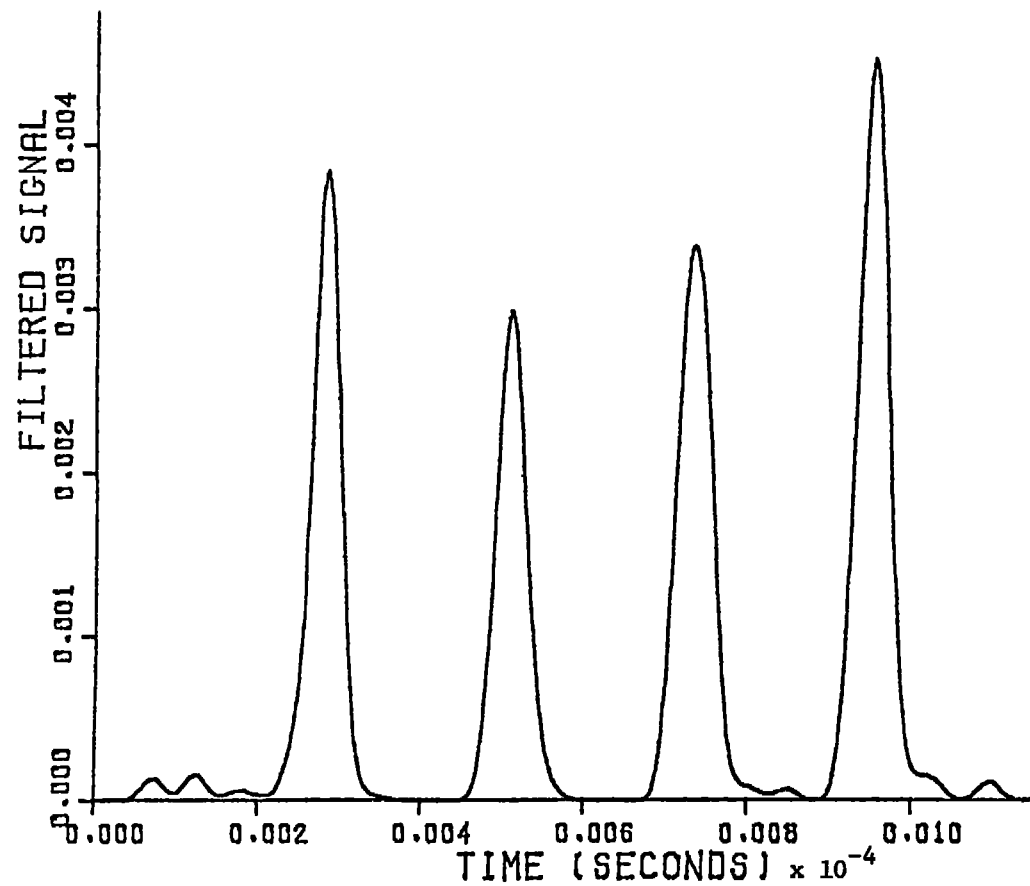


Figure 3. Low-Pass Filtered Signals from Four Equally-Timed 0.5 μm Scatterers.

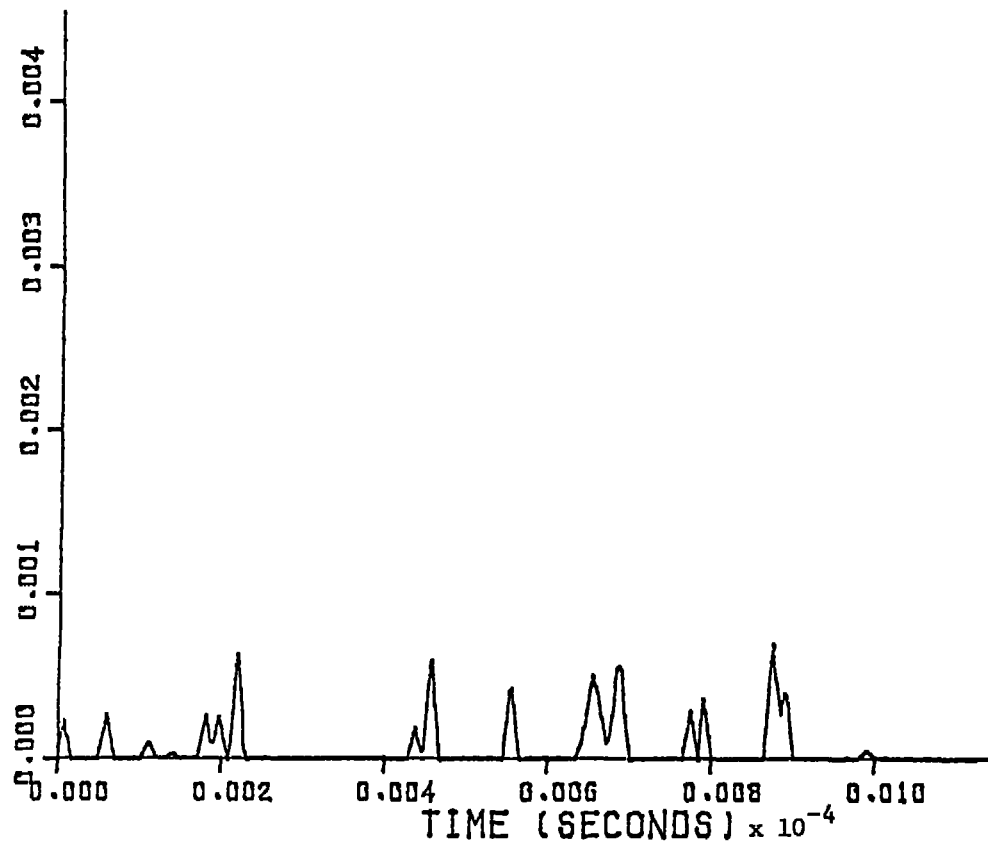


Figure 4. Simulated Signals, 0.5×10^{-6} m Particles,
Optical Efficiency 0.3×0.15 .

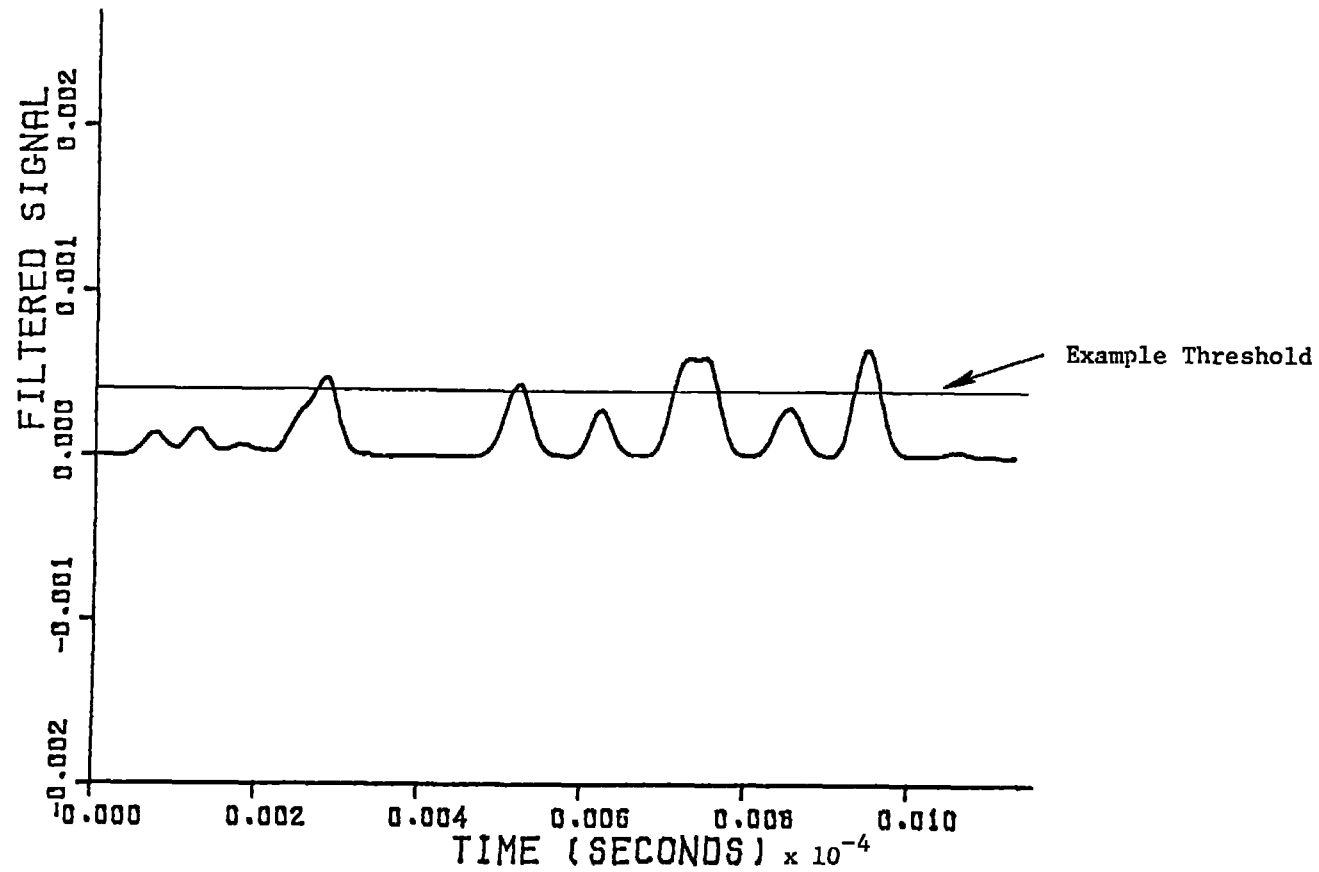


Figure 5. Low-Pass Filtered Signals
from Figure 4.

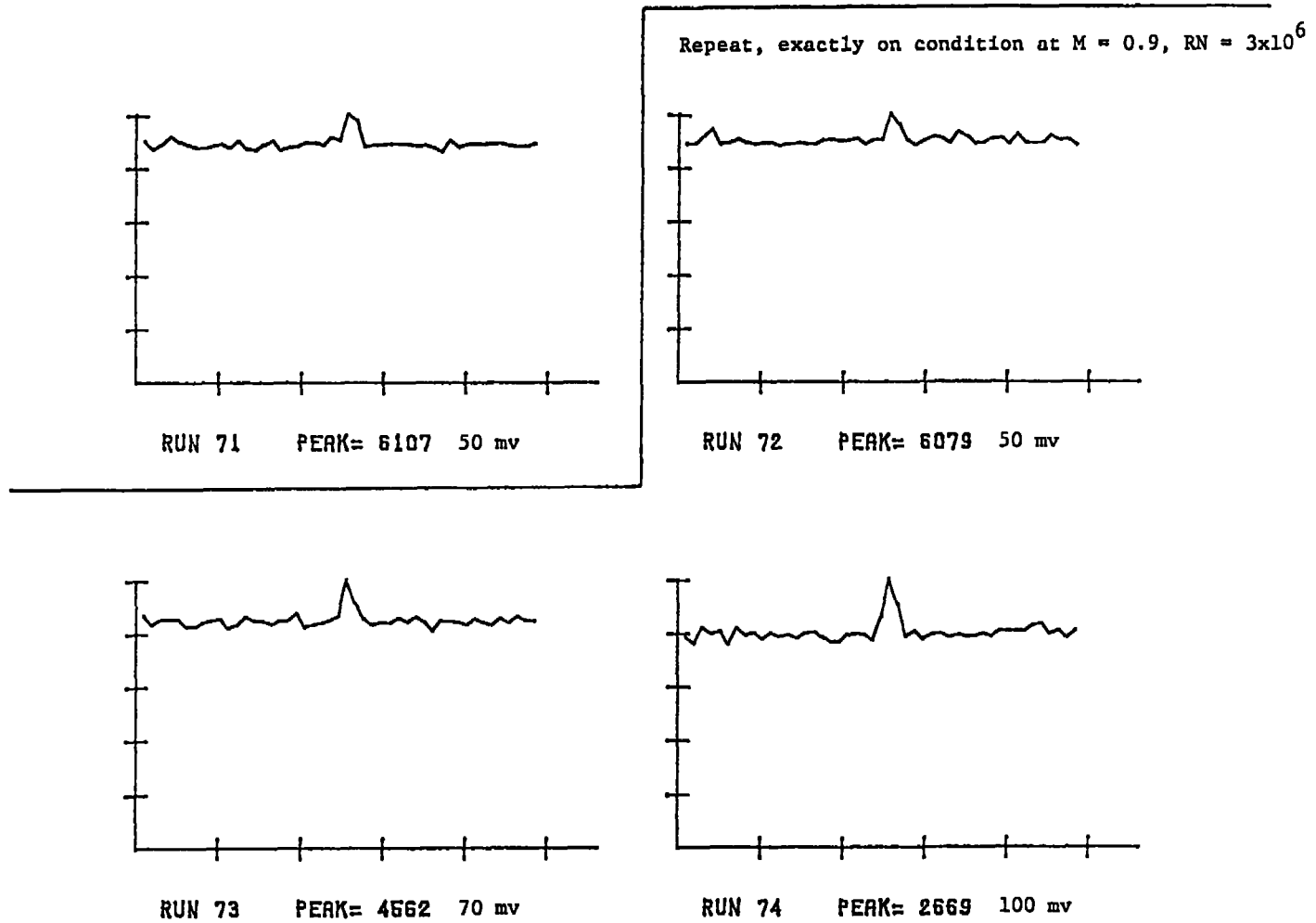
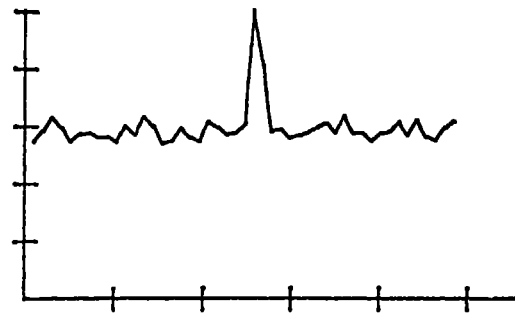
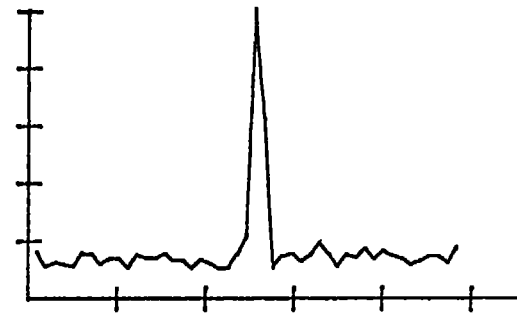


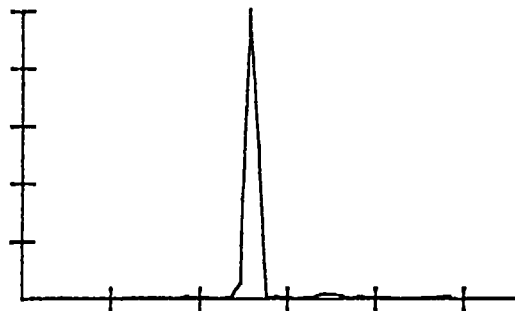
Figure 6. Raw Correlograms from Mach 0.9 Threshold Variation Series.



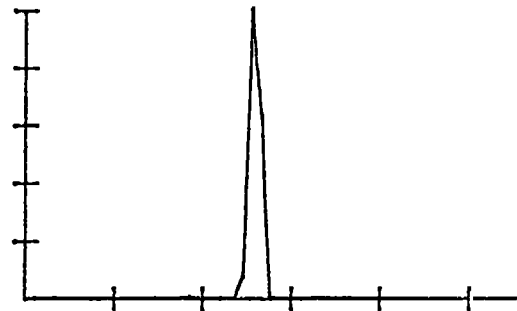
RUN 76 PEAK= 1076 140 mv



RUN 76 PEAK= 364 200 mv



RUN 77 PEAK= 238 280 mv



RUN 78 PEAK= 163 400 mv

Figure 7. Additional Raw Correlograms from Mach 0.9 Threshold Variation Series.

voltages were "balanced" to give similar pulse rates from the two tubes. The displays are normalized, but the value of the store contents with the peak value is printed for each case. The results show very clearly that the variability error of the "signal part" of the correlograms is worse at the 50 mv threshold level than at the 400 mv level.

We have computed the "data pair rate" as the area under the peak after subtraction of the mean background level for the series of runs illustrated in Figures 6 and 7. These results are shown in Figure 8. The data pair rate is much higher with the lower threshold, but the variability error level is seen to be proportionally better with respect to the "signal" portion with a 200 mv threshold than with a 50 mv threshold. On the other hand, there doesn't seem to be much return in going to even higher thresholds where the smaller particle signals are lost.

We observe that for run 76, the input mean pulse rates from the discriminators were about $15,000 \text{ s}^{-1}$ while in run 72 it was $150,000 \text{ s}^{-1}$. The data pair rate was only 100 and 240 respectively for these two threshold settings. We also observe that the spot transit time was $\approx 50 \text{ ns}$. Thus, run 72 reflects approximately the same behavior as would be obtained with a faster, "photon" discriminator since the Malvern correlator can only recognize one event per 50 ns.

Pulse Center Estimation

There is a well-known electronic technique for finding the center (with known delay) of a smooth pulse of known width. The pulse is delayed and subtracted from the underlaid waveform as illustrated in Figure 9. The zero crossing location is thus a measure of the time of the center of the pulse which is insensitive to the pulse amplitude.

It is easy to see from Figure 4 that this technique would not work for photon-limited signals where the single particle signals are "jagged". This occurs for the slower particles on a given range if the detection filter is wideband. If however, the signal is additionally low-pass filtered with a Gaussian-like filter impulse

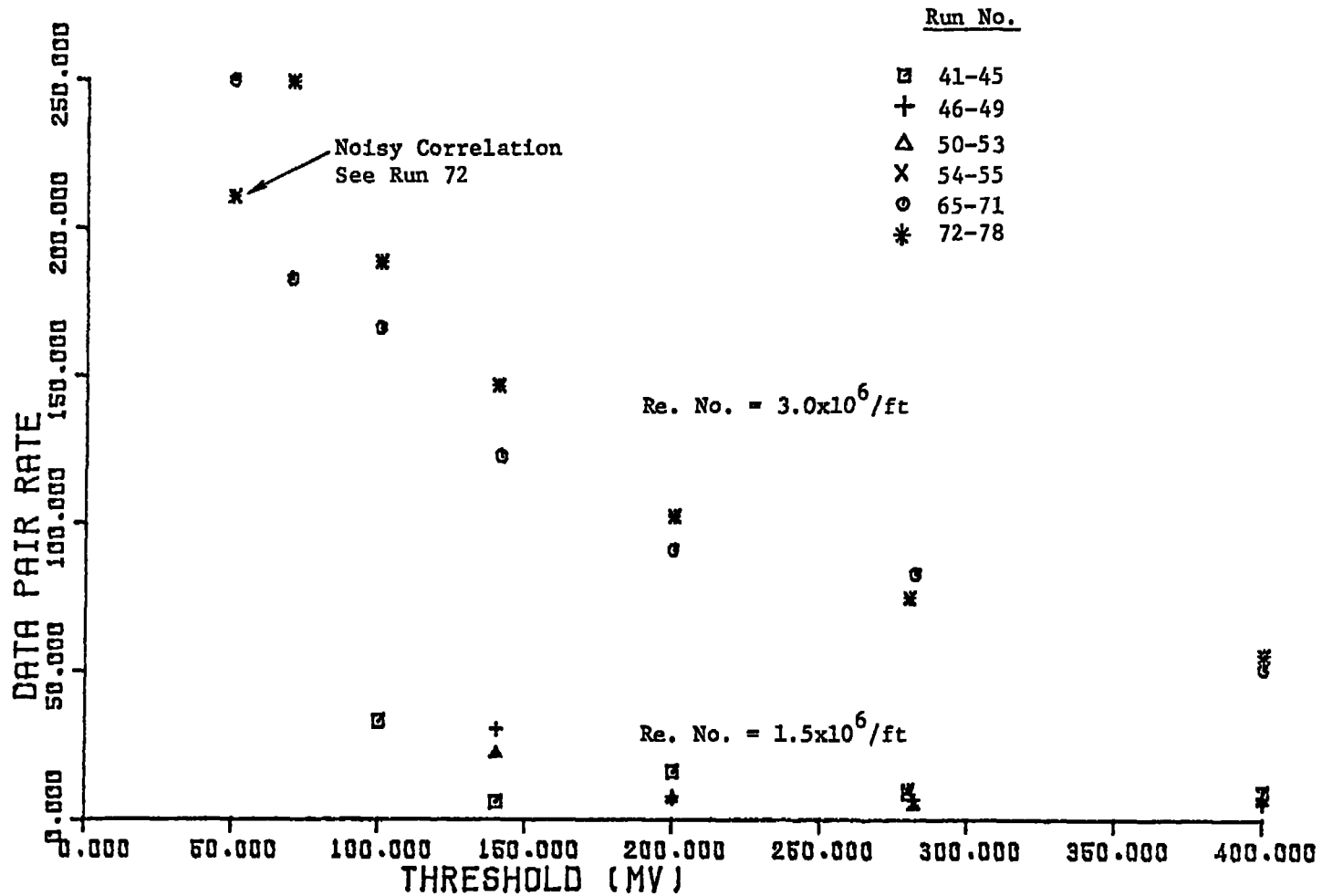


Figure 8. Data Pair Rate Versus Threshold for Mach 0.9 Runs, October 17, 1978.

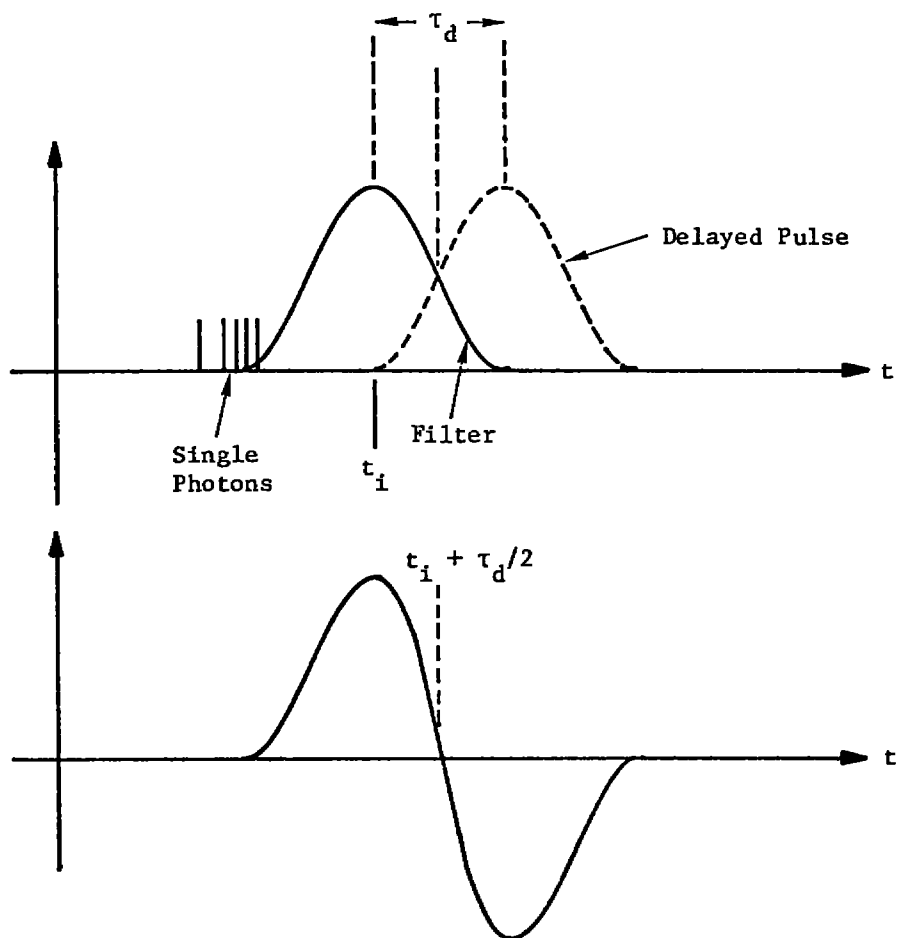


Figure 9. Pulse Center Estimation Concepts.

response which is as long or longer than the classical signals being detected, then the filter output response is always smooth and Gaussian-like in shape regardless of the number of photons in the signal pulse. Furthermore, the duration of the filtered pulse becomes nearly constant and equal to the filter impulse response, so the selection of the optimum delay becomes independent of the particle velocity over a usefully large dynamic range. We have incorporated these concepts into separate pulse center estimation filters which are only conditionally allowed to produce a discriminator output pulse after being "armed" by the detection circuits.

The pulse center estimator just described determines a crude estimate of the center of mass of the single-particle signal. For small photon numbers there will be a random pulse center jitter effect due to the single-photoelectron pulse height variation of the photomultiplier tube. Thus, the use of photomultipliers with good single-photoelectron resolution will improve the timing accuracy of the small semiclassical signals.

When the threshold is high enough for several photoelectrons to be involved in the pulse center estimation, the jitter or timing uncertainty introduced by the nonhomogeneous Poisson statistics of the photon events quickly becomes only a small fraction of the classical signal duration. Thus, the spot transit time broadening of the correlogram is eliminated from the measured data. This is analogous to the fringe LV burst counter processing effect which avoids the "transit time spectral broadening" of the early LV literature. The result is that by using semiclassical (multiphoton) signal detection, one source of "apparent" turbulence is removed, and single-particle velocity estimates are meaningful. We reiterate that digital filters or gated photon correlation would be better in principle due to the potential elimination of PMT pulse height variation. But practical high speed flows may produce 10-50 ns duration transit times, and digital filters with 1 ns resolution are not available.

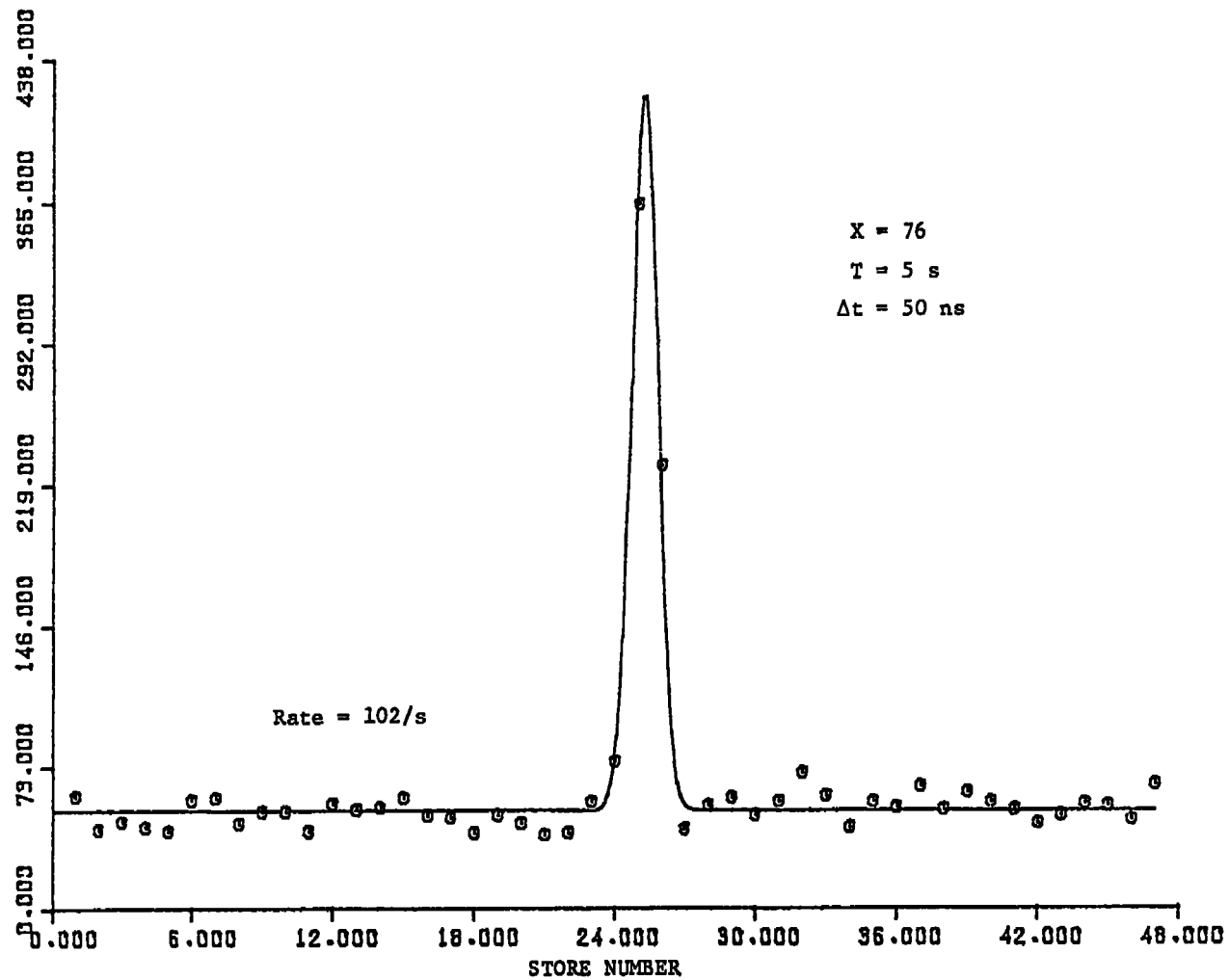


Figure 10. Curve Fit of Correlogram at $M = 0.9$, Threshold = 200 mv.

Extraction of Mean Velocity for Low Turbulence Flows

For idealized perfect estimates of the single particle pulse centers, the contributions to the cross correlation function under the peak become a histogram of particle two-spot transit times. This histogram is similar to a histogram of the N fringe transit times with fringe systems, and many of the related concepts apply directly. In particular, we see that by estimating and subtracting the flat cross correlation background, the histogram of delay times is an estimate of the probability density for inverse velocities along the direction of the two spots. For small velocity deviations evenly distributed about the mean the probability density for velocities has a similar shape to that of transit times according to the approximation for small ϵ of:

$$\frac{1}{1-\epsilon} \approx 1+\epsilon \quad .$$

For small Gaussian turbulence then, it is approximately correct to fit a Gaussian curve to the transit time histogram. We have done this for runs 72 through 78 illustrated above in Figures 6 and 7. Figure 10 shows the resulting fit for run 76.

Examination of Figure 10 shows graphically that a parametric curve fit does not estimate the mean transit time at the peak of the raw correlogram. The figure makes it intuitively obvious that the available precision of the mean velocity estimate is much finer than the correlator clock increment. It is a common mistake to think that this interpolation requires sufficient turbulence in the flow to broaden the peak to include more than one store. This is not true. In Reference 16 we showed that the classical correlation function is convolved with a triangular weighting function whose base width is two delay increments. The effect of this for exactly steady flow with no pulse center jitter is as follows: when the transit delay is exactly an integer number of stores, then only one store will have any non-zero contents. When

the delay is something else, the fractional time that the \pm clock count error occurs distributes the contents in two bins in such a manner that the center of moment is the exact delay value. This concept is illustrated graphically in Figure 11.

As evidence of the precision which we are discussing, we observe that the curve fits for runs 75 through 78 (see Figure 7) gave agreement on the mean velocity estimate of 0.15%.

Extraction of Turbulence Intensity From Low Turbulence Flows

The curvefit illustrated in Figure 10 indicated 2.2% r.m.s. turbulence. In fact, however, we can observe that the width is only slightly greater than the plus and minus clock increment which is automatically present. Thus we conclude that for this set of data, the effects of pulse center estimation jitter and actual turbulence* were both masked by a significantly larger correlator time resolution effect.

It is not unreasonable to consider "deconvolution" of such effects when they are the same width as the effects to be measured or smaller. It is not wise to try to eliminate a broadening effect which is much wider because then small errors become significant in the subtraction with unstable meaningless results. We conclude that for transonic and supersonic flow measurement with the small beam spacing we were using, a 10 ns correlator would be needed to resolve 0.5% turbulence accurately, and a 5 ns resolution would be preferable for supersonic flows.

Data Rate and Background Level Equations

For simplicity assume that all correlated pulse pairs occurred at exactly the same time delay. The rate of occurrence, on either channel, due to these "signal" pulses is then λ_s . The height of the "signal" part of the correlogram above the background level is thus $\lambda_s T$ where the sample duration T is given as

* Which the tunnel personnel estimated at less than 1.0% based on prior experience.

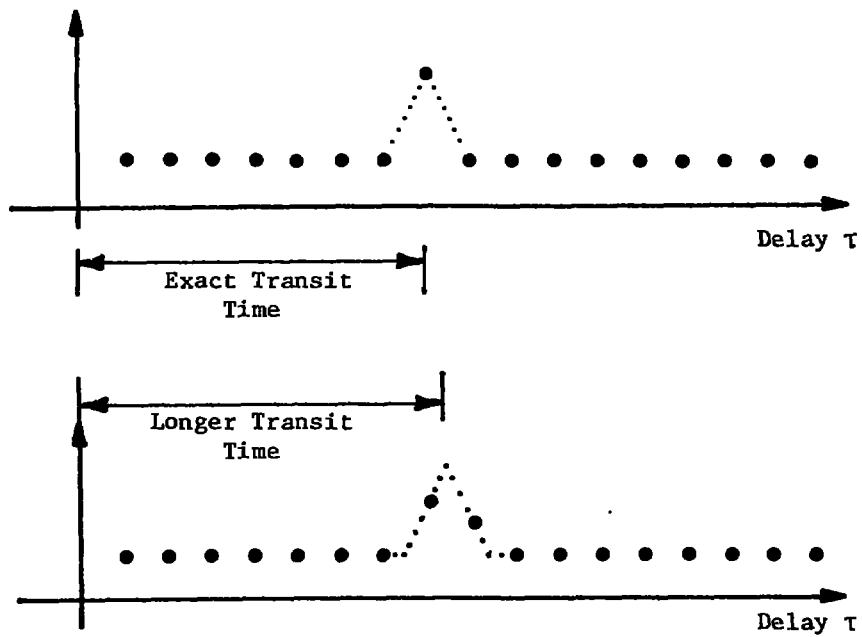


Figure 11. Interpolation of Exact Mean Delay.

$$T = N\Delta t$$

where N is the total number of Δt clock increments. For turbulent flow where the signal delay spreads over more than one delay increment, the height of the signal part of the correlogram is divided by the number of delay increments over which the signal delay is spread.

Now assume that the rates of additional uncorrelated pulses into Channels A and B respectively are λ_a and λ_b . For locations of the cross correlogram other than signal, the correlation function is a flat level with expected value given by $NP(1,1)$ where $P(1,1)$ is the probability of both a 1 in a present sample of Channel A and also a 1 in a delayed sample of Channel B, i.e., for the background locations.

$$P_b(1,1) = (\lambda_a \lambda_s + \lambda_b \lambda_s + \lambda_a \lambda_b) \Delta t^2$$

For cases where $\lambda_s \ll \lambda_a$ or λ_b , as in run 76 for example, $P_b(1,1) \sim \lambda_a \lambda_b$. To demonstrate the numbers practically, we consider run 76 again:

$$\Delta t = 50 \times 10^{-9} \text{ s}$$

$$N = 10^8$$

$$\left. \begin{aligned} \lambda_a &= 15.24 \times 10^3 \text{ s}^{-1} \\ \lambda_b &= 12.76 \times 10^3 \text{ s}^{-1} \end{aligned} \right\} *$$

$$\lambda_s = 102$$

$$\text{Background} \approx (15.24 \times 10^3)(12.7 \times 10^3)(50 \times 10^{-9})2(10)^8 = 48.6.$$

This is to be compared with the run 76 correlator mean value obtained as Background = 50, Background Rate = 50/(5 seconds) = 10 s^{-1} .

In this example the correlogram background level is one tenth the data pair rate and the experiment agrees with theory. We see that

* Actual data measured by the monitor stores of the correlator.

data rate cannot be predicted by measuring the input pulse rates λ_a and λ_b which are much higher. It must actually be measured with a correlator as was done in the experiments. If cross correlation processing is not used, then the form of the mean value of the background is not flat and may present a difficulty in the extraction of data from more turbulent flows. If single start-stop time of flight measurement is used, data is lost when the threshold is lowered enough to produce appreciable background rates. Autocorrelation of signals from a single PMT with both spots imaged on the same tube produces a more difficult correlogram to interpret and considerably more background produces variability.

DISCUSSION: CORRELATORS VS. BURST COUNTERS

There are some similarities between LTA signal processing and fringe LV signal processing. This is not strange since fringe and two-spot optics are simply two different forms of transit time measurement. First we look at two-spot or LTA signals and then consider the analogous concepts for fringe LV signal detection.

LTA Signal Processing

For sparse high-level classical signals a time-to-amplitude converter, or start-stop counter timer, plus a histogram display generator is an excellent data processing technique. The detection of single photoelectron background pulses is avoided and the background level of the display results only when two separate particles each cross a spot within the display delay time. This condition is wasteful of the more abundant and more responsive smaller particles. When the detection threshold is lowered to detect smaller particles, the larger single-photoelectron background pulses are also detected. False starts by a counter timer on background light pulses allows true signal pulses on the start channel to be missed until after counter reset. Digital correlation does not miss this data. Also, for cross correlation, the mean background remains flat so that it may be easily removed by post-detection curvefit processing.

The arguments that some have given to the effect that correlation does not work well is true for pure "photon" correlation or classical correlation of larger signals when large percentages of the signal are classically steady state or slowly varying. Such conclusions are not true when appropriate signal feature detection is used prior to correlation, as we have shown.

Fringe LV Signal Processing

There are direct parallels of the above discussion for fringe LV processing, but they are harder to implement and may not often be

as practical. For large classical signals, a burst counter is a superb detection system. If one could also use a matched tracking filter, classical signals with signal to noise ratio adequate for one percent accuracy could be obtained from 30 photoelectrons in the absence of background light (see Reference 17). Thus the fact that a "burst photon correlator" should be capable of such a feat is not a surprise. It is, however, not easy to obtain the proper tracking filter so in certain situations, a single-burst correlation has an advantage if it is gated off when the signal burst is not present.

We have implied before (see Reference 15) that filtering a fringe LV signal and then correlating the zero crossing times conditioned on a detection filter gate (or arming level for the filtered signal) could be quite sensitive. This is more powerful than even the single-cycle counter histogram approach developed by H. Kalb (Reference 18) because it allows for using the relationship between each zero-crossing and every other one, and thus uses more of the information. The purpose of the filtering and "arming" threshold would be the same as in our LTA experiments, i.e., to avoid the variability added by correlating the background generated "noise" between signals. The sensitivity enhancement reported by H. Kalb (Reference 18) over the conventional burst counter seems to support these ideas.

Implications

When a separate receiver observes low-speed laser anemometer signals with negligible background light, then single-particle photon correlation is an efficient data processing technique. When background light becomes an issue, semiclassical filtering and detection techniques may enhance the system sensitivity over that of conventional photon correlation. For high-speed flows, this filtering will be analog in nature, but single bit digital correlation remains an effective data extraction technique.

CONCLUSIONS

1. Pulse presence detection and selective signal processing can reduce the variability error contributed by background flare light when cross correlation detection is employed.
2. Pulse center estimation based on several photons per particle transit can reduce transit time broadening associated with conventional time average correlograms.
3. Digital cross correlation of semiclassicaly discriminated pulses offers advantages over simpler time-of-flight start-stop processing. It provides a well-behaved (flat) background contribution which simplifies post-detection processing, and data is not missed when more than one "start" occurs before a "stop."
4. Mean flow precision is not limited by the clock interval even for steady flow; but the clock interval does produce an apparent turbulence width which must be considered.
5. These concepts have been demonstrated in the measurement of unseeded subsonic and supersonic flow with a coaxial backscatter LTA system employing a 135 mW laser. The mean flow repeatability obtained was 0.15% at Mach 0.9 from scatterers computed to be 0.5 micrometer in diameter.

ACKNOWLEDGEMENTS

Discussions with and suggestions by A. E. Smart have been numerous and invaluable. Mr. Tom Hunt was responsible for the detailed design and implementation of the electronic discriminators. Ms. Carolyn Greenwood provided simulation software implementation.

REFERENCES

1. Tanner, L. H., Journal of Scientific Instruments, Vol. 4, 1967, pp. 725-730.
2. Thompson, D. H., Journal of Scientific Instruments, Series 2, Vol. 1, 1968, pp. 929-932.
3. Tanner, L. H., Optics and Laser Technology, June 1973, pp. 108-110.
4. Schodl, R., ASME Paper No. 74-GT-157 (1974).
5. Eckardt, D., ASME Paper No. 76-FE-13 (1976).
6. Lading, L., Paper 23, AGARD CP 193, 2-5 May 1976.
7. Bartlett, K. G. and She, C. Y., Applied Optics, Vol. 15, No. 8, August 1976, pp. 1980-1983.
8. Smart, A. E., Proc. Conf. on Photon Correlation Techniques in Fluid Mechanics, Churchill College, Cambridge (England) 6-7 April 1977.
9. Bartlett, K. G. and She, C. Y., Optics Letters, Vol. 1, Nov. 1977, pp. 175-177.
10. Lading, L., Jensen, A. S., Fog, C., Anderson, H., Applied Optics, Vol. 17, No. 10, 15 May 1978, pp. 1486-1488.
11. Smart, A. E., "Data Retrieval in Laser Anemometry by Digital Correlation," Proc. Conf. Third International Workshop on Laser Velocimetry, Purdue University, July 11-13, 1978.
12. Smart, A. E., "Laser Anemometry Close to Walls," Proc. Dynamic Flow Conference 1978, Baltimore, Maryland, Sept. 18-21, 1978.
13. Mayo, W. T., Jr. and Smart, A. E., "Comparison of Data from Transit Time Velocimeter with Other Systems Now in Use for Velocity Measurement," Final Report USAF Contract F40600-78-C-0002, Arnold Engineering Development Center, Tennessee (now in printing).
14. Mayo, W. T., Jr. and Smart, A. E., "Feasibility Study of Transit Photon Correlation Anemometer for Ames Research Center Unitary Wind Tunnel Plan," NASA CR152238, Final Report for Contract NAS2-10072, NASA Ames Research Center, Moffett Field, California (now in printing).
15. Smart, A. E. and Mayo, W. T., Jr., Proc. Conf. on Photon Correlation Techniques in Fluid Mechanics, Stockholm, Sweden, 14-16 June 1978.

16. Mayo, William T., Jr., "Study of Photon Correlation Techniques for Processing of Laser Velocimeter Signals", NASA CR-2780, February 1977.

17. Mayo, William T., Jr., "Ocean Laser Velocimetry Systems: Signal Processing Accuracy by Simulation", presented at the Third International Workshop on Laser Velocimetry, Purdue University, 11-13 July 1978.

18. Kalb, H. T. and Cline, V. A., "New Technique in the Processing and Handling of Laser Velocimeter Burst Data", Rev. Sci. Instru., Vol. 47, pp 708-711.

APPENDIX III

DISCRIMINATOR TESTS

The functioning of the LTA system is dependent upon noise rejection by electronic as well as optical means and the principle of single photon event rejection was discussed in References 20 and 21 of the main text. Under the present contract we have built new discriminators and examined their performance. Several tests were performed and limits of behavior quantified, the results of which are presented here.

MEAN DELAY BIAS TESTS

The first test of systematic electronic delay difference, before the diode test was introduced, was to rotate the spots 180° in a jet flow and compute the velocity A→B and B→A. Any difference shows a systematic disparity in signal processing delay. To our surprise, we found a disparity of 100 ns! This was finally traced to a photomultiplier dynode, miswired on receipt from the manufacturer. This was causing a charge cloud around one accelerating electrode which thus retarded electron transit. The clue which led to the discovery of the cause of the delay effect was reduced gain of one P.M.T. which had required a compensatory increase in high voltage. This was not suspected immediately because there is significant difference in gain from one individual P.M.T. to another.

The photomultiplier/preamplifier/filter/discriminator combinations (Figure 1) were tested by inserting a light pulse from a fast light emitting diode. The input electrical pulse is shown as Figure 2. The final output pulse from the discriminator is shown as Figure 3. The time delay between input pulse and output pulse in a satisfactorily operating system was found to be about 70 ns and is subject to both systematic mean and time dependent deviations. The two channels may not be perfectly matched causing a systematic difference between them. This was observed as no more than a few ns

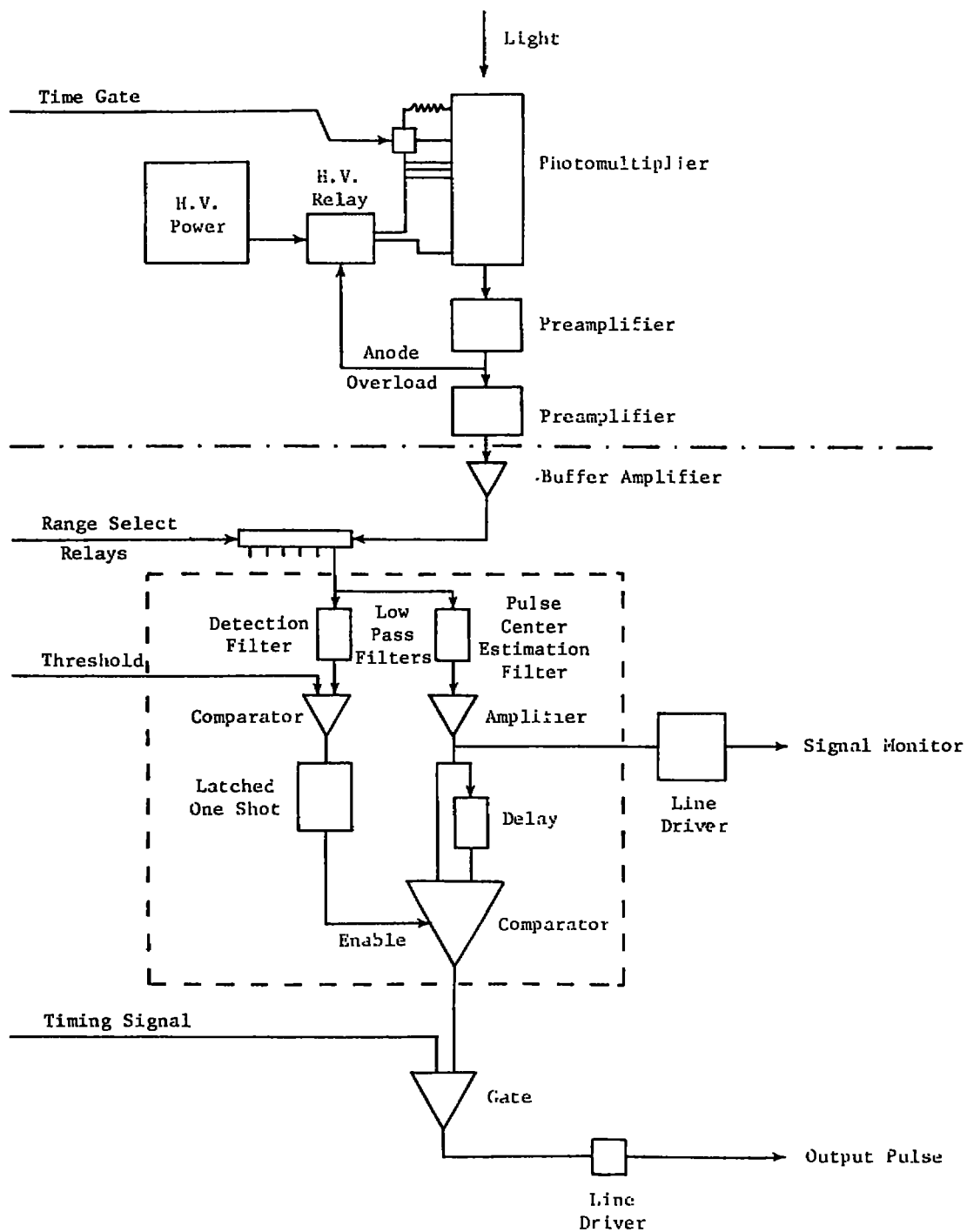


FIGURE 1. SCHEMATIC OF ONE CHANNEL OF ELECTRONICS

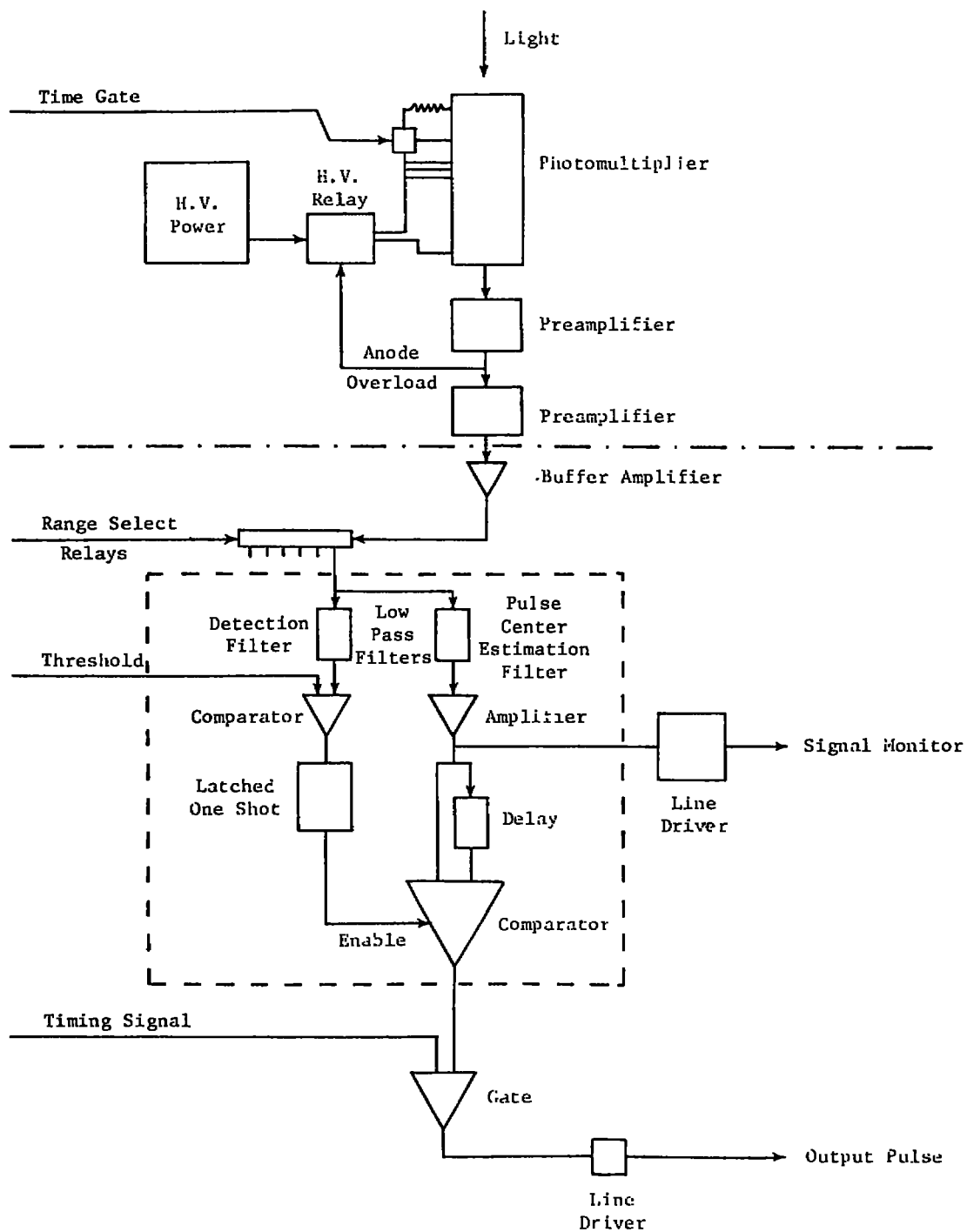


FIGURE 1. SCHEMATIC OF ONE CHANNEL OF ELECTRONICS

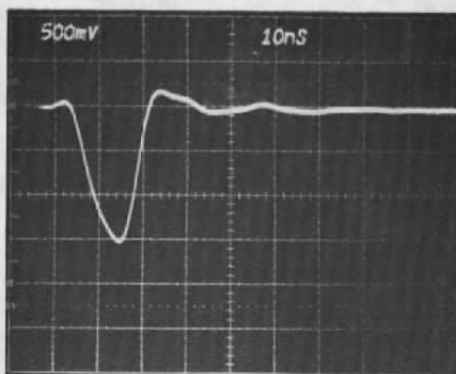


Figure 2. Electrical Signal to Test LED.

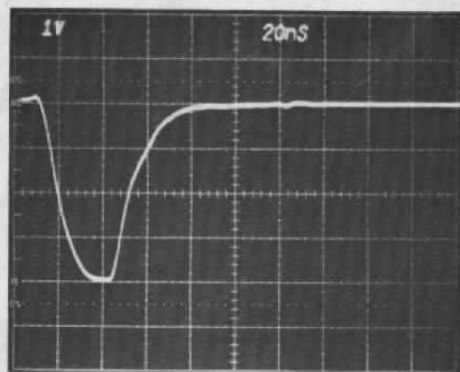


Figure 3. Discriminator Output Pulse.

on most ranges and its significance as a systematic error depends on the time of flight of a particle between spots. On the high speed ranges, 00 and 0 the mean deviation for a fixed amplitude input pulse was on the order of 2 ns.

PULSE FILTER EFFECTS AND REMOVAL

Figure 4 shows the response of the P.M.T. monitor circuit on range 00 for a diode input and attenuation which yields a small number of photons per pulse. There is a significant probability of getting NO photons from some of the pulses. This photograph, as all others in the following sequence is obtained as the superposition of about half a million events. Figure 4 shows that from such a stimulus, it is possible to get output pulses of a wide range of amplitudes. The low trigger level (80 mV) makes it possible to see that there is a preferred height of the most probable pulse from one single photon and a slightly reduced probability of pulses of lesser height. This is, therefore, fairly good tube and corresponds to a demonstration (of single photoelectron pulse heights) of the curve C in Figure 2 of Reference 13. This is shown again by Figure 5 where the signal comprises an average of less than one photon (evinced by the baseline) triggered from the diode exciting pulse. It shows overlying peaks of different heights and a 'hole' where there are not significant numbers of small pulses from real photons. Two photon events occur too infrequently to be a significant contribution to this picture. Figure 6 is a somewhat similar picture to Figure 4 but now has a trigger level set to 600 mV to exclude all pulses which may not have arisen from a 'real' incident photon.

Figures 4 and 6 show that because of single photoelectron pulse height differences, the time of the peak relative to the fixed threshold detection point shows a scatter of about 6 to 8 ns - a quite unacceptable equivalent transit time broadening from nominally identical events. Figure 7 shows how this spread is removed by the pulse center

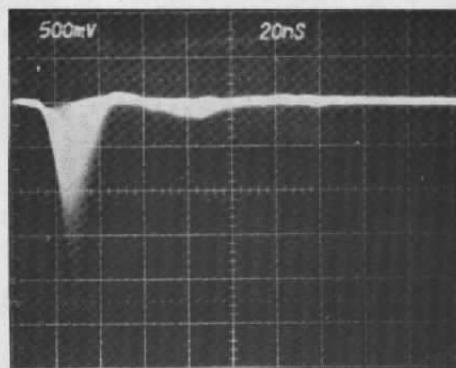


Figure 4. Signal Triggered from a Low Threshold.

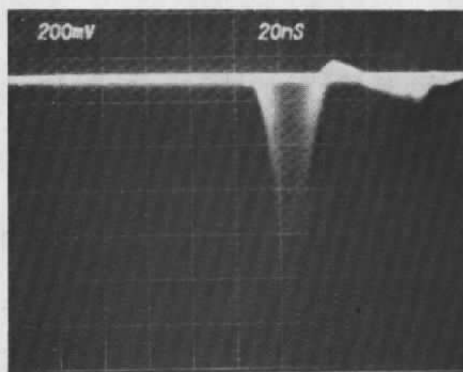


Figure 5. Signal Triggered from Diode Exciting Pulse.

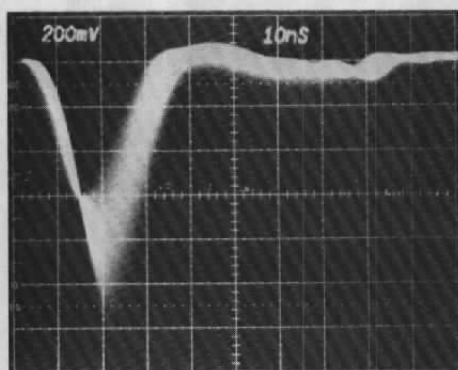


Figure 6. Signal Triggered from a High Threshold.

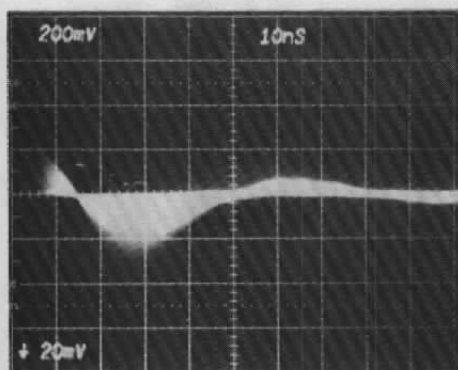


Figure 7. Output Waveform from Pulse Center Estimation Filter.

finding circuit and shows the event triggered from the output pulse. The spread of the peaks of different heights is now seen to be symmetric and involve minimal dependence of timing on pulse height.

PHOTON PROBABILITY JITTER

While the discriminators make good estimates of the time location of a single photon pulse, there are other effects to consider. When only a few single photon pulses occur during the classical signal probability envelope defined by classical scattering theory, then jitter occurs in the pulse center estimate due to the inhomogeneous Poisson occurrence time statistics of the single photoelectron pulses and due to the random single photoelectron pulse height distribution of the P.M.T. The integrating pulse center estimation filters find a weighted transit mean center, which (practically speaking) eliminates the photon probability jitter effect when several single photons contribute to a transit event. However, no analytical theory for the extent of time jitter versus photon number and P.M.T. probability distribution parameters has been developed to our knowledge.

In order to find the extent of photon jitter effect in a typical high-speed measurement, the light emitting diode was used again, but this time the oscilloscope was triggered from a sample of the pulse generator source pulses. The resulting multiple trace oscillograms of the discriminator output pulse leading edges are some measure of the overall jitter due to both the previously discussed amplitude effects and the occurrence probability effects.

Tests were conducted for different ranges with the oscilloscope triggered from the electrical pulse driving the diode. On an expanded time base, the following illustrations were obtained of the starting edge of the discriminator output pulse. To simulate worst case operation, the average number of photons per pulse was set to less than one

as is shown by the presence of a baseline of triggered sweeps with no discriminated event. The change of threshold had almost no effect on jitter over a wide range, for a photon is a photon with either a discriminable event or not, but it may be emitted at any time during the pulse of electrical energy to the diode (with a probability depending upon the waveform and the device).

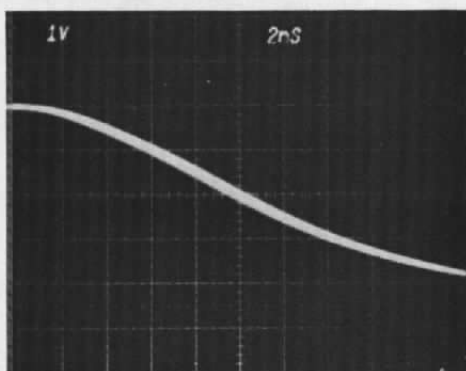
A sequence of jitter properties is shown on Figure 8 (a through e) and the details are summarized on Table I. Each is for about one million events and this sequence is all for range 00, the fastest. All were taken at the same threshold.

TABLE I

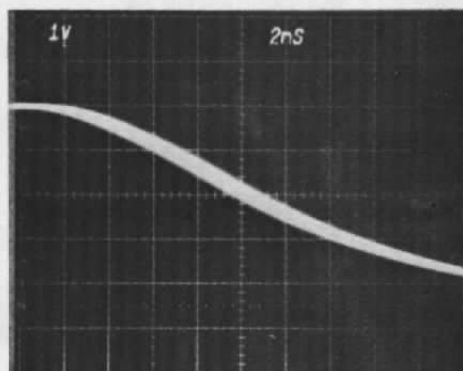
<u>Figure 8</u>	<u>Photon/Pulse</u>	<u>High Voltage</u>
	(Mean)	(Volts)
a	Many	1250
b	Many	1400
c	1 - 2	1400
d	1 - 2	1600
e	< 1	1600

THRESHOLD/RANGE EFFECTS

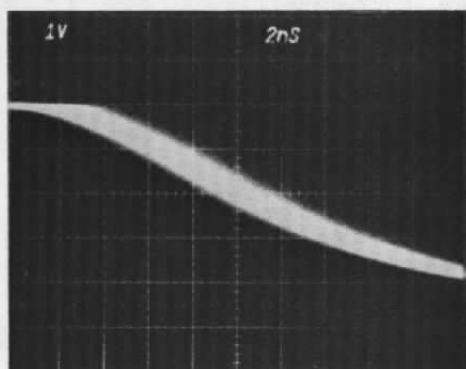
Because there is a link between threshold level and precision of timing, it is possible to check that similar event jitter characteristics occur on each range. Figure 9 (a through d) are pictures of the same type as in the previous section. The scope was triggered from the current exciting the diode and the discriminator pulse was observed at suitable timebase dilation. The ranges increase in factors of two with respect to the input filter except for range 0 which has the same input filter as range 1 with different pulse center estimation filters.



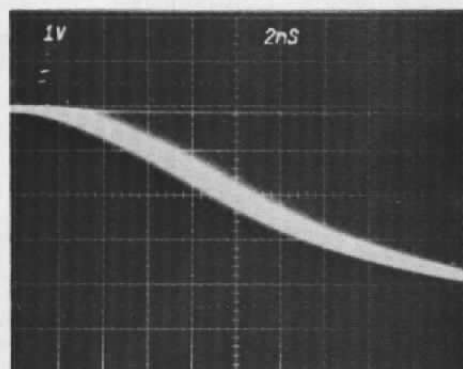
(a)



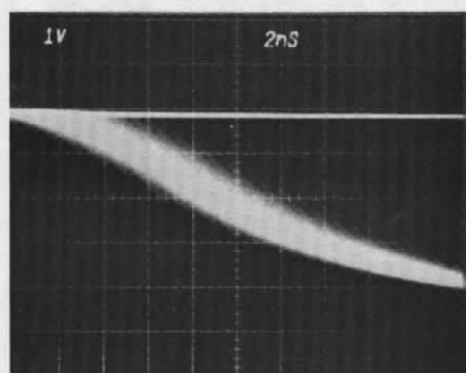
(b)



(c)

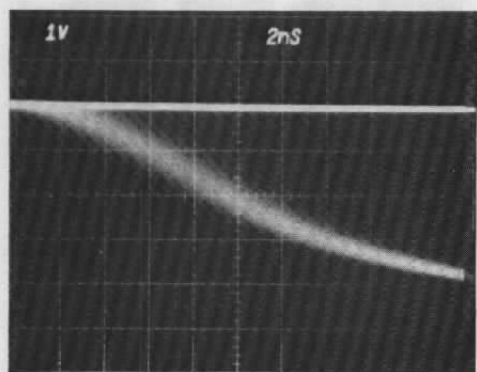


(d)

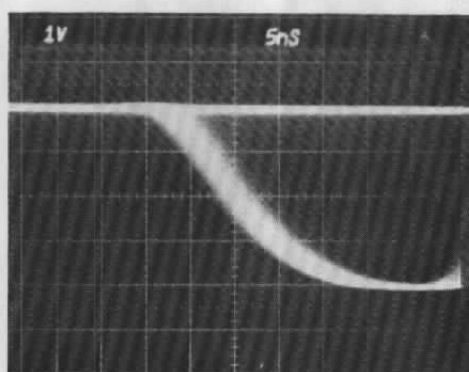


(e)

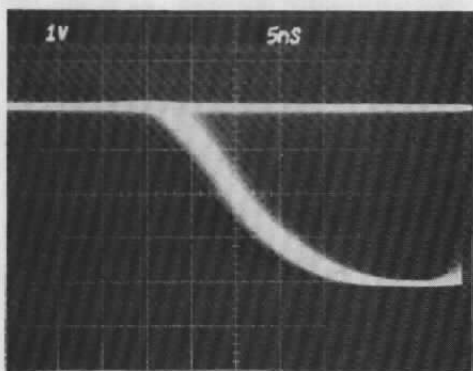
Figure 8. Time Jitter Effects.
(Table I)



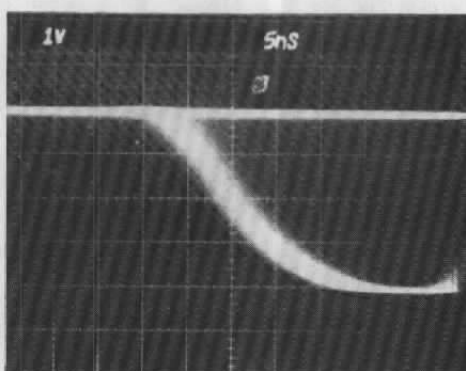
(a)



(b)



(c)



(d)

Figure 9. Threshold Range Effects. (Table II)

The same results would be expected in terms of rate and jitter when changing the threshold by the inverse of the extra dilation incurred by using a lower frequency filter. The Figures are identified in Table II.

TABLE II

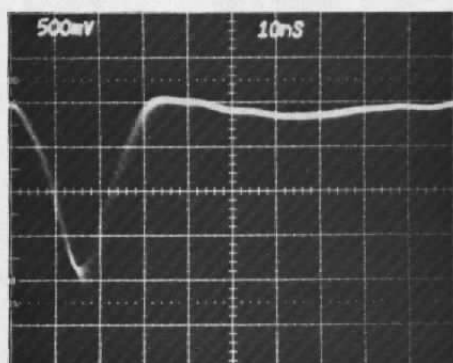
<u>Figure 9</u>	<u>Range</u>	<u>Threshold</u>
a	00	8.0
b	0	4.0
c	1	4.0
d	2	2.0

RANGE FILTERS

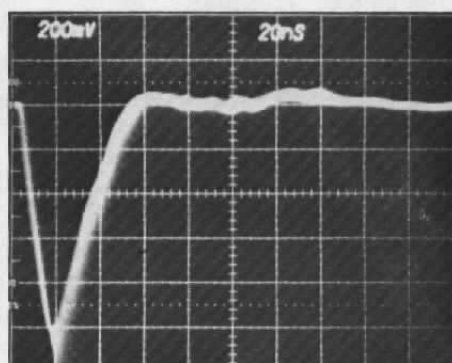
Figure 10 (a to f) are pictures of the response of the ranges 00 through 4 to the same optical input signal. The amplitudes reduce by the same factor as the detection filter and do not proceed perfectly in the ratios 16:8:8:4:2:1 because of variations in trigger level. The tendency is illustrated satisfactorily on the pulse lengths. There is a small amount of overshoot and some effects of small residual line mismatch when observed from the monitor terminal but this does not affect the machine performance. More seriously, there is a glitch some 6 squares after the peak due to the cross channel interference of the discriminator output pulse on the other channel. This cross talk has not yet caused problems but it may ultimately be necessary to eliminate it.

The plug-in discriminator cards have properties described by Table III which relates also to the figures.

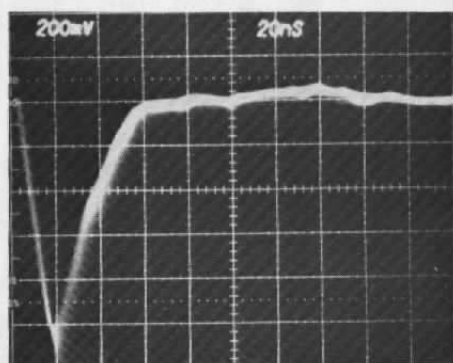
Figure 11 shows the discriminator with continuous light and too low a threshold setting. There is an undesirable bounce feature



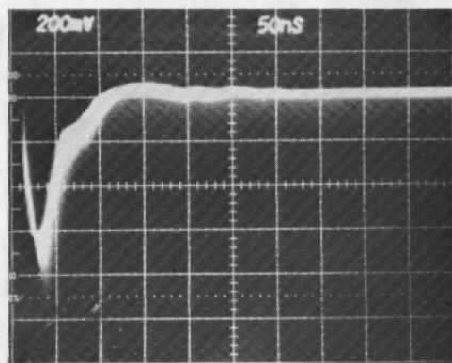
(a)



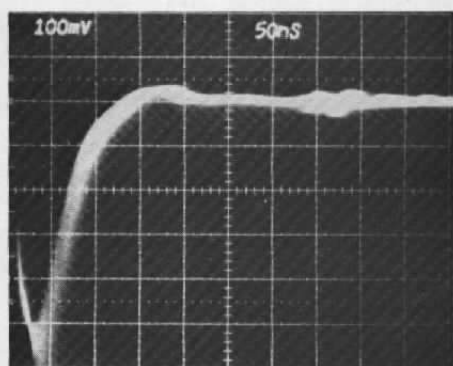
(b)



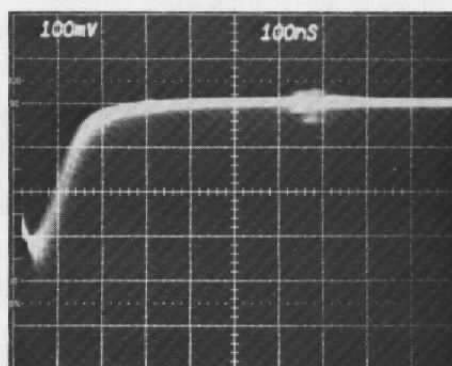
(c)



(d)



(e)



(f)

Figure 10. Signal Monitor on Each Range. (Table III)

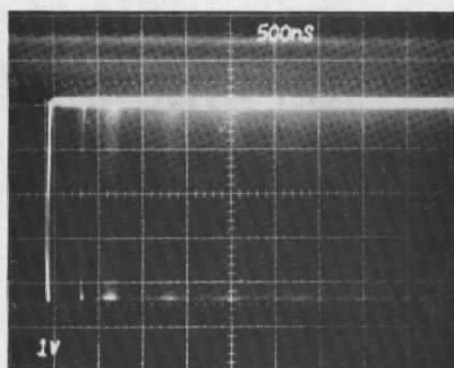


Figure 11. Discriminator Output Pulse (With Bounce).

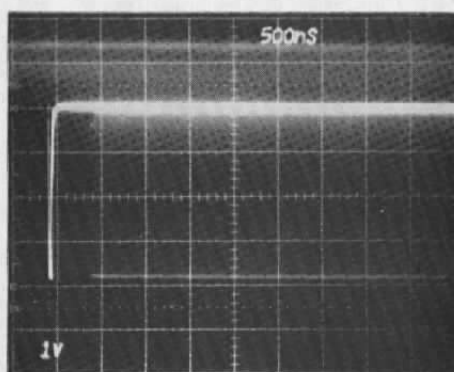


Figure 12. Discriminator Output Pulse (Corrected).

where several pulses are produced related to the initial firing. This is highly unsatisfactory for work where the output pulses are correlated and was cured by a small change in the reset line timing to produce the cleaner picture of Figure 12. This change resulted in a slight increase in discriminator dead time which is not so serious a penalty as multiple firing. Range 3, from which these photographs were obtained shows a dead time of 450 ns whereas the faster ranges show proportionally shorter dead times.

TABLE III

DISCRIMINATOR CARD PLUG-INS

<u>Figure 10</u>	<u>Range</u>	<u>Detection Filter</u>	<u>Pulse Center Estimation Filter</u>	<u>Card Slot</u>
a	00	< 20 ns	25 ns	1
b	0	25 ns	50 ns	2
c	1	25 ns	100 ns	3
d	2	50 ns	200 ns	4
e	3	100 ns	400 ns	5
f	4	200 ns	800 ns	6

APPENDIX IV

SECTION 7.0 THROUGH 7.3 OF
"LASER TRANSIT ANEMOMETER SYSTEM OPERATION MANUAL"

SDL Report No. 79-6463

July 1979

7.0 OPTICAL CLEANING AND ALIGNMENT

There is one important consideration to be observed when embarking upon the task of alignment or cleaning of optics:

DON'T

7.1 Getting Dirty

There are several items which may get dirty after prolonged or careless use.

- 7.1.1 Slow and overall deposition of dust on all surfaces including optical components may occur. This deposit may be removable with a blast of clean air. If it becomes very bad, as it may if the unit is frequently opened in dirty places, it is necessary to disassemble the machine, clean the components and reassemble and align the unit. This is not a recommended action for the user -- we do, however, include sufficient information for you to do this.
- 7.1.2 Thermophoretic transport in the close neighborhood of surfaces and dust deposition on the output train optical components may impair the performance. The components most likely to suffer from this are the four turning mirrors, the transceiver mirror, and the focusing lens. The Wollaston prism is quite well protected by the alignment stop and in any case would require disassembly for cleaning, although its reassembly and alignment is fairly easy. The lower surface of the

focusing lens is prone to thermophoretic deposition but cleaning should only be necessary after exposure of the naked system to a dusty environment (see Section 7.2).

- 7.1.3 The front surface of the final outer transceiver lens may get dirty more readily than any other component simply because it is exposed to the ambient conditions more often and for longer periods. Depending upon the type of contamination it may be cleaned by blowing with clean dry air and/or cleaning with solvent as in later sections.

7.2 Cleaning Optical Components

In general if only one component at a time is removed for cleaning it is not necessary to realign the entire system. It is however essential to replace each cleaned component in precisely the same place and orientation. It is important to follow these instructions to avoid unnecessary re-alignment tedium. If a screw has red sealant on it you are advised not to touch it. Most can be recovered with sufficient patience but those adjustments on the rotator prism require great dedication. Just in case you are tempted to alter the system, we do give full alignment details in Section 7.5, but touch the red screws at your own risk.

Any carelessness or failure to observe the precise instructions in this section of course invalidates the guarantee. Prior to cleaning or optical maintenance of any kind set the optical head in a clean, warm, dry environment.

For the actual cleaning wear medical quality cap and mask and use thin polythene gloves or be sufficiently practiced never to touch a component on or near an active surface.

The outer part of the unit should be cleaned free from dust or dirt prior to the removal of the side panels. Many components may be adequately cleaned in situ. For those which must be removed observe the instructions and do not become involved with more than one component at a time.

- 7.2.1 A component should be initially blown free of deposited dust or potentially abrasive particles with a jet of clean dry air or nitrogen. Mostly the sticky particles are not abrasive and the abrasive particles are not sticky but this is not guaranteed and it should not be assumed that all grit has been or can be blown off.
- 7.2.2 Obtain the purest methanol (methyl alcohol, CH_3OH) available and charge a hypodermic syringe with it. Rinse the syringe many times to remove the soluble fraction of the seal lubricant. It is usual to favor an eye-dropper for supplying the alcohol but since in this system most of the components to be cleaned are not horizontal the syringe is more appropriate. Since it is useful to retain the hypodermic needle to permit easy control of alcohol flow great care must be exercised to avoid touching the needle point on the surface when supplying alcohol to the component to be cleaned.

Use good quality optical tissue -- facial grade Kleenex is okay provided you always use a new pack or discard those pieces which have been exposed to dust collection. Break the top off the box so that a fresh tissue is accessible without exposing the one beneath to a situation where it no longer protects

the one beneath it. Keep the box covered at all times.

Lay the tissue near the surface and supply sufficient alcohol to attach the tissue by capillary attraction at one edge. Slowly and deliberately drag the tissue across the surface such that no visible liquid residue is left. This procedure may be repeated several times. Although all the surfaces in this machine have protected overcoating it is still highly undesirable to 'scrub' the surface. Under certain types of greasy contamination the solvent may be replaced by chloroform (CHCl_3) or even methylene chloride (CH_2Cl_2) but these are more volatile and pick up contamination more easily requiring greater care in use.

- 7.2.3 If a component cannot be cleaned adequately or becomes visibly scratched the damage must be considered in the light of its function in the system. Some components are relatively tolerant of certain types of damage; others must be replaced. It is usually possible to make this decision by careful observation and detailed thought. If you are unsure seek professional advice.

7.3 Cleaning Specific Components

Proceeding through the system in the same way as the light we observe a sequence of components which have different properties and requirements. (Refer to Figure 1.1.1-A)

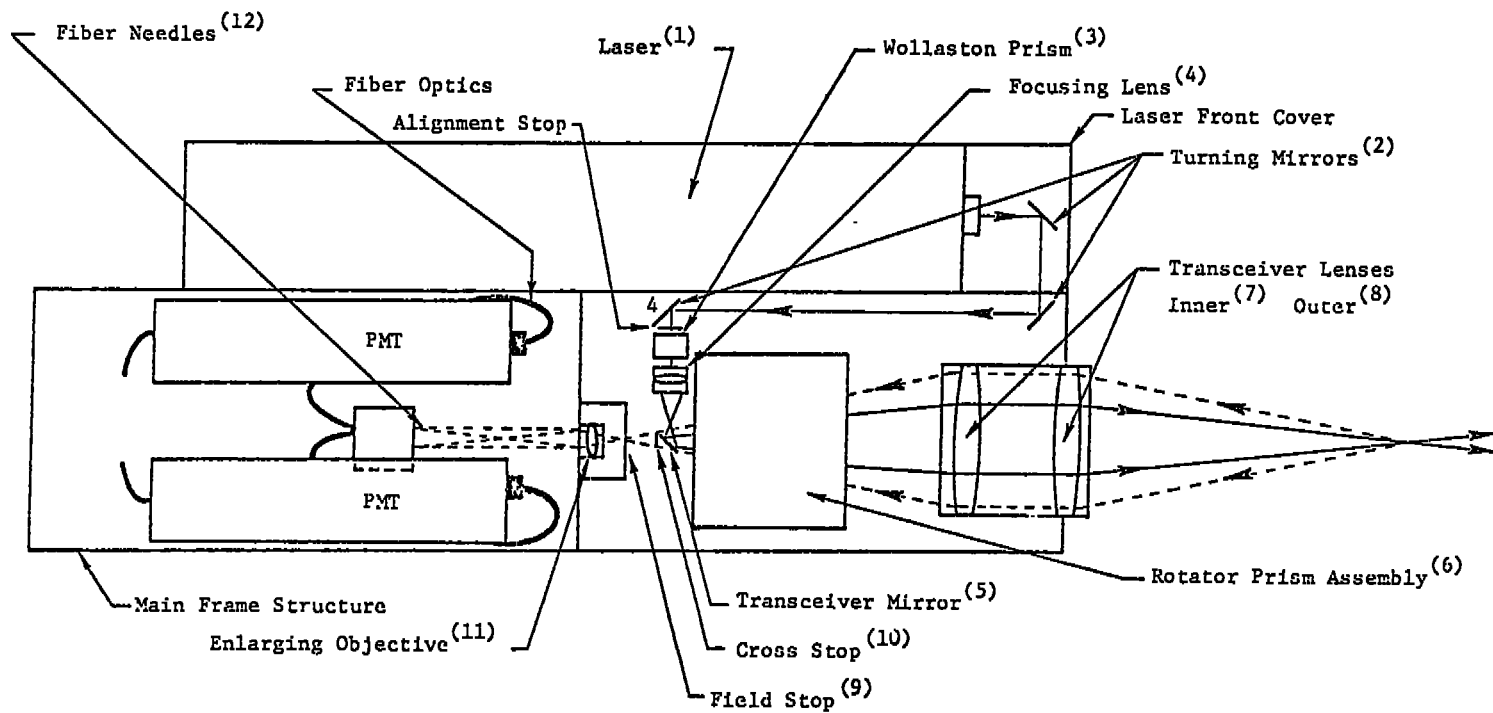


FIGURE 1.1.1-A MAIN COMPONENTS OF OPTICAL HEAD

7.3.1 Laser Output Window

It is unlikely that this component will become dirty. It is both far recessed and protected within the laser top cover enclosure. If this component causes bad beam profile or reduced intensity, remove and clean according to the manufacturer's instructions. (See the Laser Handbook.)

7.3.2 Four Turning Mirrors

Clean only when necessary using method of 7.2.1 and 7.2.2. Do not remove any fixing screws. Clean one mirror at a time and realign before moving on to the next one. For realignment, use the method outlined in 4.1.13 and 4.1.14.

7.3.3 Wollaston Prism

This is well protected and should not require cleaning. If it does, remove the mounting block: this is irrevocable and should not be considered casually. Remove the alignment stop, and slide the prism out noting its approximate orientation. If you damage either surface in disassembly or cleaning, replace the component. Realignment will be necessary after the cleaning operation.

If the entire system is being cleaned, replace the Wollaston prism but not the alignment stop at this stage. (See Section 7.4 on system alignment.)

7.3.4 Focusing Lens

The most likely contamination of this lens will be on the lower surface which is easily cleaned by method 7.2.2 without removal. If the upper surface is dirty, then it must be cleaned after removal. It is possible with sufficient care to mark the depth and orientation of this lens and to replace it without need for realignment but this is not especially easy. With some care, it is possible to make very small adjustment to this lens both in depth into the mount and rotation of the lens. The rotation does not always have any significant effect: it depends on the axial perfection of the specific focusing lens and they vary a little from unit to unit.

7.3.5 Transceiver Mirror

This is a small right angled prism whose hypotenuse is the only active surface. It is coated with silver and protected, but is still fragile. We do not recommend changing the adjustment of this component. It may be cleaned in situ by the method of 7.2.1 and 7.2.2. In the event of damage it must be replaced and readjusted (See Section 7.4).

7.3.6 Rotator Prism

This component may be cleaned in situ only with great care and some difficulty. If it is removed for cleaning (7.2.1 and 7.2.2), see realignment sequences (7.4).

If the prism as a subunit is damaged or itself misaligned, see Section 7.5.

7.3.7 Inner Transceiver Lens

This lens may be removed for cleaning (7.2.1 and 7.2.2) as necessary, but must be replaced in the same position, depth of insertion into the holder and square to the beam. It must, of course, be refitted the same way round! It is wise to check that the output light with the outer transceiver lens removed is perfectly collimated.

7.3.8 Outer Transceiver Lens

This lens has no critical positioning. Removal incurs no problems except the need to recalibrate the throw and spot spacing. It is quite possible with care to replace it so exactly that even this is not essential.

7.3.9 Field Stop

It is unlikely that the field stop will become clogged with debris unless the rest of the instrument is virtually destroyed. Any cleaning should be performed as in Section 7.2.1.

7.3.10 Cross Stop

It is not necessary to do anything to maintain this component unless it has acquired bits of fluff or wool (or pieces of flesh if you have caught your hand on it, in which case, it is probably bent and will need flattening and repositioning). In a complete cleaning and re-alignment procedure it may need slight adjustment.

7.3.11 Enlarging Objective

This should never need cleaning or touching in any way except under the complete realignment procedure (Section 7.4).

7.3.12 Fiber Needles

These may be very carefully swabbed with alcohol (7.2.2) if essential.

No other items should require cleaning to improve the functioning of the instrument nor to restore it to its former operating specification.

APPENDIX V

SECTION 7.4 OF
"LASER TRANSIT ANEMOMETER SYSTEM OPERATION MANUAL"

SDL Report No. 79-6463

July 1979

7.4 Alignment of System

The optical system should never need complete realignment unless terrible things have happened to the instrument, i.e., extreme heating (from rig malfunction!) to the point of warpage or violent physical shock to the point of case distortion. If components are exchanged in groups or singly it may be felt that the alignments will improve the system, and this section includes sequence and details of such an alignment. There are partial alignments which may be performed in the event of different component changes. In most cases the realignment may be made by selecting the appropriate section from the following sequence. This presupposes that only one component is out of its 'correct' position.

NOTE: The rotator prism is prealigned at the factory and it is extremely unlikely that this is the cause of any spot orbit or other output problems (see Section 7.5). It is easy to tell if the prism is at fault as the spot orbit becomes cardioidal. Under all conditions of circular orbits it is not the internal alignment integrity of the rotator prism which can be at fault.

An outline of the major alignment sequence and tasks is given as Table 7.4 which further refers to the sections where individual details and instructions are to be found.

PROJECTION SYSTEM ALIGNMENT

- 7.4.1 Reduce the laser output power to CLASS 1 operation by controlling the tube current. The 'light control' may be the more stable and reduce the chance of the laser going out. Do not use an attenuator as the thickness of material and reflections from its surface may impair the alignment. An attenuator may

TABLE 7.4. ALIGNMENT SEQUENCE AND TASKS

	<u>Section(s)</u>
PROJECTION SYSTEM ALIGNMENT	
1. Laser Internal Alignment	1 - 3
2. Beam Position and Pointing at Box Entrance	4,5
3. Beam Position and Pointing to Transceiver Mirror	6 - 9
4. Beam Position and Pointing through Image Rotator Prism to Final Output	10 - 13
5. Centration of Transceiver Mirror	14
6. Set Up Screen	15
7. Focusing Lens and Wollaston Prism Mounting	16,17
8. Inner Transceiver Lens Collimation	18
9. Outer Transceiver Lens Placement	19
10. Orbit Minimisation	20
11. Wollaston Rotation	21
12. Beam Parallelism	22
13. Final Orbit Alignment at Outer Transceiver Lens and Sampling Volume	23 - 25
14. Place Alignment Stop and Criteria of Alignment	26
RECEIVER SYSTEM ALIGNMENT	
15. Location of Sampling Volume	27
16. Mounting of Fiber Optic Needles	28
17. Position of Enlarging Objective	29,30
18. Focus of Enlarging Objective	31
19. Fiber Optics Alignment	32 - 34
20. Cross Stop Alignment	35
21. Field Stop Position and Alignment	36
22. Review Checks	37,38

be used in the parallel section of the input laser beam if it is aligned with sufficient care to avoid any change in beam steering or multiple walk-off effects. It is necessary to allow several minutes warmup time.

- 7.4.2 Remove the top and both side covers, observing the cleanliness precautions outlined in Section 7.2. Strip the spine plate of components 4 through 10 except 6, the image rotator prism, which may be left in situ unless it requires attention. Identify components on Figure 1.1.1.A. Clean, repair, or renew as necessary.
- 7.4.3 Make sure that the laser is bolted down tightly, has been on for some time, and is in a stable operating condition. By use of the "Vertical and Wavelength" knob (top control) peak the laser power. It is seldom necessary to touch the "Horizontal" knob (lower control). The laser should be tuned to the 514.5 nm line unless there is some special reason why, for the contemplated experiment, it should be otherwise. The system, once aligned, should not be sensitive to change of wavelength. If these controls seem especially free, you may tighten the clamps onto the adjustment screws, an action performed with the laser cover removed (see laser handbook).

This power maximisation, most easily performed by observing either of the power monitors supplied with the laser, in the current control mode, also guarantees that the output will be TEM_{00q} of clean Gaussian profile about 0.9 mm diameter.

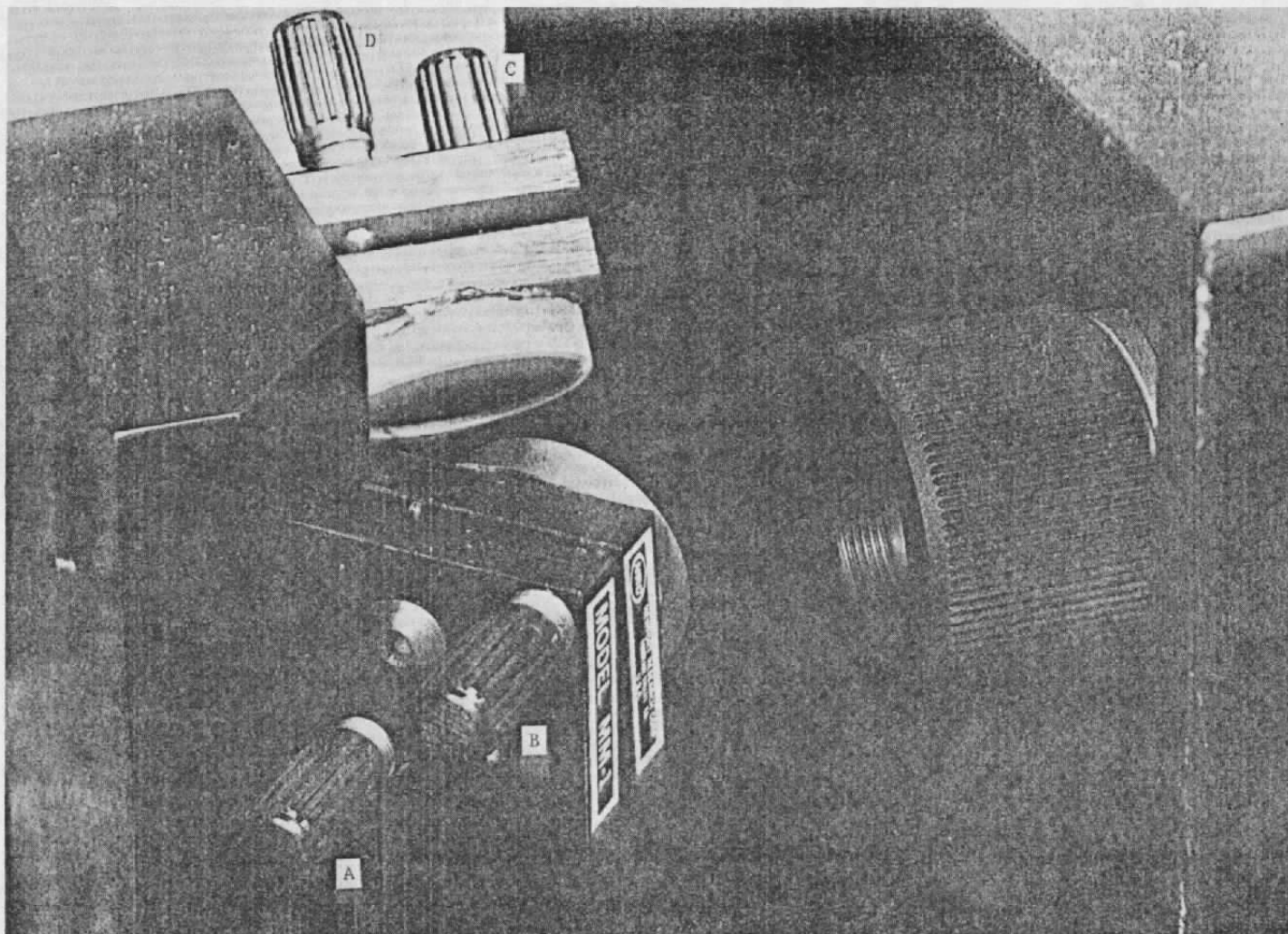


FIGURE 7.4.5 FRONT OF LASER ADJUSTMENTS

- 7.4.4 Tape a microscope cover slip to the top plate across the hole where the laser beam is to enter the box.

Use easily removable masking tape and lightly smear the cover slip with a finger. Make sure the slip is taped down all the way round and is thus as flush as possible with the plate which supports the laser.

Confirm that the external mirror mount post and the two mirrors are tightly clamped.

- 7.4.5 Using the four screw adjustments on the two external mirrors (screws A to D in Figure 7.4.5), arrange that the input beam shall be in the middle of the entry hole and perpendicular to the surface. This is guaranteed when the multiple reflections between the cover slip and the laser output mirror are coincident. This is a four-dimensional search, but can be rendered as two two-dimensional searches by using A and D as a pair and B and C as a pair. Do not touch these mirrors again, yet. It is a good idea to replace the top cover as a precaution against accidental contact with the adjustment screws.

- 7.4.6 Unless the mirrors 3 and 4 have been removed, the mounting positions will be correct. If they have not been removed, ignore the mounting instructions which follow, merely performing the adjustments of screws E through H. If they have been removed, proceed.

Arrange mirror 3 to be square and parallel to its adjustable mount and bolt it in position such that

the point of contact of the light is near the center of the mirror and 1.2 inches below the underside of the top plate. It will be 1.5 inches from the spine plate (which carries all components in this projection system). Bolt the mirror and support rigidly to the spine plate.

- 7.4.7 Adjust this mirror to make the beam parallel to the spine and top plates at the above distances. Use screws E and F on Figure 7.4.7.
- 7.4.8 Bolt mirror 4 in position so that the beam may be made parallel to the spine plate (1.5 inches away) and the baffle plate (2.70 inches away) and may pass directly over the center of the hole which supports/ will support the transceiver mirror. Tighten the mirror support.
- 7.4.9 Using screws G and H in Figure 7.4.7, arrange that the beam satisfies the dimensional specifications of 7.4.8.
- 7.4.10 Fix the transceiver mirror to its stub. It can be tightened enough to prevent casual movement. Arrange that its mount stub shall be centered in its oversize mounting hole. Do not forget the washer. If the cross stop is not already removed, remove it now. Put it somewhere safe.
- 7.4.11 Make translucent targets which look like Figure 7.4.11 or similar. Center one on the input face of the image rotator prism and one on the output face of the optical head. (The one on the prism must be cut down to a suitable size.)

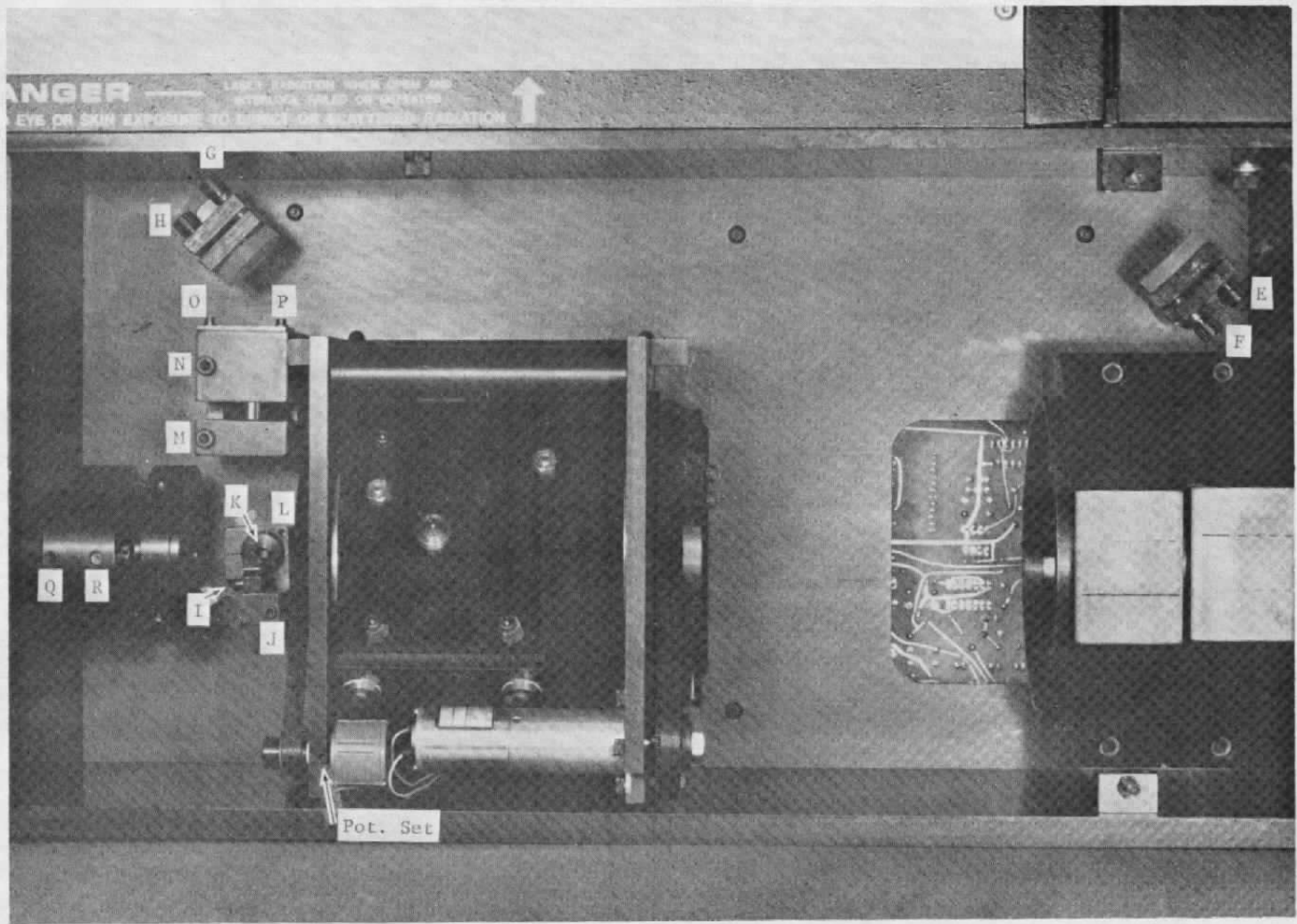


FIGURE 7.4.7 INTERNAL ALIGNMENTS I

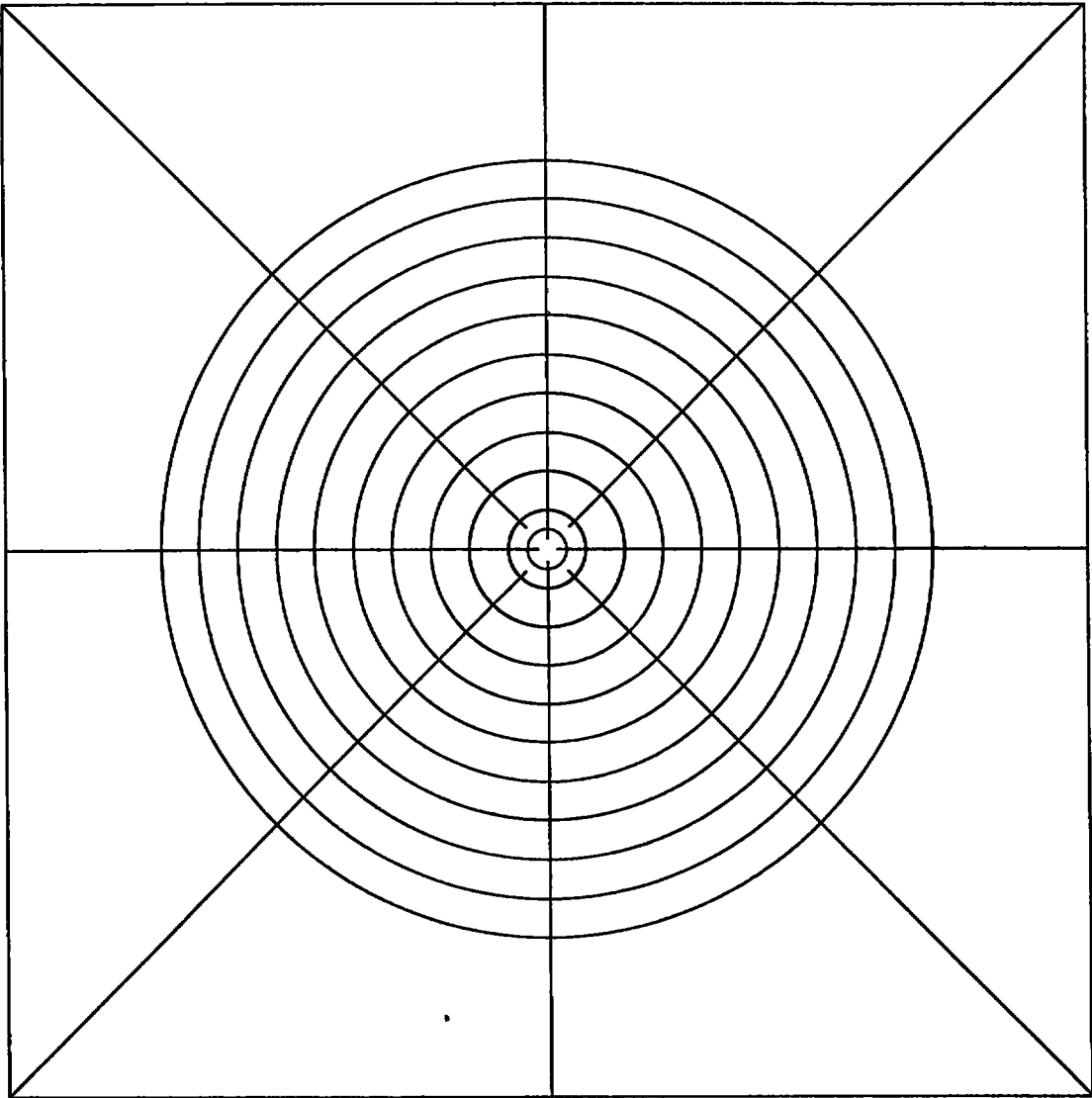


FIGURE 7.4.11 TARGET

- 7.4.12 If for any reason the image rotator was removed as under 7.4.2 for cleaning or other attention, it may now be replaced; otherwise, continue with 7.4.13.

Mount the rotator prism assembly and fix with three screws only.

- 7.4.13 By judicious manipulation of the transceiver mirror assembly with the screws I through K sufficiently slack to allow movement with slight stiction, arrange that the beam shall pass through the exact center of both 'targets'.

- 7.4.14 By further manipulation of L, K, and J, make the incident beam fall in the centre of the transceiver mirror, both in height from the spine plate and position using the nylon faced jacking screw and the play in the mounting hole.

Do not derange the alignment which was correct under 7.4.13, or if you do, make sure it is obtained again before you move on from this section.

- 7.4.15 The laser beam will now point out of the front of the instrument. There will be some scatter from the translucent targets which are still in place, but ignore this. Arrange for the beam to strike a surface between 3 m and 5 m away. Closer than 3 m gives too little magnification, and more than 5 m becomes a tedious walk. This surface may be usefully covered with squared paper with the lines horizontal and vertical - use a spirit level to level both the optical head and the screen. This screen should be

approximately normal to the beam to minimize later difficulties (See Section 4.5).

If the image rotator prism is rotated through full travel, the spot should not orbit by more than a few mm's. Tape a smaller plain sheet of paper to the squared screen using removable masking tape. You will use many such pieces of paper and wish to discard old calibration points to avoid confusion. Mark the centre of the beam orbit.

- 7.4.16 Assemble the Wollaston prism and focusing lens support block. For outer transceiver lens throws of 400 mm to 700 mm and where the machine is to be used with turbulence levels in excess of 0.5% to 1%, mount the front face of the focusing lens level with the end face of the mounting block. This axial position is a fine tune adjustment on the parallelism of the two spots near the focal region and may be important for low turbulence levels. It also differs slightly for different focal lengths of output transceiver lens. It may be changed with only minor readjustment of the final system should it be necessary to work with very low turbulence levels and hence very good parallelism of the spots over the length of the sensitive volume.

Mount the Wollaston prism with the black paper disc between it and the focusing lens. Slide it as far towards the lens as it will go. Arrange it to be at approximately 45° to the sides of the block. There are four possible positions. Only two will be satisfactory to allow the final spot orientation

to correspond to that of the fiber optics. There will be a later opportunity to correct this if you get it incorrect at this stage. It does not matter which way the light goes through this prism and hence it has no preferred 'right way up'.

Do not mount the aperture plate.

- 7.4.17 Arrange the position of the Wollaston mount block to be parallel to the sides of the box and to allow light to pass square and centrally through the focusing lens to centre the final output image. If the incidence is not square and central, there will be residual astigmatism which will impair the final performance. Tighten the support bolts for the mounting block and make sure that the focusing lens lock screw is tight. A demonstration of correct placement of this component is the recentration of the spot on the transceiver mirror and the uniform spread of the bright patch of light on the screen about the previously marked point.
- 7.4.18 Mount the inboard transceiver lens in the inboard lens mount the correct way round (see Figure 7.4.18) leaving the yoke clamping screws a little loose. Place an opaque mask with a 1 inch hole in it symmetrically over the output beam. Measure the beam diameter at the screen. Adjust the position of the transceiver lens until the diameter of this circle (to the appropriate part of its diffraction rings, see standard texts on physical optics) is about 1 inch.

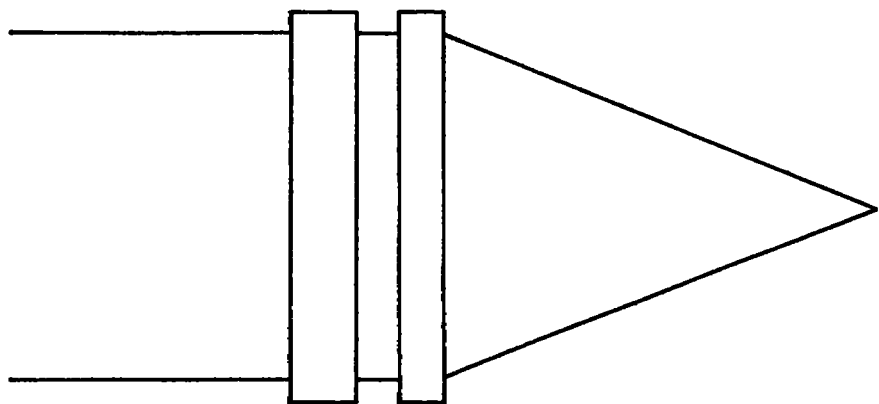


FIGURE 7.4.18 TROPEL LENS SENSE

Make sure there is NO INTERMEDIATE FOCUS, by running a card along the length of the beam. Tighten the lens mount yoke.

7.4.19 Mount the outer transceiver lens chosen for the present application. Its axial position is not significant and may be used to adjust the exact throw over a small range. Normally at this stage it should not be pushed hard against the inner transceiver lens to allow movement under the repeat of 7.4.18 which may be necessary after 7.4.22. After this fine tune operation, it may be good to push the outer transceiver lens hard against the inner to ensure squareness and maximize rigidity. It is necessary to tighten the yoke to prevent casual movement even though it may be moved later.

7.4.20 Remove both translucent targets so that scattering through them will not impair the beam quality at the spots. Mount a $\times 20$ microscope objective with a large entrance face so as to project the region of best focus of the spots on to the screen. Tape a clean sheet of blank paper to the screen so that the spot orbit stays within its bounds.

On rotation of the rotator prism, the spots will orbit the common centre of gravity of the two spots. There will be a dim spot of light at this central point. This central point will most probably trace a circle twice for each rotation of the prism. Circular orbitting is caused either by the entrance direction or the entrance position at the image rotator prism being slightly away from the mechanical rotation axis of the prism assembly.

Using only turning mirror 4, screws G and H, and the transceiver mirror angular adjustment screws I and J slackened, walk the beam about the entrance face of the prism to minimize the size of the orbit made by the spot on rotation of the prism assembly. It is necessary to get both the entrance position and angle exactly correct. Necessary adjustments should be very small and should not take the beam perceptibly from the centre of the focusing lens. If it does, it will be necessary to move the focusing lens mount block to re-centre the unit and repeat from that point in the alignment (7.4.17). At this time, it is not necessary to arrange for the circular centre orbit to be much less than the spot separation. Further precision will be required in section 7.4.23 in due course.

Some hints to ease this tedious adjustment are to use a resting position of the rotator prism such that its plane of reflection symmetry including its rotation axis is parallel to the side or top of the optical head box, and to use the screws G and J together and alternately with H and I together.

If the beam now strikes visibly away from the centre of the transceiver mirror, repeat 7.4.14.

- 7.4.21 Slacken the Wollaston prism retainer screw (N) and rotate the prism until the two spots on the screen are of equal brightness. There are four angular positions where this will be true. Only two of them are acceptable, those where the plane of the spots is ultimately imaged on the plane of the fiber optic

needles. Choose one of these. It is convenient, and sufficiently accurate, to use a laser power meter for this function.

- 7.4.22 Following the initial remarks on beam parallelism in Section 7.4.16 is included a more precise discussion. This section is only relevant for very low turbulence situations.

If you need very high parallelism -- say to better than 0.1% -- it will be necessary to proceed as follows. For visualization, arrange that the sampling volume is suffused with a light mist. Suggestions are dry ice in warm water, cigarette smoke, incense, or a foggy day. Observe the beams to look like the middle diagram (B) in Figure 7.4.22. This will almost certainly be true for the earlier procedure will have reduced any divergence to a (probably significant) fraction of 1%. To improve the system further, it is necessary to measure the divergence with high precision and this is best done by using a $\times 20$ microscope objective as illustrated elsewhere and racking it along the beams with a calibrated linear stage. It is not very useful to move the objective more than about 2 mm (total) because it will not be easy to place the centre of the spot with sufficient accuracy outside this range. By measuring the spot separation as projected on the screen, it is possible to adjust the axial position of the focusing lens until it is reduced to zero. Actually, about 0.1%/mm is the best it is reasonable to achieve. At this value, there would be no significant error

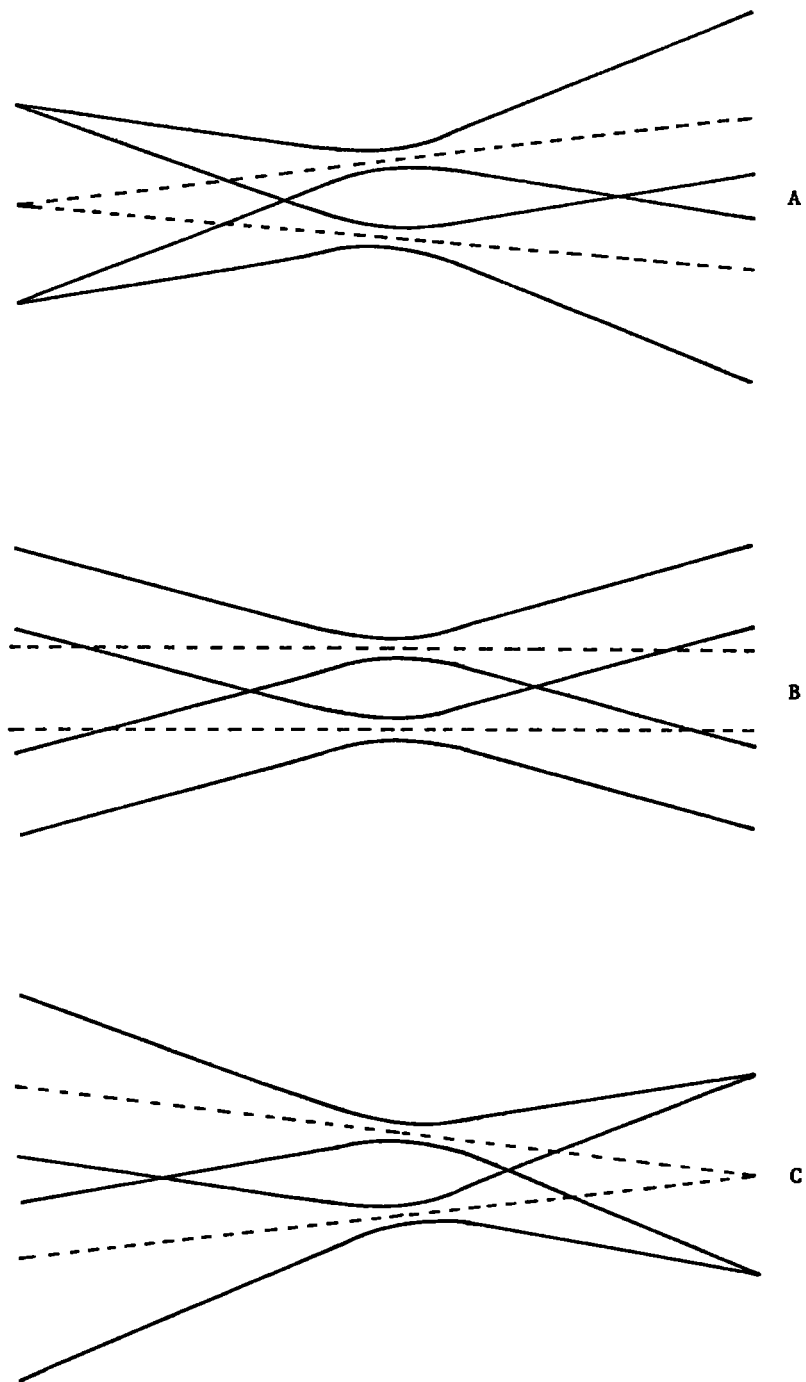


FIGURE 7.4.22 BEAM PARALLELISM

from this source above .05% turbulence. It is necessary to repeat this procedure for each output transceiver lens.

- 7.4.23 Check that the spots orbit not too far from their centre of gravity. Repeat the work of 7.4.20. This time, the adjustments will be very small but the criteria to be met are tighter. This is a final output system optimisation.

NOTE ALL CLASS IIIB LASER SAFETY REQUIREMENTS AND PRECAUTIONS!

Turn the laser to maximum power under 'light control'. Wait 20 minutes for thermal stabilisation. Use the instructions in 7.4.20 to reduce the magnified spot centre orbit to a small fraction of the spot separation. The errors remaining accrue from three sources:

- a) Circular orbits derive from errors of direction or position or a combination of both at the entry face to the image rotator prism. Theoretically, this may be eliminated to give a pure cardioid.
- b) Cardioidal orbits derive from internal prism alignment which may be rectified if sufficiently large by the sequence, or intelligently selected parts thereof, in Section 7.5. The early part of this sequence may be omitted since the residual errors are very small and only minute changes of position of screws 7 through 13 (Figure 7.5) should be attempted.
- c) Glitches derive from play, especially end float, in the prism bearings. These will be very small, but

may never be reducible to zero. Errors of up to 0.1 milliradian may occur in extremely unfortunate combinations of circumstances, but 10 microradians is more likely -- corresponding very roughly to 0.1 of the spot separation.

Simultaneous with the orbit criterion at the screen, it is necessary that the illumination of the outer transceiver lens shall be central and symmetric. This is not a mutually exclusive criterion, but MUST be simultaneously achieved. Again, this is correct when the input direction and position to the rotator prism is correct. There are necessary and sufficient adjustments for these simultaneous criteria. (Screws G, H, I, and J -- if all these, especially G and K, are used at this stage in the game, it may be necessary to repeat parts of the earlier sequence.)

- 7.4.24 Remove the $\times 20$ objective and note that the pattern on the screen is a roughly Gaussian patch with square terminator and some diffraction patterns, especially near the edge.

This will be quite symmetric if 7.4.14 was performed with care. Arrange that the alignment stop plate, fixed with the screws and washers O and P, just cuts off the corners of this square with perfect symmetry. This will be a subsequent datum making realignment in the field very simple if its cause does not derive from physical damage to the instrument.

Be careful not to touch any optical surfaces at any time you have your fingers inside the instrument to perform adjustments.

7.4.25 Turn the laser back to 'current control' and reduce the power to Class I operation.

7.4.26 You have now completed the adjustment of the output system for projection of the two spots into the test space. Now the alignment stop is correctly placed, perfect alignment may be restored by use of mirror 1 only under the following causes of misalignment:

- | | | |
|---|---|----------------------|
| a) laser aging, | } | up to certain limits |
| b) thermal changes, | | |
| c) box distortion through mishandling, | | |
| d) change of wavelength (different laser line). | | |

In general, this mirror 1 correction will be a complete correction including the receiving system alignment, which is fixed conjugate with the projected system and will not change with the above properties.

Outside the limits of mirror 1 correction using the alignment stop (and if necessary the normal central input criteria of 7.4.5 simultaneously), the question must be asked, "Is the misalignment far enough away from what I require to merit realignment of its system?"

The criteria of projection system alignment are summarized in Table 7.4.26.

RECEIVER SYSTEM ALIGNMENT

7.4.27 Obtain a fine ground steel surface (a machine ruler is ideal). Slide the surface along the beams through the crossing point until the far field speckle pattern

TABLE 7.4.26. FINAL ALIGNMENT CRITERIA FOR
PROJECTION SYSTEM

<u>Property</u>	<u>Possible Achievable with This Design</u>	<u>Reasonable Standard for Extended Use</u>	<u>Remarks</u>
Spot Orbit			
a) Prism	0	10 μ rad.	Cardioidal
b) Input	0	10 μ rad.	Two circles
c) Glitch	0-100 μ rad.	Fixed	Depends on instru- ment
Output Centration	0	1-2 mm	
Spot Quality	Diffraction Limited	10% Elipticity from Astigmatism	Focusing lens not square to beam
Laser Tube	Maximise power by mirror alignment. Mode structure is then OK (TEM _{00q}).		
Spot Intensity	Equal	Within 1% or Better	
Spot Parallelism	Parallel	Low Turbulence 0.5 m rad. High Turbulence 1 to 5 m rad.	Depends on the needs of the user and the present appli- cation

has structure of the largest size. At this point, the speckle pattern dimension will be of order 4° to 7° of arc depending on the surface of the scatterer and will contain closely spaced erratic fringes. You can observe these on the front of the instrument or on any surface available in the room. Since the laser is running at low power, it may be useful to darken the room.

- 7.4.28 With none of the cross and field stops and the enlarging lens mounted, bolt the carrier of the fiber needles to the spine plate. Arrange with the screws X through Z (Figure 7.4.28) that the ends of the fibers shall be close together and near the centre of the hole in the mounting block.
- 7.4.29 Slide the enlarging lens (for most systems, a $\times 7$ microscope objective on a 10 mm mounting tube) into its receiving hole and lightly nip it in position with screw Q.

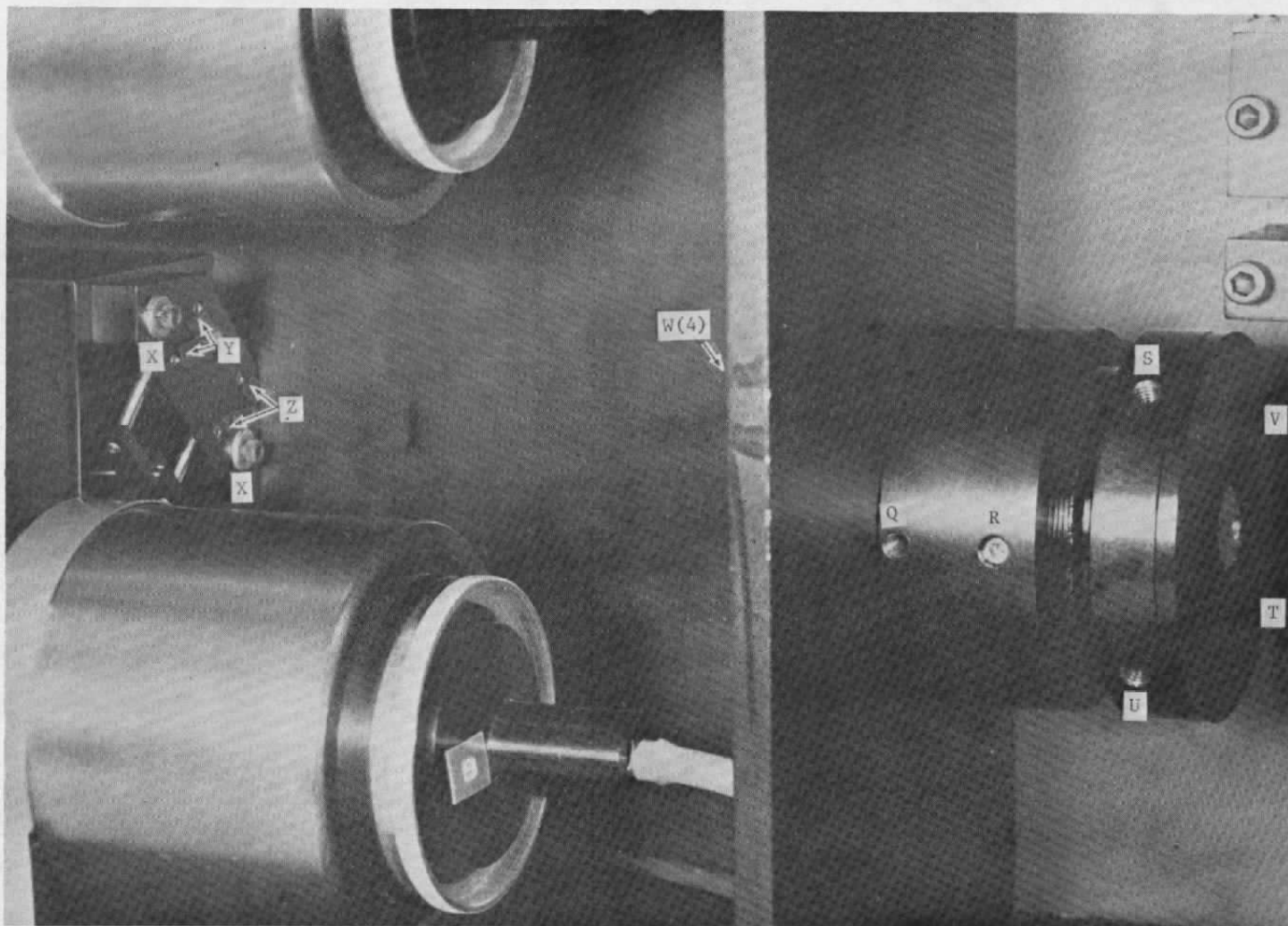


FIGURE 7.4.28 INTERNAL ALIGNMENTS II

- 7.4.30 Slacken the four screws (W) on the back of the baffle plate and centre the enlarging objective to place the return spot images as near the needle ends as possible; certainly within 0.5 mm (.020 inches). The image may not be in focus -- do not worry.

Tighten the four screws (W).

- 7.4.31 Loosen the set screw (Q) holding the shank of the enlarging lens holder. Slide the objective very gently to obtain the best focus on the fiber needle ends or on a piece of thin white card fixed in the plane of the fiber needle ends. The card should not be more than a few thousandths of an inch away from the plane of the fiber needle ends. Use a low power microscope to observe the images. $\times 20$ to $\times 30$ is ideal. The spots will change as you search through the planes for the 'best focus'. Choose a point where the 'disc of least confusion' is as small as it may be, certainly no larger than the size of the fiber which will be clearly visible in the microscope and should be clean and free from visible damage. The lenses concerned here are very well corrected and the best position will be very sharply defined. Even so, there will most likely be some residual spherical aberration. There may also appear traces of astigmatism and a fair amount of diffraction. This diffraction will look even more complex after the cross stop is fitted, so do not worry about it. There will always be a clear point of brightest centre. You may find that the

adjustment of this lens is facilitated by using a tube with a female microscope objective thread on one end. These are standard and readily available.

Tighten the set screw. It has a nylon face, so will not feel very tight. Do not overtighten or the nylon will cold flow and make the adjustment very difficult for the next occasion.

- 7.4.32 Slacken the screws X and use what little rotational play there is to line up the ends of the fibers with the mean line connecting the two spots. This is to allow for the Wollaston prism not being at exactly 45° because the equality criterion is dominant. The fiber faces must lie somewhere along this datum line. See the sketch 7.4.32. Tighten both the screws X.
- 7.4.33 Slacken two set screws Y. These have nylon faces and will again cold flow if overtightened. Slide the upper needle to make it coincide with its spot. Do the equivalent with screws Z. Whilst these are not fully tight, it is possible to lever the block which holds the needle away from the plane face of the mounting block. This enables a very small amount of side play in the direction $\pm x$ on Figure 7.4.32.

The final alignment is best performed by observing the back of the fiber (in the mount which couples it to the photomultiplier tube housing) with a power meter and performing small adjustments of position as above with the screws not quite tight. Finally, tighten screws Y and Z.

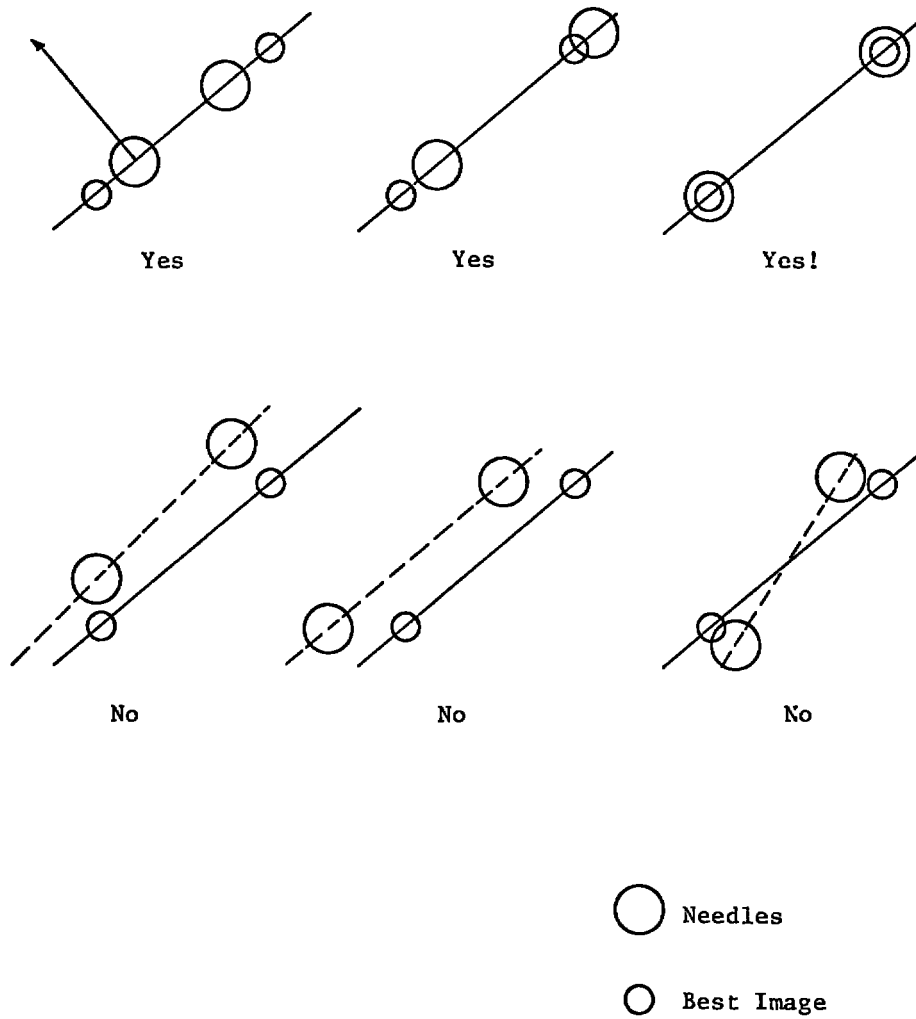


FIGURE 7.4.32 RETURN IMAGE ON NEEDLES

- 7.4.34 Look at the PMT ends of both fibers at the same time. It is beneficial to tape some fairly thin white paper to these mount plates because the emission from the fiber is into a tight angle and it is awkward to line one's eye up with both of these simultaneously. Note now that if the scatter plate is slid along the optical axis, both beams extinguish together and over a few mm movement of the plate. If you are very observant, you will observe that at one point in the excursion to extinction, you will detect a minute brightening. Do not worry about it. It is cured by later operations.

The beams should appear quite similar -- a bright centre region surrounded by a distinct but dimmer halo. If any other appearance is present, the fibers may be dirty or damaged. If the appearance is corrected by cleaning, this will suffice. If not, the fibers should be replaced. The damage will mainly lead to loss of optical efficiency or unbalance between the two channels, but can also lead to loss of precise restriction of the depth of the sensitive volume.

- 7.4.35 Retrieve the cross stop from the 'safe place' of 7.4.10 and mount it with a washer behind the transceiver mirror. Its orientation should be such that the 'semaphore' arm which is pointed towards the base defined by the mounting hole is at the star-board side of the system.

Arrange a plane front surface mirror between the enlarging lens and the fiber optic needles -- be very

careful not to touch the needles -- to reflect the image of the spots on to the back of a sheet of translucent paper fixed to the starboard side of the box where the side cover normally fits. Note that as the scatter plate in the sample volume is moved along the optical axis that the cross stop interrupts a diametral sector of the now defocused image. Use the small amount of rotation available in the cross stop to prevent the circular image of one spot passing over the place corresponding to where the other spot has its focus. See Figure 7.4.35.

The real image will never be as clean as the idealized diagram. The pattern will be covered with speckles and irregularities which derive from the minute imperfections and structure of the scatter screen. Nevertheless, there must be a blank hole in the annular image where the focal spot centres (dotted) were when they were at best focus. The dark portion (not quite a sector) which is not aligned with the spots will invert when the scatter plate is moved from the sensitive volume in the opposite direction from its former movement.

Tighten the cross stop screw.

7.4.36 Fit the field stop by means of screws S through V.

Slacken the nylon faced set screw R.

Observe the illuminated face of the field stop plate with the low power microscope which you used formerly.

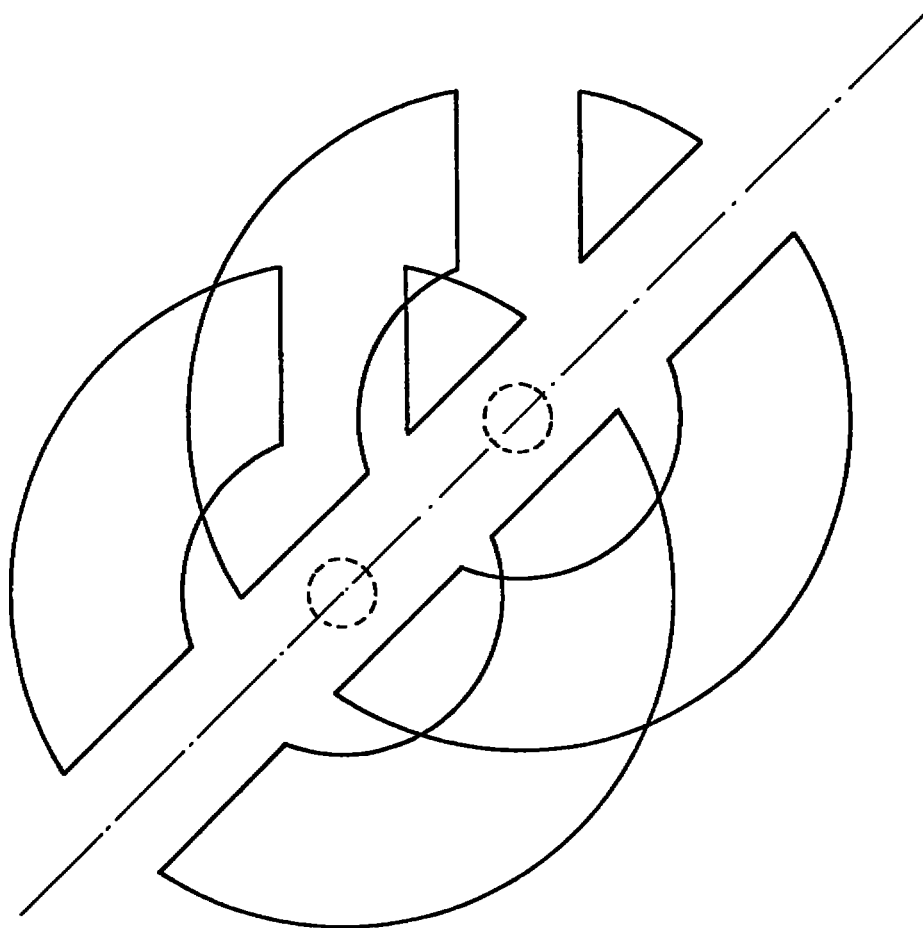


FIGURE 7.4.35 CENTER AND CROSS STOP IMAGES

Screw the field stop plate until the spots are in best focus -- a repeat of the criterion of 7.4.31, but now the spots will be smaller. However, the screw adjustment will make it quite easy. Measure and record the gap through which you can see threads and note the angular position of the plate which retains the screws for the field stop adjustment. Rotate this plate through 180° and replace the two set-screws with spring plungers (nylon faced set-screws with spring shanks). Two of these are provided in the accessory kit. Screw these up loosely when the field stop plate is centered. Rotate the plate 180° to give access to the pointed set-screws. Observing through the microscope, rotate the field stop until its holes line up in direction only with the bright images. Now, using the pointed set-screws and observing the ends of the fibers for maximum brightness and the stop plate for darkness because the bright images now go through the holes, move the stop plate in its own plane. When this criterion is achieved, rotate the plate 180° , replace the spring plungers with rigid set-screws, and turn the plate back through 180° . Tighten screw R and note that the above conditions are met (that the images of the two holes in the stop plate are symmetric about the bright points which illuminate the fiber ends). Check all screws for tightness while observing that the alignment is perfect.

- 7.4.37 Check that sliding the scatter plate along the optical axis of the spots now produces much sharper extinction with no trace of return brightening as the scatter plate moves away from the volume of maximum sensitivity. If you measure the change in return light from an

approximately Lambertian scatterer as it is racked through the sampling volume, it will have the approximate properties of Table 7.4.37 for a 400 mm high resolution (Tropel) outer transceiver lens.

Other lenses will have different criteria and it is up to the user to decide whether the precision of adjustment he has achieved is adequate for his present purposes.

There is an even more accurate method to centre these field stops and also assure that their plane of focus is correct. Using the front surface mirror of Section 7.4.35 and the x20 microscope objective, reimage the field stop a meter or two from the instrument. You will observe two circles corresponding to the field stop holes. When these are in sharp focus, the central portion of each hole should exhibit the disc of least confusion of the return images. The field stop adjustment may now be rendered near perfect by minute movement of screws S through V.

- 7.4.38 Review all the checks in this section and screw the fiber optic guides into their respective photomultipliers. Be careful to get the sense correct. The top fiber guide goes to the top PMT and is called Channel A. If desired, fit the narrow band laser transmission filters for the suppression of broad band light, e.g., from sunlight, self-luminous phenomena, fluorescent media, etc.

TABLE 7.4.37

FINAL ALIGNMENT CRITERIA FOR RECEIVING SYSTEM

Defined here with 400 mm f/4 TROPEL lens.

<u>Property</u>	<u>Specification</u>
Axial Rejection	Full Width to Intensity Below Peak
$1/\sqrt{e}$	< 360 μm
$1/e$	< 520 μm
$1/e^2$	< 720 μm
10^{-1}	< 800 μm
10^{-2}	< 1.2 mm
10^{-3}	< 2.5 mm
10^{-4}	< 7.0 mm
Fiber Optic Output Cone	$\sim 10^\circ$ Half Angle

APPENDIX VITHICK WINDOW ABERRATION EFFECTS
ON A LASER TRANSIT ANEMOMETER

INTRODUCTION

This appendix presents the results of a "quick look" study of the degree to which a thick optically flat window will degrade the performance of an otherwise diffraction-limited laser transit anemometer (LTA) system. The study is restricted to a concentric coannular transmitter-receiver system with the transmitted beams assumed to occupy the central portion of the transmitter lens. The lens is assumed to be ideal and geometrical ray optics and Snell's law are adequate to justify the points we intend to make. The transmitted beam is assumed to focus to a point in the absence of the window; the return scattered light is assumed to originate at a point scatterer located at the paraxial focus of the transmitted beam. The effects of diffraction are considered separately. Only one beam is considered as though it were along the lens axis for simplicity, although in a normal LTA system there are two beams symmetrically inclined at a small angle to the axis. This angle is sufficiently small to produce no effects which could be significant here.

As a figure of merit we calculate a diameter of the transmitted and received spots and compare these diameters with the $1/e^2$ intensity diameter of the transmitted beam which is predicted by Fresnel diffraction theory. Since diffraction-limited optics are assumed,

the window induced spherical aberration can be neglected when the geometrically computed spot diameters are much less than the transmitted spot diameter (or its image, in the case of the receiver).

FOCAL SHIFT RAY EQUATIONS

Figure 1 illustrates the shift of a point image produced when the transmitted light is not collimated. The dotted line indicates the focal position that would obtain in the absence of the glass block, and intersects the optical axis (z) at the point A, which is invariant with θ_i . When the glass block is present, the focus is shifted by a distance $b + \Delta b$ which is now a function of θ_i and which for paraxial conditions (i.e., $\theta_i \rightarrow 0$) tends to b and is illustrated as point B. The refractive index of the glass n_g is related to that of the surrounding medium n_o as

$$n = n_g / n_o \quad (1)$$

and is typically 1.5 for optical glass in air. Using Snell's law

$$\sin \theta_i = n \sin \theta_r \quad (2)$$

and the rules of geometrical optics, it is easy to write the total shift of focus as a function of incidence angle as

$$b + \Delta b = t \left(1 - \frac{\tan \theta_r}{\tan \theta_i} \right) \quad (3)$$

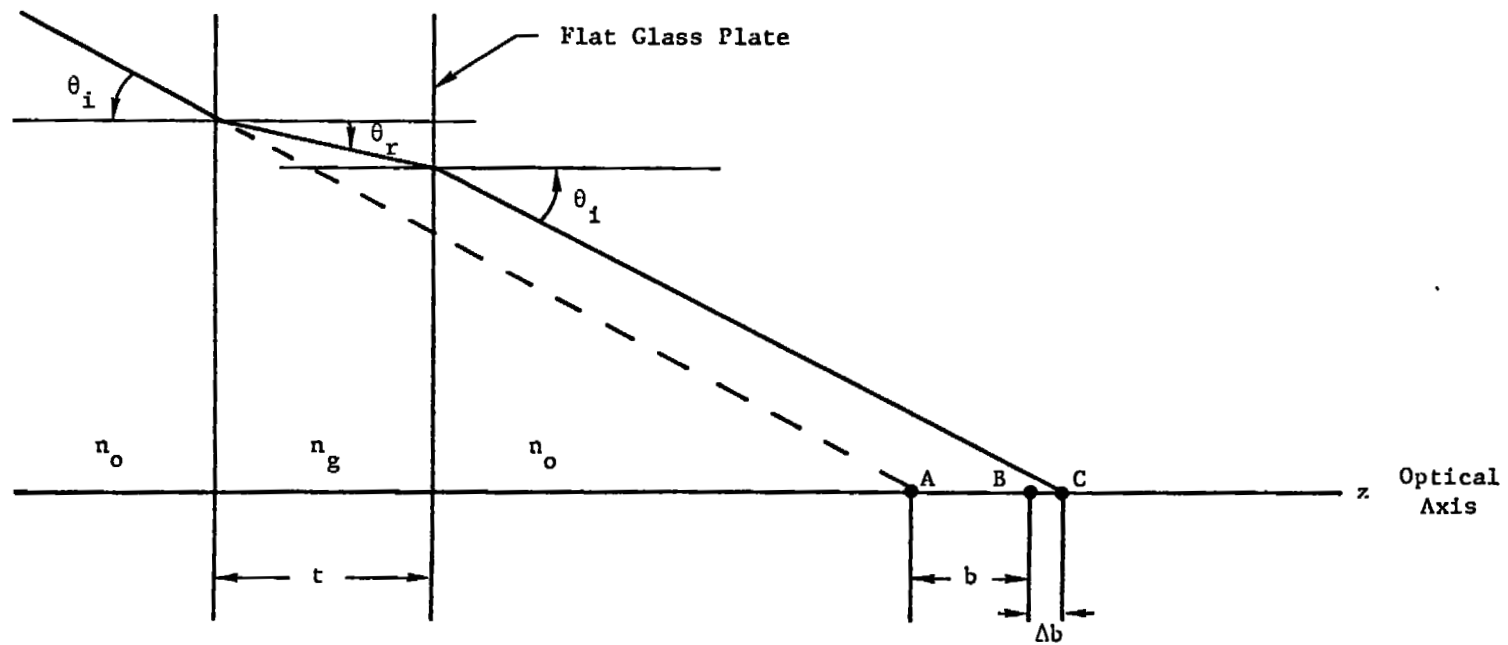


Figure 1. Shift of Focus by a Flat Window in a Converging Pencil.

For paraxial condition $\Delta b = 0$ and

$$\begin{aligned} b &= \lim_{\theta_i \rightarrow 0} t \left(1 - \frac{\tan \theta_r}{\tan \theta_i} \right) \\ &= t \left(1 - \frac{1}{n} \right) \end{aligned} \quad (4)$$

Observing that point C (Figure 1) is the *additional* shift of focus from the paraxial condition and hence corresponds to the effects of aberration caused by the flat plate we may rearrange Equations (3) and (4) to yield

$$\Delta b(\theta_i, n, t) = t \left(\frac{1}{n} - \frac{\tan \left(\sin^{-1} \left(\frac{\sin \theta_i}{n} \right) \right)}{\tan \theta_i} \right) . \quad (5)$$

Figure 2 is a plot of this function for $n = 1.5$ and a range of values of t from 0.25" to 4.0". The range of values of θ_i correspond to F/D ratios (focal numbers) from $f/4$ to $f/50$.

FOCUSED SPOT RADIUS (TRANSMITTER)

Figures 3 through 6 illustrate the way in which the window-induced aberration affects the focus when the window is normal to the optical axis. The rays from each different incident angle focus with different slope to different locations. The distance from the optical axis to each ray cone is a function y which depends on both location

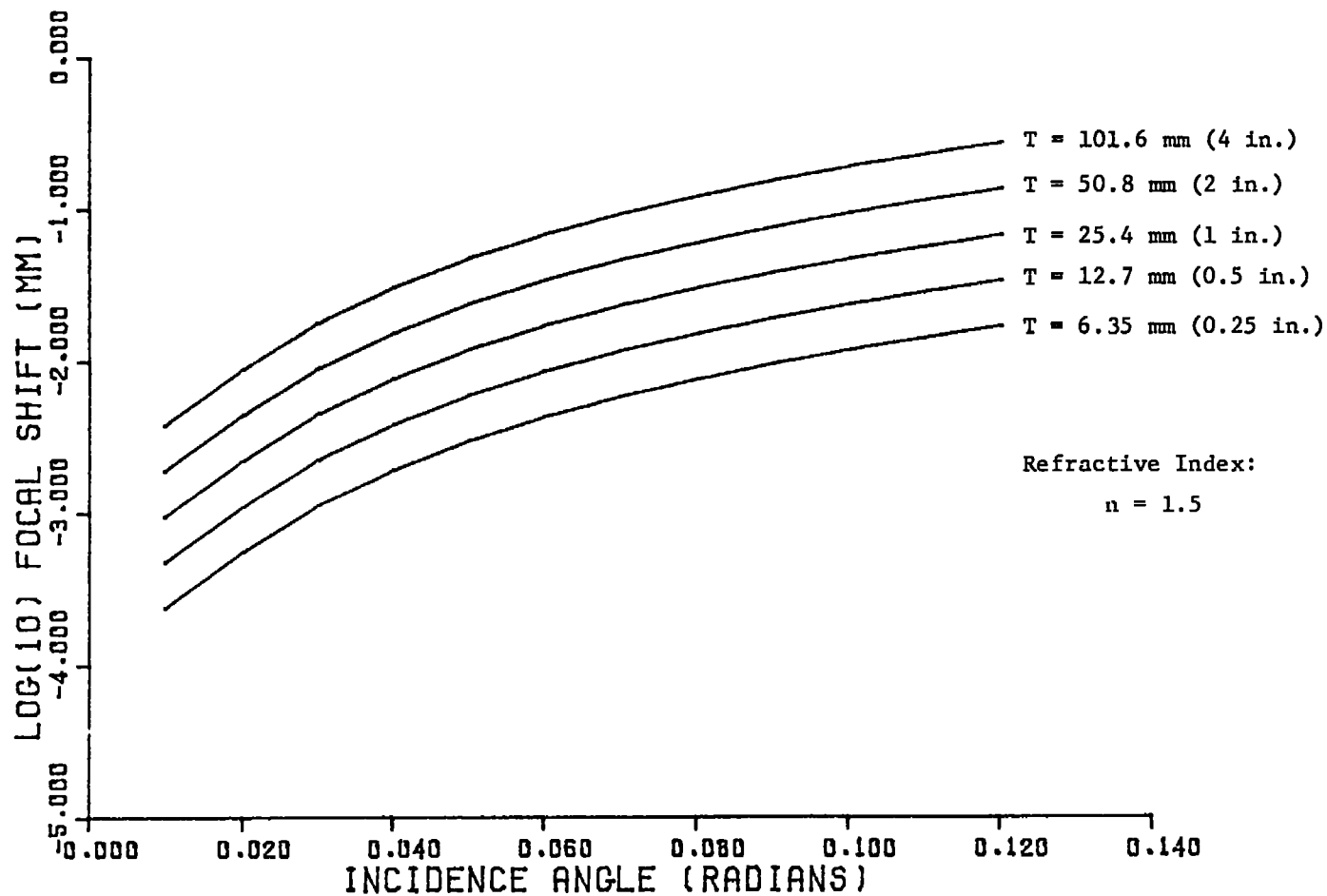


Figure 2. Geometric Focal Shift from Paraxial Focus for a Flat Window.

z (measured from the paraxial focus) and the incidence angle. Hence, the equation for the transmitted rays becomes

$$y(z, \theta_i, n, t) = [z - \Delta b(\theta_i, n, t)] \tan \theta_i \quad (6)$$

where θ_i (in radians) is positive in the figure for lines with positive slope. Figures 3 through 6 are plots of Equation (6) with the parameters t and n chosen to illustrate quantitatively the aberration for practical cases of interest. At the paraxial focus, the intensity pattern is bright at the center but has a large outer area with energy not well focused. A disk of least confusion occurs at a positive value of z where the outermost rays are contained in a smaller radius than they are at the paraxial focus.

Figures 3 through 6 illustrate graphically that the smaller the window thickness and the smaller the angle of incidence of the outer edge rays, the smaller will be the disk of least confusion. On the other hand, the diffraction limited radius increases with decreasing edge ray angle. Figure 7 is a plot of the diffraction limited $1/e^2$ focal waist radius for three wavelengths of light with the focusing angle defined by the $1/e^2$ intensity cones in the portion of the radiation away from the focus. The equation for the beam waist radius is

$$W_o = \frac{\lambda}{\pi} \cotan \theta_i \quad . \quad (7)$$

From Figures 3 through 6 it is possible to obtain values for the radius of the disk of least confusion for different limiting values of θ_i where there is no lower limit to θ , i.e., a solid cone.

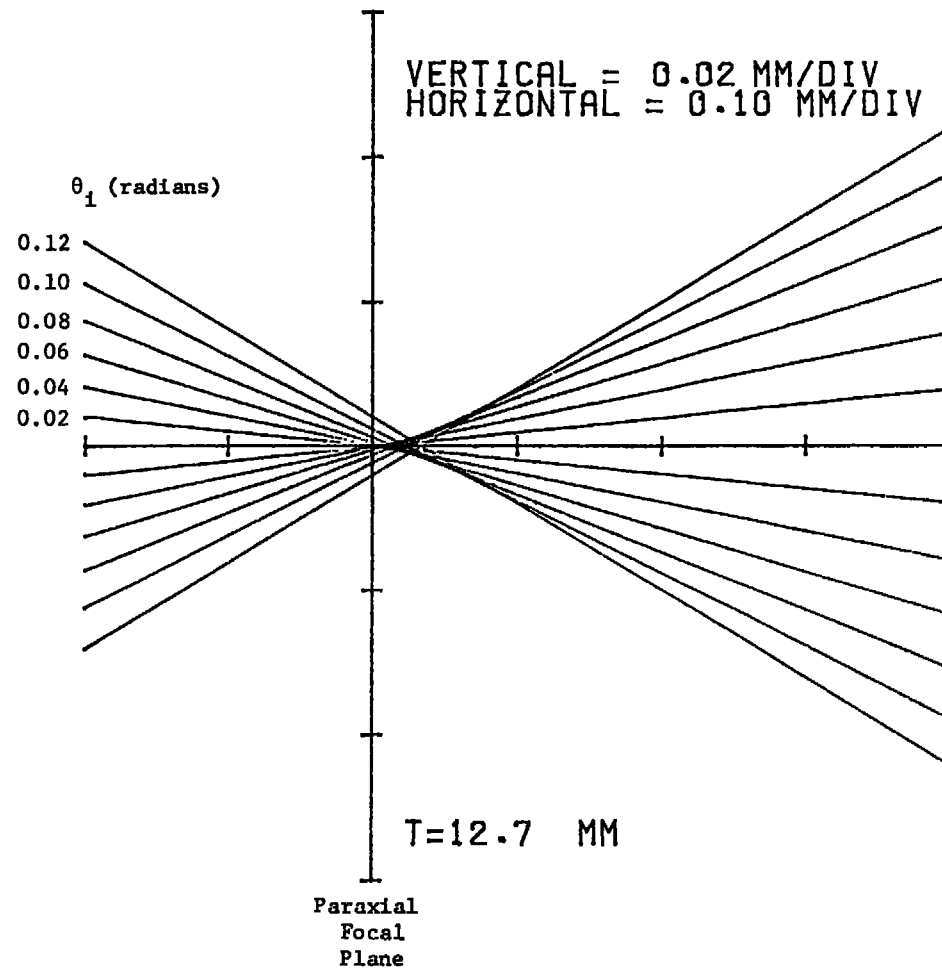
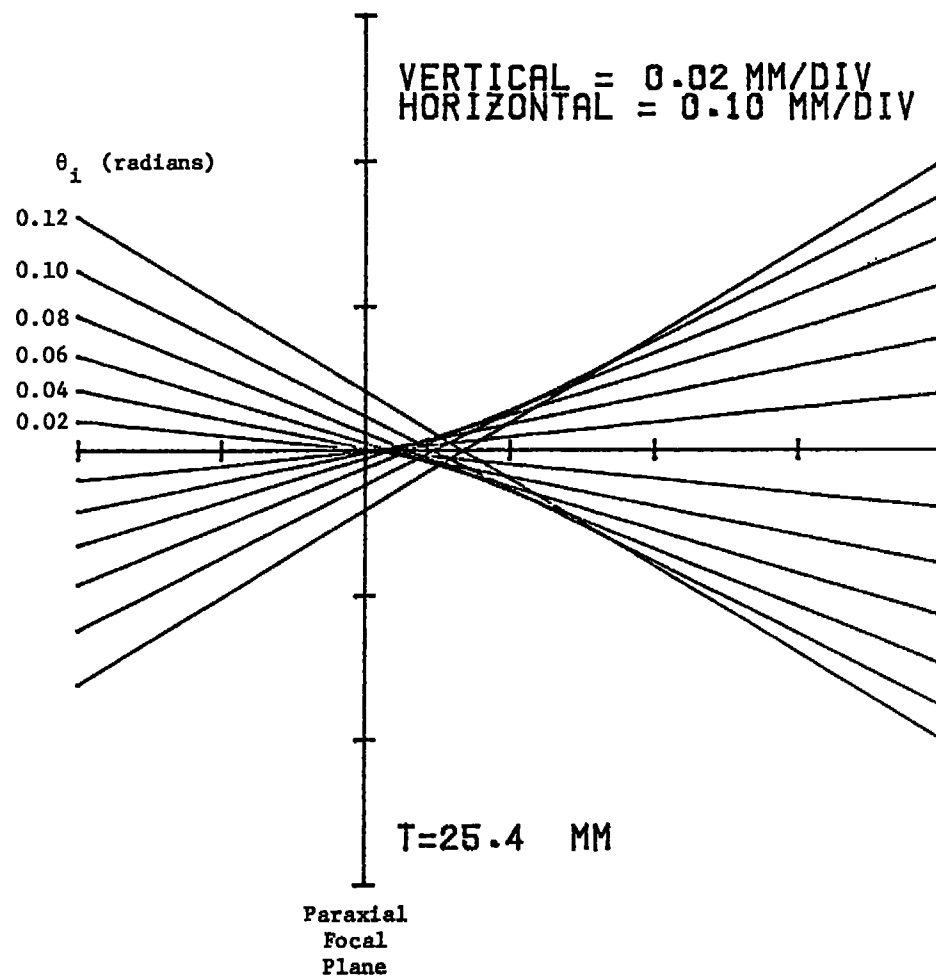


Figure 3. Focal Spot Ray Diagram: $t = 0.5''$

Figure 4. Focal Spot Ray Diagram: $t = 1.0''$

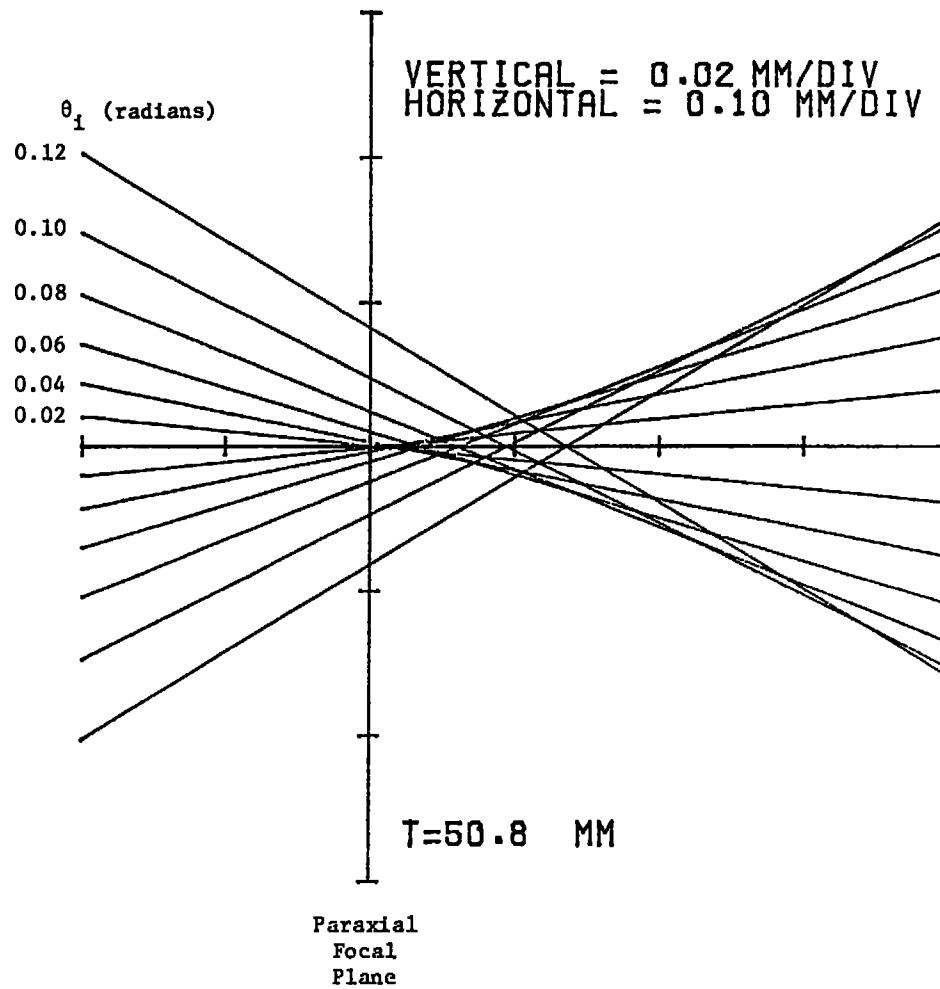


Figure 5. Focal Spot Ray Diagram: $t = 2.0''$

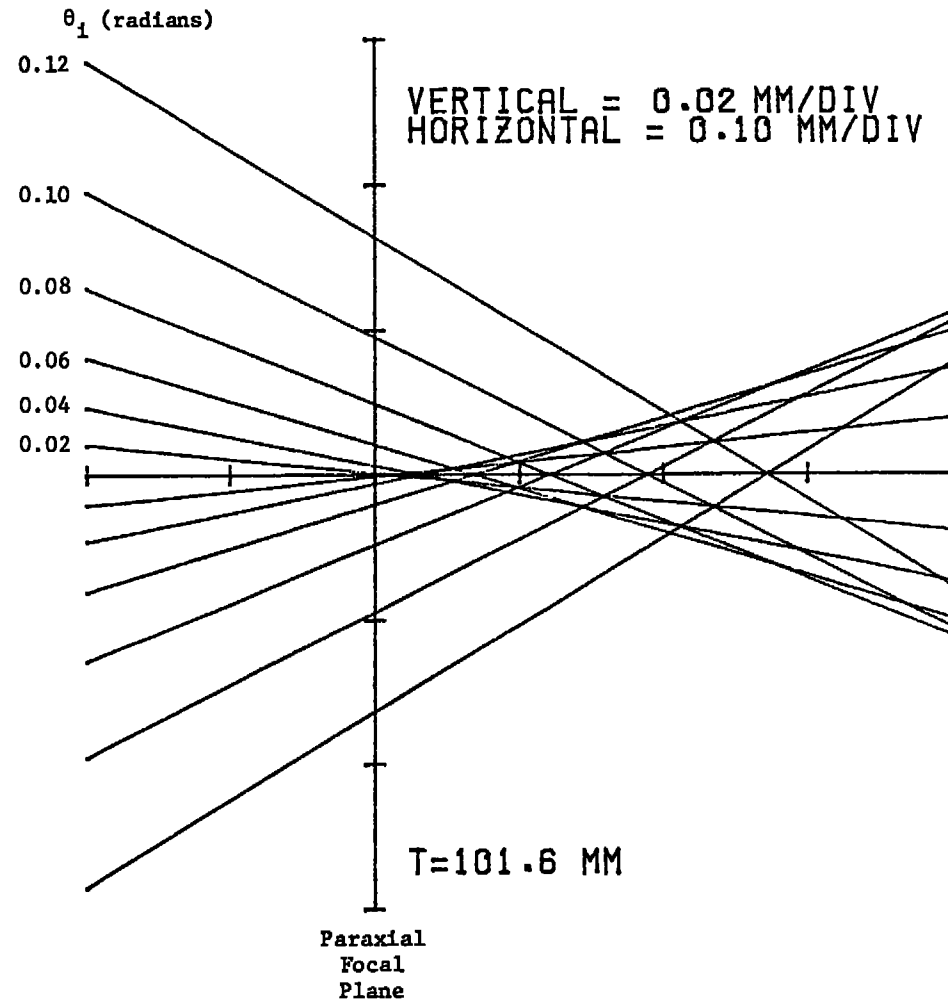


Figure 6. Focal Spot Ray Diagram: $t = 4.0''$

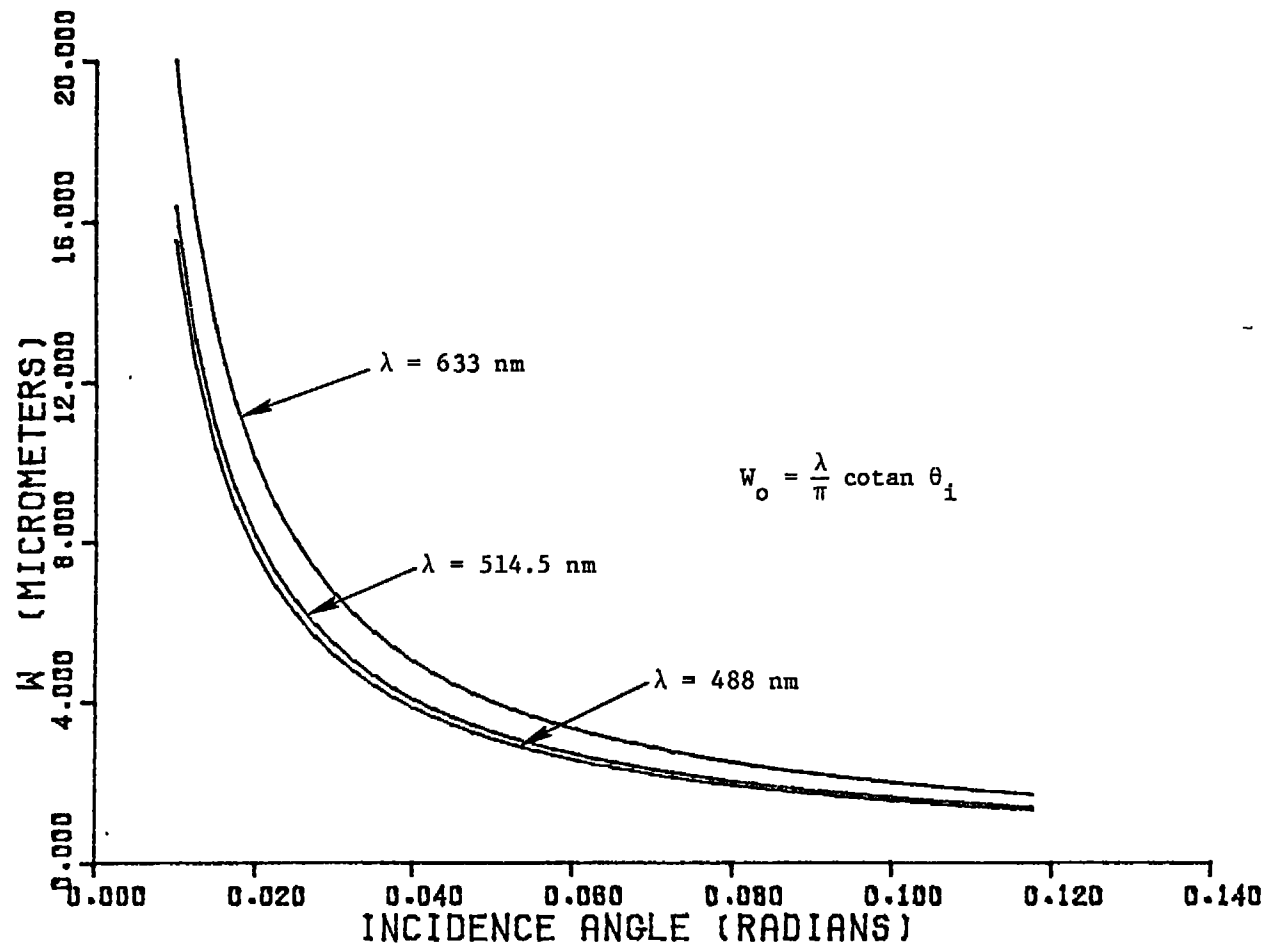


Figure 7. Gaussian Beam Waist Radius as a Function of $1/e^2$ Incidence Ray Angle.

These are plotted on Figure 8 for a range of thicknesses from $t = 0.25''$ to $t = 4.0''$ and for θ_1 (max) from 0.02 to 0.12 radians.

The geometrical definition of the disk of least confusion is in error by the influence of diffraction and the criterion that the effect of the glass block shall not be seriously detrimental is equivalent to the quantitative statement that the convolution of the geometrical radius with the Gaussian radius shall not exceed the value of the Gaussian radius by more than a certain figure, chosen by the application.

It is clear from Figure 8 that with θ_1 (max) of 0.062, equivalent to an f/8 transmitter, there is almost no significant spot expansion even for glass thicknesses up to 4.0". For thinner pieces of glass, this effect becomes even less significant.

Thus, the spherical aberration induced into the transmitter beam is not significant, especially when compared with aberrations which are introduced into the system by the receiving optics with its greater values of θ_1 . These effects are discussed in the next section.

SPHERICAL ABERRATION OF THE RECEIVER

Figure 9 illustrates schematically both the transmitter and the receiver rays for normal incidence of the optical axis on the flat window. The effects are, of course, grossly exaggerated in this diagram.

In Figure 9(a) the deterioration near focus described in the preceding section is indicated by the edge rays (point source over aperture)

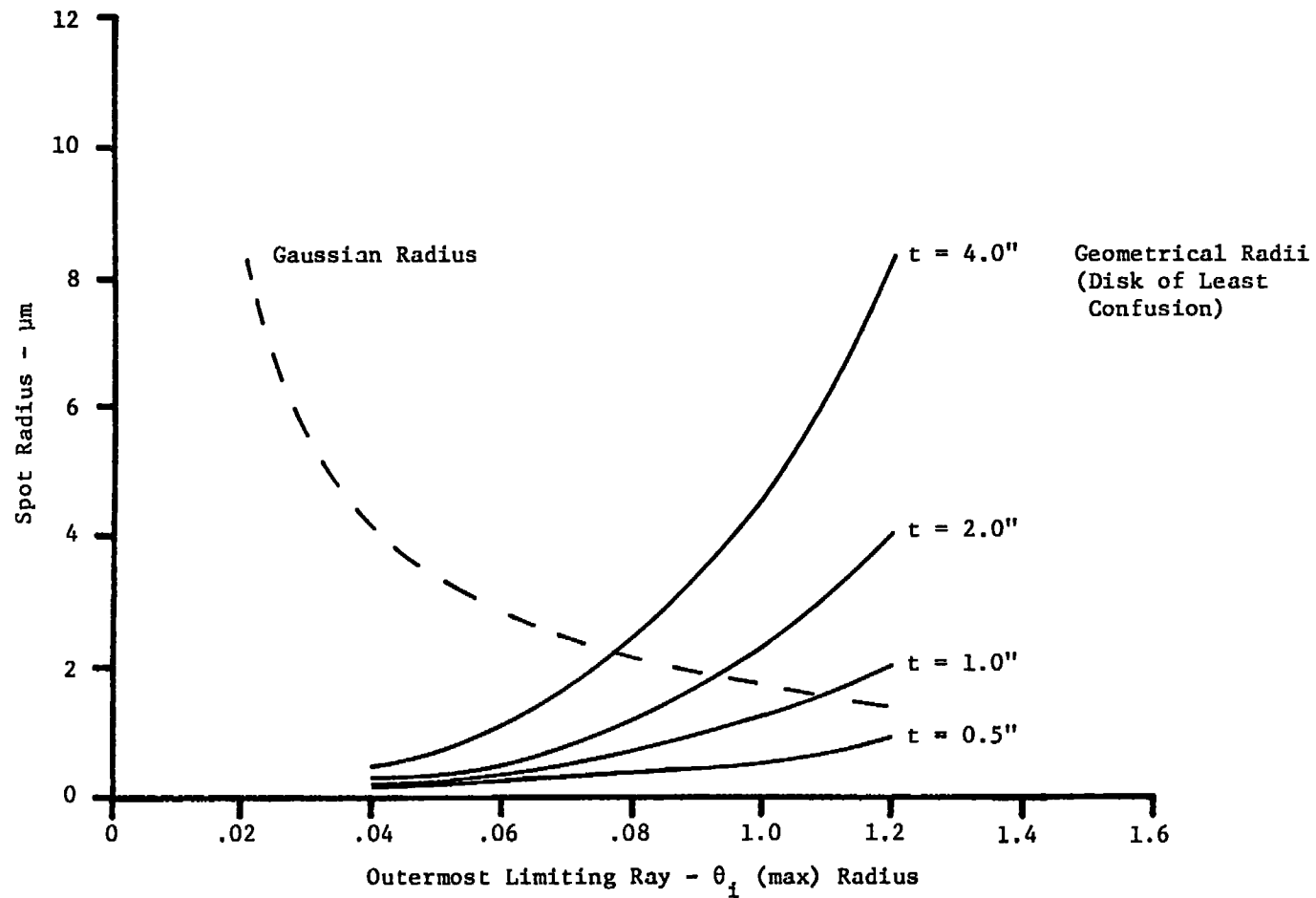


Figure 8. Extreme Disk of Least Confusion Radii.

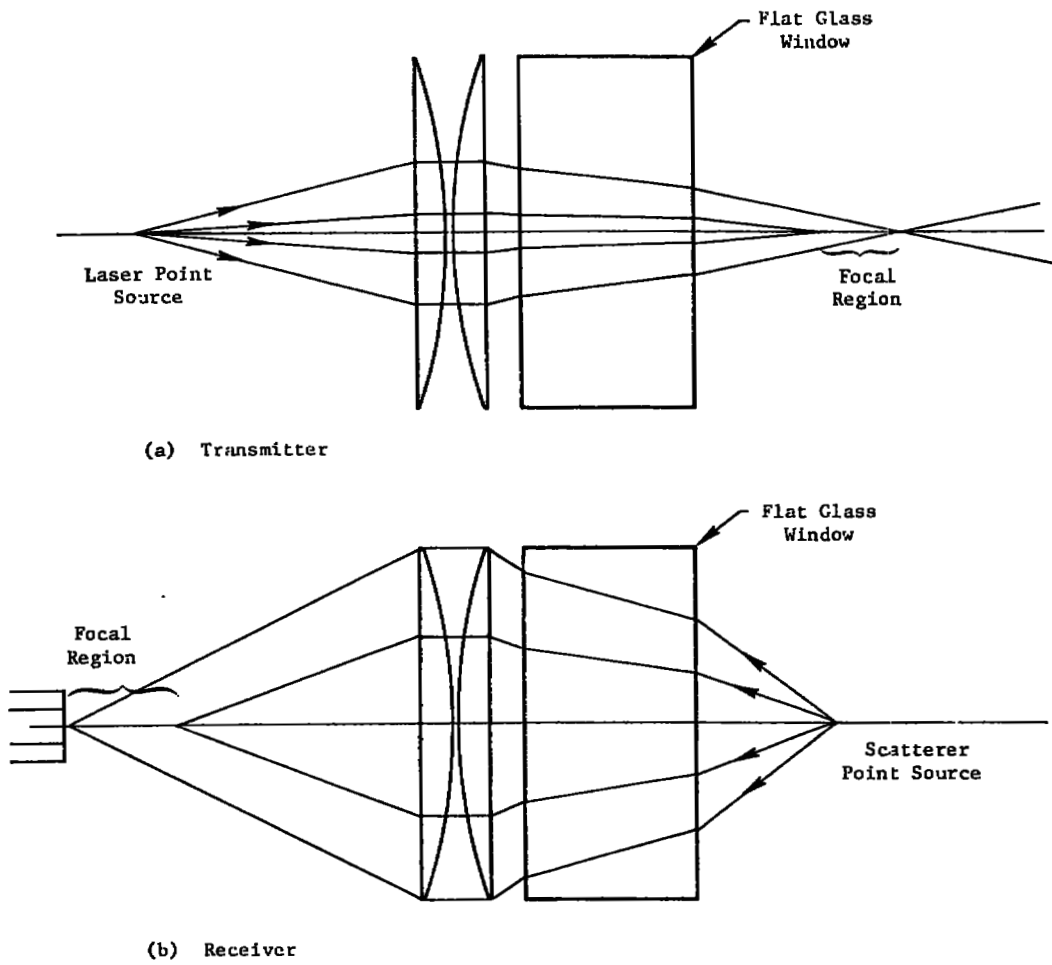


Figure 9. Axial Focus Distortion for Transmitter and Receiver.

focusing further away from the lens than the paraxial focus. Figure 9(b) illustrates that if a scattering point source is located at the paraxial focus of the transmitter beam, then the light intensity distortion in the real image will be of a form similar to that of the transmitter. In fact, for a perfect lens with small flat-window aberrations, we can argue by perturbation theory that the receiver light distribution near the focus has the same mathematical form as was previously derived for the transmitter. (For simplicity we assume that the lens is imaging one-to-one. A change of magnification affects the diffraction-limited spot size and the scaling of the geometrical image in the same way.)

The direction of propagation in a geometrical ray diagram may be reversed without change. We will state, but not prove here, that the effects of interchanging the positions (order) of lens and window will change neither the qualitative nor quantitative descriptors of the aberration pattern. Hence, the aberrations may be predicted by use of the former equations and the diagrams of Figures 3 through 6 may be used once more.

By the preceding slight of hand we are able to examine relative magnitude of the effects of transmitter and receiver spherical aberration on the same figure. Figure 10 is an edited section of Figure 6 with a typical choice of transmitter and receiver edge rays as shown. We see by examining Figure 10 that while the transmitter beam geometrically focuses to a spot much smaller than the diffraction limit (which means the transmitted beam is diffraction limited) the receiver spot image is now significantly larger than what would be either its

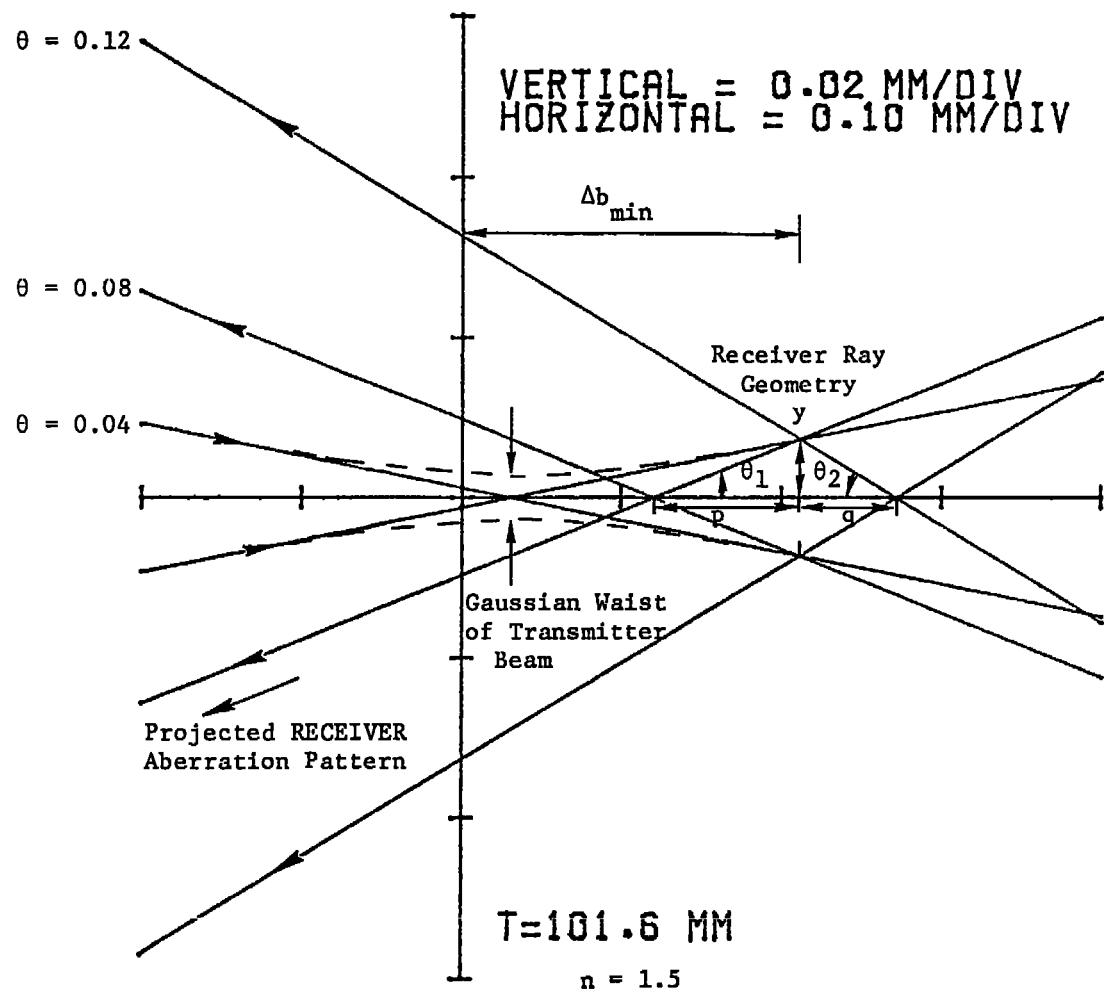


Figure 10. Worst Case Illustration of f/4 Receiver and 4-Inch Thick Window.

own diffraction-limited image or the diffraction-limited image of the inner ray cone which would have been potentially larger.

Note that from Figure 10 with $f/4$ receiver optics and a 4.0" thick window the image covers about twice the radius which it would if the window were absent.

RECEIVER FIELD STOP SIZE AND IMAGE SPOT SIZE REQUIREMENTS

The question of how large to make the receiver field stop pinhole apertures is not such an easy one in some cases. For example, if the actual return image of the point scatterer were as large or larger than the ideal perfect image of the transmitted focused beams, then we would be forced to enlarge the pinholes to avoid losing signal radiation. However, such loss of focus and pinhole enlargement would degrade the system's ability to reject wall flare.

Ideally, we wish for the aberrated receiver spot image to be smaller than the diffraction-limited transmitter beam focus pattern. If the receiver had no aberrations, the diffraction-limited image of the scatterers would be on the order of half the size of the ideal image of the transmitter beam. This is because the receiver lens diameter is approximately twice that of the transmitted beam. In order to maintain near ideal wall flare rejection then, we may say that the receiver point scatterer image diameter must be less than or equal to the receiver Airy disk (the diameter of the central bright portion of the focal spot pattern of a fully illuminated diffraction-limited lens).

The Airy disk radius r_o is given in terms of the edge ray angle by a formula similar to that for the Gaussian beam given earlier

$$r_o = \frac{0.61 \lambda}{\tan \theta_i} \quad . \quad (8)$$

This equation is plotted in Figure 12. We now have arrived at the conclusion that the requirement concerning the acceptable disk of least confusion is about the same for the transmitter and the receiver, i.e., equal to about half of the diffraction-limited transmitter beam diameter; but the aberration effects are much worse for the receiver as seen from Figures 6 and 10 of the previous section.

SOLUTION FOR THE RECEIVER DISK OF LEAST CONFUSION

The diameter of the disk of least confusion is here defined as the diameter of the ray diagrams where the converging edge rays intersect the outermost diverging inner ray. Close inspection of Figure 6 reveals that for a fully-illuminated aperture with edge rays having $\theta = 0.12$, the disk of least confusion is formed by intersection with the $\theta = -0.06$ radius ray. In order to study the way these intersections behave, we may choose an inner and an outer ray and solve for the radius of intersection. Figure 10 illustrates the following notation:

$$y = p \tan \theta_1 = q \tan \theta_2 \quad (9)$$

$$p + q = \Delta b(\theta_2) - b(\theta_1) \quad . \quad (10)$$

From which we solve to obtain

$$y = \frac{\tan \theta_1 \tan \theta_2 [\Delta b(\theta_2) - \Delta b(\theta_1)]}{\tan \theta_1 + \tan \theta_2} \quad (11)$$

The location of the intersection along the optic axis is given by

$$\Delta b_{\min} = \frac{\Delta b(\theta_2) \tan \theta_2 + \Delta b(\theta_1) \tan \theta_1}{\tan \theta_2 + \tan \theta_1} \quad (12)$$

Figure 11 is a plot of Equation (12) with the edge ray θ_2 as a parameter and the inner ray angle θ_1 as a variable. We see that for each case there is a value of inner ray angle above which the diameter of the disk of least confusion decreases (critical angle). The functional behavior of Equation (12) scales linearly with window thickness t , so t is not of concern in determining the value of the critical inner angle. Graphically, we see that for a typical index of refraction of 1.5, this angle is generally about half the angle θ_2 . The implication of this is that, for practical LTA systems, the disk of least confusion may be obtained as the intersection of the outer ray and the minimum angle ray defined by the annular receiver aperture stops. This minimum ray angle is generally greater than half the maximum ray angle.

In order to evaluate the typical diameter of the disk of least confusion for LTA design purposes, we now evaluate Equation (12) parametrically with θ_1 arbitrarily chosen equal to $0.5 \theta_2$. The results are plotted in Figure 12, which while appearing superficially similar to Figure 8 has rather different numerical values and, naturally, different criteria.

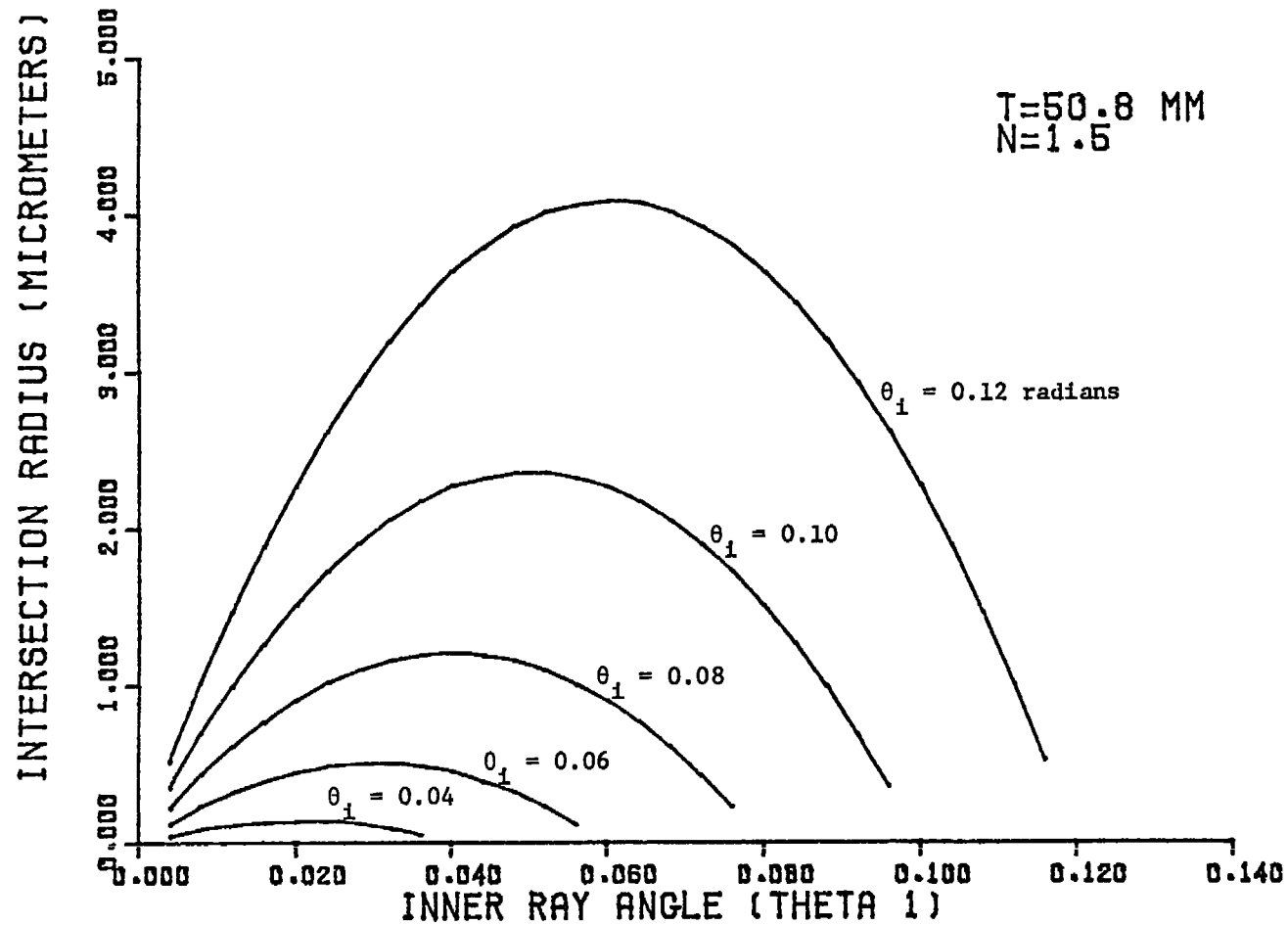


Figure 11. Ray Intersection Radius vs. Receiver Inner and Outer Ray Angles for a 2-Inch Thick Window.

EXPERIMENTAL

For the configuration of the $f/4$ outer lens -- worst case -- some observations were made by projecting the highly magnified focal region on to a distant screen. The first observations were made, using a magnification of about 500x, of the spot from the transmitter. Using glass blocks of up to 4.0" thick, the effects on the spot size were observed to be negligible as was predicted by Figure 8.

When the return spots were imaged at a similar magnification where the source was a fine etched stainless steel surface placed at the best focus of the transmitter, the spot size was measured to increase its diameter by about a factor of two with the introduction of a 4.0" block of optical glass. This, too, accords with the data from Figure 12.

A further observation was made of the way the image changed as the axial position was scanned. In all cases the change in pattern was closely similar to that which is predicted by Figure 10.

CONCLUSIONS

There is much practical information which can be deduced from the preceding graphs. It is immediately apparent from Figure 12 that for windows as thick as 4 inches aberration correction of the receiver would be required for a high-performance $f/4$ system. In more specific terms, a 400 mm $f/4$ Tropel collimator may be used uncorrected with only minor loss of efficiency for windows up to 2 inches thick. In

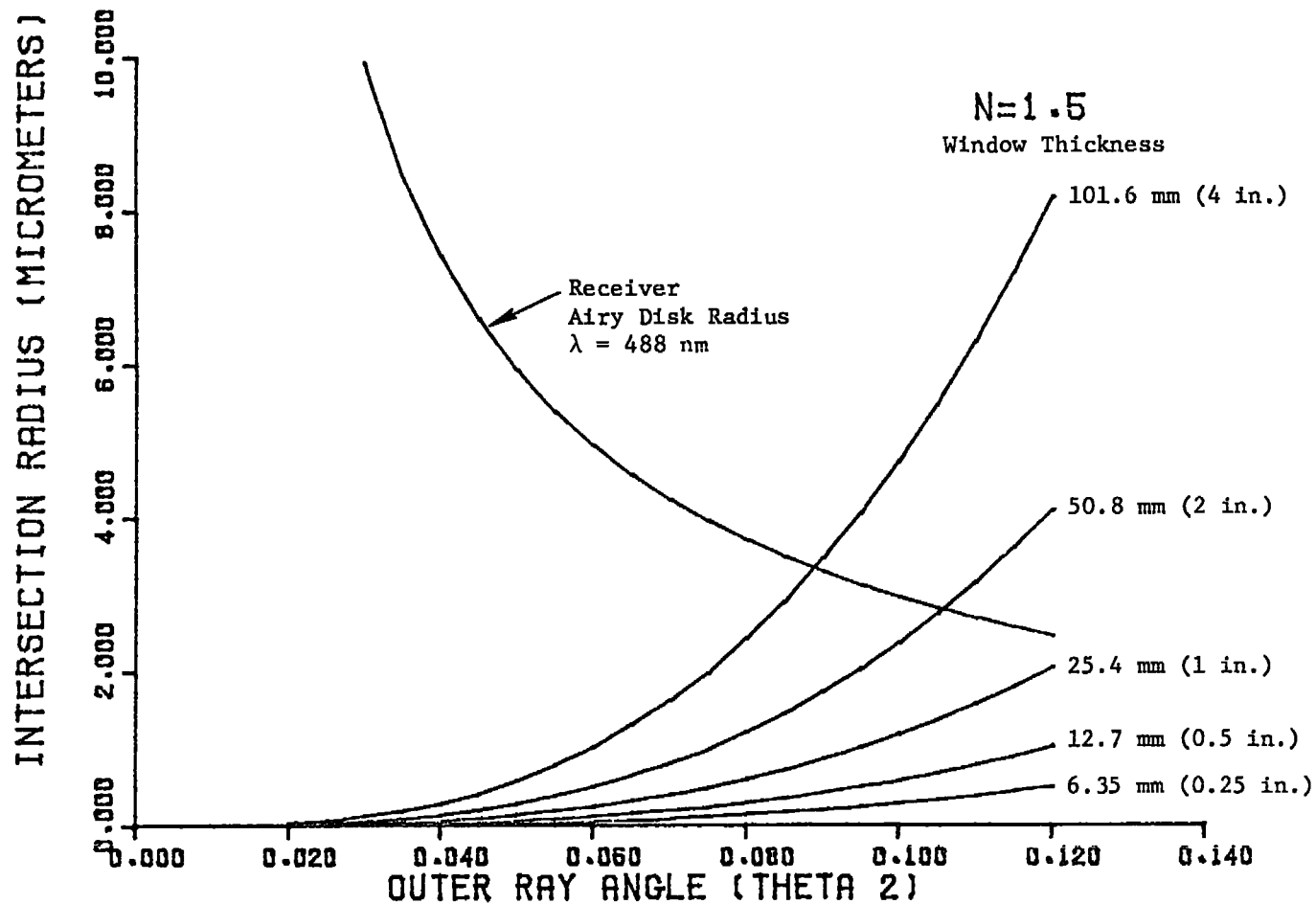


Figure 12. Diffraction-Limited Receiver Radius Compared with Disk of Least Confusion Radius.

addition, we see that even 4 inch thick windows are not a problem for f/6 optics. Experiments with 4 inch windows verified the analytical results.

Incidental experimental observations indicated a marked deterioration of the images if the glass block were inclined to the mean optical axis. This indicates that the thinner windows and smaller collection angle optics may be advisable for application which require observations through windows at other than normal incidence, while scanning for instance, if particular points of interest are only accessible by an angular scan. It will be necessary to attempt some quantification of these effects at a later time but will not be a simple exercise.

There exist methods of correcting the spherical aberrations from which this system can suffer under the extreme window thicknesses cited. The simplest is to use a low-power meniscus lens with positive spherical aberrations. The curvature and power may both be chosen allowing a simple lens to perform adequate correction. It should be located after the transceiver turning mirror because at other positions in the system it would introduce more surfaces into the transmitter beam and run the risk of increasing the internal flare, which so much design has gone to remove.

For most applications, either an f/6 collecting lens or a window 2 inches or less in thickness will be available. Since these criteria also reduce incidence angle effects, we do not anticipate many situations in which spherical aberration compensation would be required.

